

Feasibility of Producing Clad Twin Roll Cast (TRC) AZ31

by

Vignesh Jayakrishnan

A thesis

presented to the University of Waterloo

in fulfillment of the

thesis requirement for the degree of

Master of Applied Science

in

Mechanical Engineering

Waterloo, Ontario, Canada, 2011

©Vignesh Jayakrishnan 2011

Author's Declaration

I hereby declare that I am the sole author of this thesis. This is a true copy of the thesis, including any required final revisions, as accepted by my examiners.

I understand that my thesis may be made electronically available to the public.

Abstract

The need for lighter weight vehicles to improve fuel efficiency is becoming increasingly imperative. Sheet magnesium alloys offer the potential as a light weight material for use in the transportation industry due to their high specific strength and stiffness. In fact, magnesium alloys have the highest strength-to-weight ratio of all the common structural metals. Though the demand for light weight materials is present and sheet magnesium is available, the use of these materials in automotive applications has been rather limited due to high production costs and poor corrosion performance and formability. A promising process to produce wrought magnesium sheet in a more cost effective manner is Twin Roll Casting (TRC). In addition, enhanced corrosion resistance and ductility may be realized in these sheet alloys with the possible introduction of a clad layer during the TRC process thereby producing a laminate sheet where the surface properties are different from the core.

The focus of this research was to investigate the potential of cladding magnesium alloy AZ31 material during the TRC process. As part of this research, a thermal fluid mathematical model of the TRC process was developed, which was then further refined to include the addition of a clad layer during the process. The TRC model was validated through experimental work conducted at the Pohang Institute of Science and Technology (POSTECH University), where TRC experiments of AZ31 were conducted under various casting conditions. The as-cast microstructure of the AZ31 sheets were characterized and measurements of the secondary dendrite arm spacing (SDAS) made at the mid-region were compared to predicted microstructures from the TRC model based on solidification history. The predicted SDAS matched with the measured values, thus, validating the model.

Using the validated TRC model the feasibility of adding a clad layer was assessed and various simulations were conducted to observe the effects of cast speed, cast thickness, and clad material on the thermal history and temperature profile in both the clad and core domains. The material properties

and clad thickness did not seem to impact the temperature profiles significantly, while the cast speed and initial temperature dictated whether or not the cast would be successful. Using these operational parameters a process window was created (based on the CANMET facility) to illustrate the feasibility of casting and cladding during TRC. This window is beneficial for future experimentation and understanding the effects of these casting parameters.

Acknowledgements

I would first and foremost like to thank my supervisor, Dr. Mary Wells, whose support and guidance has helped me greatly throughout my graduate program. I sincerely thank you for the opportunity.

I would also like to thank Dr. Nack Kim, Dr. Jun Ho Bae, Dong Wook, Min Kyu and POSTECH University for lending me their time and resources to accomplish the experimental part of my research.

I thank Dr. Amir Basernia for sharing his expertise with ANSYS-CFX, Amir Hadadzadeh for sharing his modelling experience, Brian Langelier for his assistance with sample preparation, and Ali Nasiri for his general support and aid.

I would like to thank the University of Waterloo, NSERC and MagNET for funding this project and my graduate research.

Finally, I would like to thank Dr. T.K. Venkatachalam for his constant support.

Dedication

For my family,

The ones who accept me for my successes and failures

The ones who hold an unyielding amount of patience

The ones who pushed me to what I thought were my limits only to show me that there were none.

Table of Contents

Author’s Declaration.....	ii
Abstract.....	iii
Acknowledgements.....	v
<i>Dedication</i>	vi
Table of Contents.....	vii
List of Figures	ix
List of Tables	xiii
Nomenclature	xiv
Chapter 1: Introduction	1
1.1 Casting of Mg Alloys.....	2
1.2 Twin Roll Casting Process.....	3
1.3 Cladding Process during Twin Roll Casting	5
Chapter 2: Literature Review	7
2.1 Twin Roll Casting of Aluminum Alloys.....	7
2.2 TRC with Magnesium Alloys.....	8
2.2.1 Microstructure of TRC Sheet.....	10
2.2.2 Cladding during TRC.....	12
2.3 Modelling of TRC Process.....	14
2.4 Summary and Problem Statement.....	18
Chapter 3: Model Development	20
3.1 Governing Equations.....	20
3.2 Geometry	22
3.2.1 Conventional TRC.....	23
3.2.2 Clad-TRC Model.....	24
3.2.3 Mesh	25
3.2.4 Boundary Conditions.....	29
3.2.5 Material Properties	34
3.3 Solver	35
Chapter 4: Experimental Procedure	37

4.1 POSTECH TRC	38
4.2 Procedure.....	39
4.2.1 Surface Temperature Measurements.....	39
4.3 Experiment Matrix	40
4.4 Sample Preparation	42
4.4.1 Grinding and Polishing	44
4.4.2 Etching.....	45
4.5 Microstructure Analysis	46
4.5.1 Optical Microscopy	47
4.5.2 EDS Procedure.....	48
Chapter 5: Results and Discussion	49
5.1 Microstructure Analysis	50
5.1.1 Optical Microscopy	50
5.1.2 SEM and EDS Analysis	56
5.1.3 SDAS Measurements.....	58
5.2 Conventional TRC Model Validation Results.....	60
5.3 Clad TRC	66
5.4.1 Clad Thickness Effects	67
5.4.2 Casting Speed.....	68
5.4.3 Clad Material Influences	73
5.4.4 Process Window.....	74
Chapter 6: Summary, Conclusions, and Future Work.....	78
References	81
Appendix A - CFX Model Setup	85
Appendix B - TRC Procedure	100
Appendix C - Metallography	107

List of Figures

Figure 1 - World Production of Magnesium Metal [3].....	2
Figure 2 - Conventional Horizontal Twin Roll Casting Schematic [6].....	4
Figure 3 - Twin Roll Casting with Cladding Schematic [8]	6
Figure 4 - Process map showing optimal manufacturing conditions for AZ31B alloy (O: successful conditions, Δ: unsuccessful conditions) [14].....	9
Figure 5 - Optical Micrographs of typical solidification microstructures under different casting conditions: a1-a3) casting speeds of 18, 8, 13 m/min and casting temperatures of 993, 973, and 953 K, respectively. [16].....	10
Figure 6 - Material properties comparison of sand cast, die cast, and twin roll cast AZ91 [13]	11
Figure 7 - TEM micrographs of the reaction zone (interface) for: A) as- cast, B) annealed, C) hot rolled samples [19].....	14
Figure 8 - Heat Flux Variation along the Roll Bite [23].....	17
Figure 9 - Velocity Profile at Different Casting Speeds for Asymmetrical Flow [6].....	18
Figure 10 - Isometric View of the TRC mathematical model created based on the POSTECH facility.....	24
Figure 11 – Clad TRC Model	25
Figure 12 - Mesh Sensitivity Analysis of Temperature Readings along the Symmetry Plane.....	28
Figure 13 - Mesh Sensitivity Analysis of Temperature Readings along the Clad-Core Interface.....	28
Figure 14 - Boundary Conditions of Mathematical Model	30
Figure 15 - Fluid Flow Velocity Profile Comparison: Top - Without Source Term, Bottom - With Source Term.....	33
Figure 16 - Annotated picture of the horizontal Twin Roll Caster at POSTECH University.....	38
Figure 17 - Nozzle used for all conducted experiments at POSTECH University. All dimensions in mm....	39
Figure 18 - Schematic of the location of interest for metallography taken at mid-width of cast	43
Figure 19 - Samples from Experiments 1 through 9 from left to right, mounted in an EpoFix cold mount and covered in colloidal graphite.....	44
Figure 20 - Experiment 7 Sample thickness from top surface to bottom surface. Arrow refers to casting direction.....	48
Figure 21 - Surface quality of POSTECH experiments; Left: Decent cast quality (Experiment 4), Right: Poor cast quality (Experiment 8). Scale in inches. Arrow refers to cast direction	49
Figure 22 - Optical Micrograph of Experiment 5 at 50x Magnification. Arrow refers to casting direction	51

Figure 23 - Optical Micrograph of the Top Surface Columnar Dendrite Region below the chill zone at the edge of Experiment 5 at 200x Magnification. Arrow refers to casting direction	52
Figure 24 - Center line (red line) segregation of Experiment 4. Arrow refers to casting direction	53
Figure 25 - Experiment 9 Bottom Surface Chill Zone. Arrow refers to casting direction	53
Figure 26 - Optical Micrograph of Experiment 3 Sample at 50x Magnification. Arrow refers to Rolling Direction.....	54
Figure 27 - Optical Micrograph of the Boundary Region in Experiment 3 at 100x Magnification	55
Figure 28 - Al-Mg Phase Diagram. Red line represents alloy composition [30]	56
Figure 29 - SEM Image of Experiment 1 at the top Surface below chill zone. Arrow refers to casting direction.....	57
Figure 30 - Sample SDAS Measurements of Experiment 1 mid-region at 200x Magnification	59
Figure 31 – SDAS Measurement Distribution for Experiment 1	59
Figure 32 - Center Line Vector of Velocity and Temperature Predicted Values of Experiment 9 (Conditions: 690°C and 1.6 mm).....	62
Figure 33 - Velocity and Temperature Data Collected at the Center Line of the Simulated Casts.....	62
Figure 34 - Comparison of Measured (with 1 standard deviation of error) to Predicted SDAS values of all experiment cases. Dotted lines represent predicted values from simulations. Solid lines represent measured averages.....	64
Figure 35 - Predicted thermal history for Experiment 7 (2.0mm), 8 (1.8mm), and 9 (1.6mm) cast at 690°C	65
Figure 36 – Velocity Curves of Experiment 7 (2.0mm), 8 (1.8mm), and 9 (1.6mm) cast at 690°C	65
Figure 37 - Various Zn Clad Thickness Temperature Profiles: a) 0.5 mm, b) 1.0 mm, c) 1.25 mm. AZ31 core exit thickness: 2.5mm with roll speed of 1.7 m/min.	68
Figure 38 - Temperature Profile of Clad (AZ31) and Core (Al and Zn) at 0.9m/min casting speed	69
Figure 39 - Temperature Profile of Clad (AZ31) and Core (Al and Zn) at 1.7m/min casting speed	70
Figure 40 - Temperature Profile of Clad (AZ31) and Core (Al and Zn) at 3.0m/min casting speed	71
Figure 41 - Percent melting that occurs across the thickness of the zinc clad layer along the roll bite position	72
Figure 42 – Temperature of Al Clad – AZ31 Core Interface along the Roll Bite Position for various casting speeds	73
Figure 43 - Results from Simulations Conducted at Various Casting Parameters: A) A failed cast due to cooling before entry, B) A successful cast, C) A failed cast due to insufficient cooling.....	74

Figure 44 - TRC Process Window for the CANMET facility for a clad thickness of 0.5 mm	76
Figure 45 - TRC Process Window influences from clad thickness. Red arrows represent the direction clad boundaries move if clad thickness decreases. Green arrows represent the direction clad boundaries move if clad thickness increases.....	77
Figure 46 - CFX-Pre Model Setup Screen	86
Figure 47 - AZ31 Material Properties Setup.....	87
Figure 48 - AZ31 Material Properties Setup cont'd	88
Figure 49 - Clad Domain Setup.....	89
Figure 50 - Core Domain Setup	90
Figure 51 - Core Domain Setup cont'd.....	91
Figure 52 - Inlet Setup.....	92
Figure 53 - Outlet Setup.....	93
Figure 54 - Roll Surface Boundary Condition Setup. Rotating wall is setup at domain interface for the clad model	94
Figure 55 - Source Term setup for Fluid Flow Correction	95
Figure 56 - Symmetry Plane Boundary Condition.....	96
Figure 57 - Adiabatic Wall Setup.....	96
Figure 58 - Zinc Material Properties Setup	97
Figure 59 - Conductivity Equation Setup	98
Figure 60 - Solid Fraction Equation Setup.....	98
Figure 61 - Specific Heat Capacity Equation Setup	99
Figure 62 - Expression Setup.....	99
Figure 63 - TRC controls	102
Figure 64 - Difference of Melt Pool with (Right) and without (Left) protective gas shielding.....	103
Figure 65 - Guiding the cast out of the rolls while removing any debris attached to the rolls	104
Figure 66 - Removing the tundish from the furnace and submerging it in sand.....	105
Figure 67 - Tundish dimensions	106
Figure 68 - Palette of all experiment sample thicknesses	109
Figure 69 - Experiment 1 SDAS Measurements	110
Figure 70 - Experiment 2 SDAS Measurements	111
Figure 71 - Experiment 3 SDAS Measurements	111
Figure 72- Experiment 4 SDAS Measurements.....	112

Figure 73 - Experiment 5 SDAS Measurements	112
Figure 74 - Experiment 6 SDAS Measurements	113
Figure 75 - Experiment 7 SDAS Measurements	113
Figure 76 - Experiment 8 SDAS Measurements	114
Figure 77 - Experiment 9 SDAS Measurements	114

List of Tables

Table 1 - Examples of Current Magnesium Usage in today's Vehicles [2]	2
Table 2 - Production Cost Comparison of AZ31 Sheet [5].....	3
Table 3 - Material properties comparison of AZ31, AZ91 and commercial AZ31B alloys along the rolling and transverse directions	12
Table 4 - Material Properties of AZ31 [23]	34
Table 5 - Experiments conducted using the TRC at POSTECH University for AZ31	42
Table 6 - Atomic % of Each Element by Region	58
Table 7 - Average Measured SDAS Values	60
Table 8 - Secondary Dendrite Arm Spacing Values: Predicted vs. Measured.....	63

Nomenclature

Acronyms and Abbreviations:

TRC – Twin Roll Casting

VTRC – Vertical Twin Roll Casting

HTRC – Horizontal Twin Roll Casting

DC – Direct Chill [Casting]

ASTM – American Society for Testing and Materials

CFD – Computation Fluid Dynamics

HCP – Hexagonal Closed Pack [Structure]

HTC – Heat Transfer Coefficient

UTS – Ultimate Tensile Strength

YS – Yield Strength

Symbols:

u - Velocity (m/s)

ρ - Density (kg/m^3)

g - Gravitational constant (m/s^2)

μ - Dynamic viscosity (Pa s)

P - Pressure (Pa)

C_p - Specific heat capacity at constant pressure ($\text{J/kg}^\circ\text{C}$)

K - Thermal conductivity ($\text{W/m}^\circ\text{C}$)

T - Temperature ($^\circ\text{C}$)

H - Enthalpy (kJ/kg)

C - Constant of the liquid phase (between 10^4 - 10^7 for the AZ31 alloy)

f_l - Fraction of liquid

ε - Small number to avoid dividing by zero

Q'' - Heat Flux (J/m^2s)

\dot{m} - Mass flow rate (kg/s)

θ - Pressure Profile Blend

P_{profile} - Pressure of user specified profile (Pa)

P_{floating} - Pressure upstream of the outlet (Pa)

P_{nor} - Normalized Pressure (Pa)

Chapter 1: Introduction

Fuel efficiency is becoming increasingly important in the automotive industry. In part, this is due to the constant depletion of today's oil reserves and the continuous increase of greenhouse gas emissions to the environment. Hence, newer vehicles are designed to be lighter and more fuel efficient. The Canadian government has set a target of reducing the amount of greenhouse gas emissions by 45-65% by the year 2050 [1]. Since the transportation sector contributes about 25% of the GHG emissions, the North American automotive industry has set a goal to increase the amount of magnesium usage within vehicles from 5kg to 160kg per vehicle by the year 2020 [1]. Replacing pre-existing components within vehicles with much lighter magnesium components will, in turn, make vehicles more fuel efficient and help Canada achieve its target.

Magnesium is increasingly becoming a more attractive material of choice for vehicle components due to its high strength-to-weight ratio. The density of magnesium (1.7 kg/m^3) is much lower than steel (7.8 kg/m^3) or aluminum (2.7 kg/m^3) [2]. Other attractive properties of magnesium and magnesium alloys for the automotive industry include its ability to absorb vibrations, its good weldability, and machinability. Figure 1 displays the overall increase in production of magnesium metal, which has been increasing since the 1950s. This can be attributed to the growing knowledge and interest in this material. Table 1 shows some examples of magnesium usage within current vehicles.

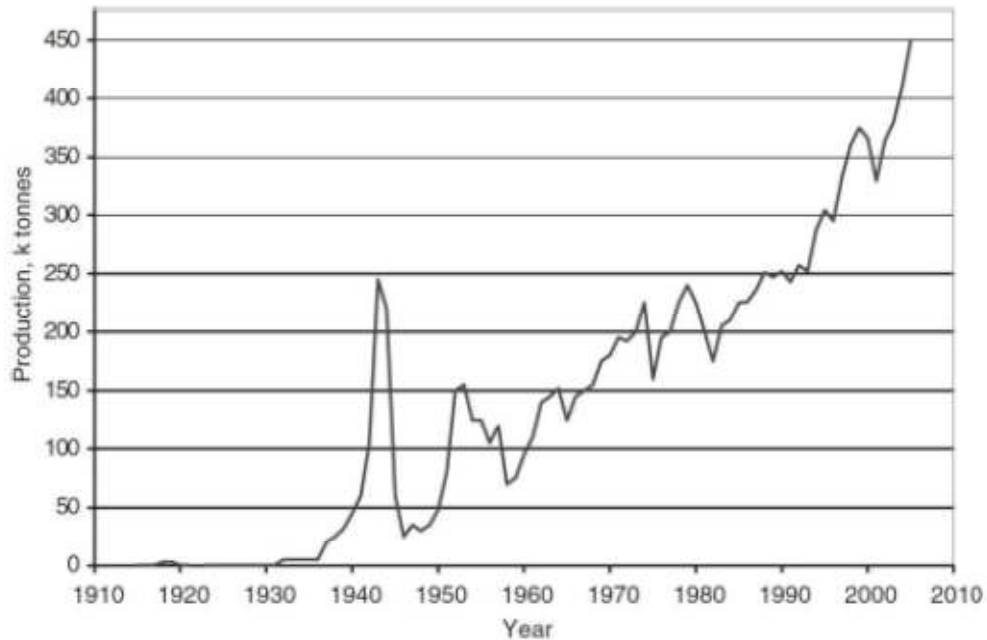


Figure 1 - World Production of Magnesium Metal [3]

Table 1 - Examples of Current Magnesium Usage in today's Vehicles [2]

Company	Part	Model
Ford	Clutch housing, steering column	Ranger
GM	Valve cover, air cleaner, clutch housing	Corvette
Porsche	Miscellaneous components (45kg)	911
Mercedes-Benz	Fuel tank cover	SLK
Volkswagen	Gearbox housing	VW Passat
Toyota	Steering wheels	Lexus, Celica, Carina, Corolla
Opel	Roof	G90
BMW	Engine block, Air intake system	3 Series

1.1 Casting of Mg Alloys

Manufacturing parts prove to be somewhat difficult with magnesium and magnesium based alloys due to its hexagonal close packed (HCP) crystalline structure. This structure limits the formability of the material and restricts the amount of deformation it can undergo in one step. This means that magnesium alloys require more incremental steps of deformation for part production. Because of this, magnesium sheet production is an expensive process compared to that of aluminum or steel [4]. An alternative production method to overcome these obstacles is the twin roll casting process.

Instead of multiple deformation steps in small increments with annealing stages in between, the twin roll casting process allows for a single process; from molten metal to cast sheet. In addition to reducing production steps, the cost of this process is reduced significantly. Processing costs are a third to a half as high, operating and investment costs are only a quarter to a third as high, and there are lower space and labour requirements. Furthermore, less energy is required as it is no longer necessary to pre-heat the ingot before rolling [4]. Table 2 displays the difference in cost with the production process of twin roll casting in comparison to conventional methods.

Table 2 - Production Cost Comparison of AZ31 Sheet [5]

Manufacturing Process	Costs
Conventional	9.92
Twin Roll Casting	4.34

* 10,000 tpy of 1.5mm thick×1m wide AZ31 sheet

1.2 Twin Roll Casting Process

The twin roll casting process is a casting process first patented in the mid-19th century by an English engineer, Sir Henry Bessemer [4]. This process involves feeding molten metal through two counter rotating rolls, which act as the cooling and deformation elements to solidify the molten metal into sheet. Figure 2 shows a schematic of the traditional twin roll casting process. There are two types of twin roll casters; vertical twin roll casters (VTRC), and horizontal twin roll casters (HTRC). The type of caster is labelled with respect to the direction of casting.

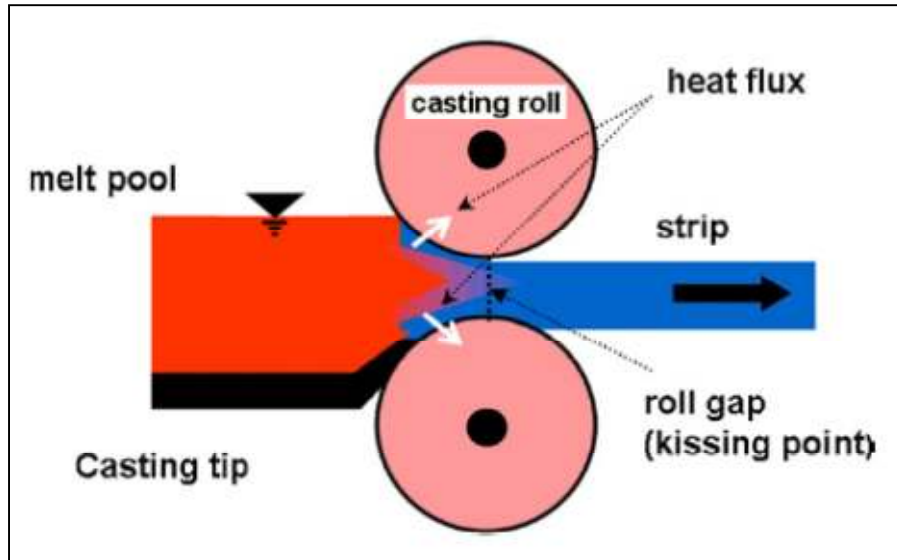


Figure 2 - Conventional Horizontal Twin Roll Casting Schematic [6]

The main equipment used within this process are the crucible, the tundish, the molten metal feeding system (referred to as the nozzle), and the internally-water cooled rolls. The crucible is where the metal is melted and held until casting is ready. Once casting commences, the metal is released into a tundish placed in a furnace at the desired casting temperature. From this point, the metal is fed through the nozzle and towards the rolls, which act as a solidification “mold”. The molten metal solidifies and is squeezed through the gap in the rolls to exit as sheet metal. In some cases, when a highly reactive metal is being cast, such as magnesium and magnesium alloys, a shielding gas would also be required for this process in order to prevent oxide formation within the melt pool. Sometimes a vacuum furnace is also used to limit oxide formation. The quick oxide formation for magnesium alloys makes the humidity levels of the facility a great concern.

The twin roll casting process can achieve cooling rates in the range of 100°C/s - 1000°C/s [7]. The cooling rate is greatly dependent on the roll speed, and the roll material; typically, the rolls are made of steel or copper. The material of the rolls has a significant impact on the roll speeds that can be achieved due to the fact that the material of the roll helps dictate the heat transfer coefficient at the interface between the molten metal and roll surface. The higher the heat transfer coefficient, the more heat can

be extracted in a shorter period of time, which, in turn, results in the ability to cast at higher speeds. Thus, the roll material directly impacts the production rate of cast sheet within the twin roll casting process. Typically, a lubricant or parting agent will be sprayed on the rolls to prevent the core material from sticking to the rolls during casting. However, this further inhibits the production rate of the sheet since the lubricant acts as a thermal barrier, which lowers the heat transfer coefficient of the system.

1.3 Cladding Process during Twin Roll Casting

A possible innovation to the twin roll casting process of magnesium involves casting such that a clad layer is joined to the sheet surface during the process. The main difference in a clad process as compared with the traditional twin roll casting process is that the cast exits with a clad layer bonded to its surface. One way in which this is accomplished is by inserting a thin sheet or foil at the point of contact between the roll and the core material while the core is still in its molten state. Due to the significant pressure of the rolls and the solidification of the molten metal core, the resulting exit core is bonded or joined to the clad material. Ideally, the heat of the core metal would induce partial melting of the clad layer at the point of contact in order to create a strong metallic bond at the interface [8]. One advantage of the addition of a clad layer to the surface of magnesium sheet would be to improve the weldability of the sheet for magnesium alloys, such as AZ31 (3% Al, 1% Zn) to other materials. Currently, the constant presence of an oxide layer makes joining and bonding processes very challenging. Introducing a thin surface of another material with good joining properties will aid in the ability to join magnesium alloys to other metals while still maintaining the high specific strength of magnesium metal for the sheet. Joining of the clad layer to begin with is made possible because of the limited oxide present due to the fact that the magnesium core is still in its liquid state in a controlled environment. Any oxide that does form is forced towards to surfaces of the material through the immense pressure of the rolls. Figure 3 is a schematic of one method that a clad sheet could be created during TRC.

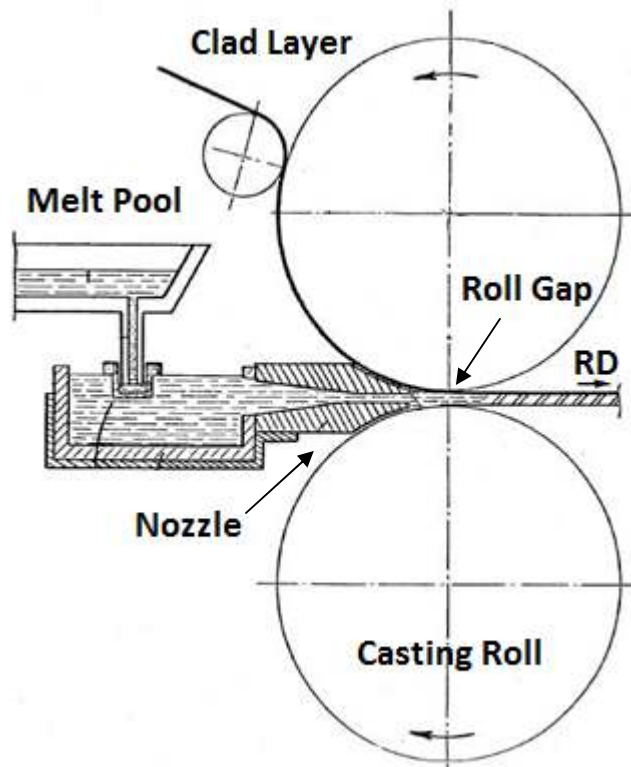


Figure 3 - Twin Roll Casting with Cladding Schematic [8]

In addition to the joining aspect, there are many other advantages of having a clad layer on magnesium sheet. Another advantage could be to improve the ductility of magnesium and magnesium alloy sheet. As a protective coating, the clad layer also offers increased corrosion resistance to the magnesium sheet. This research will explore the feasibility of the cladding process during TRC of magnesium sheet.

Chapter 2: Literature Review

This chapter reviews the literature associated with the twin roll casting process, roll heat transfer coefficient, resulting TRC magnesium alloy microstructure and model development of the TRC process. With twin roll casting of magnesium alloys being a relatively new initiative, the literature within this area is somewhat limited. Though the primary focus of this research involves the AZ31 alloy, the background has not been limited to this material and broadens the review to other magnesium alloys and aluminum alloys. This literature review also focuses on attempts to clad material during the TRC process.

2.1 Twin Roll Casting of Aluminum Alloys

The Twin Roll Casting (TRC) process is based on a concept patented by Sir Henry Bessemer in 1865 that integrated vertical casting and rolling technologies to produce steel strip directly from liquid steel [4]. Limitations on refractory materials development, sensing and process control technologies prevented commercial penetration of the steel TRC process in the 19th century and, in fact, it wasn't until the 1950s that the TRC process was successfully applied to commercial strip production for aluminum sheet. Aluminum TRC was developed by two major manufacturers, Hunter (later to become Fata Hunter) in the USA and Pechiney (later to become Novelis PAE) in France, both adopting horizontal placement of the roll casters, not the vertical configuration originally envisioned by Bessemer. Over the years, the casters have become larger in size to produce wider, thinner gauge, highly alloyed strip, While in its early stages TRC of aluminum was fairly slow (1 m/min), changes to the process equipment , allowed speed increases up to 60 m/min today [9]. Furthermore, the TRC process is also used for certain carbon and stainless steels and can reach speeds of up to 150 m/min [10]. Magnesium alloy sheet production via TRC, on the other hand, is still in the early stages of commercialization.

2.2 TRC with Magnesium Alloys

Since magnesium's properties (particularly its high specific strength and stiffness) make it an appealing material for the automotive industry, its implementation continues to be a motivating yet challenging task. As mentioned in Chapter 1, the twin roll casting process offers a more cost effective method of producing sheet magnesium. Experimental TRC of magnesium was carried out for the first time in the 1980's by Dow Chemical, who used a proprietary molten magnesium handling system, coupled with a Hunter caster originally designed for aluminum alloys (horizontal configuration) to produce 200 Kg coiled magnesium strip, with a thickness of 6 – 7 mm and width of 610 mm, at a casting speed 1.5 m/min [11] [12]. While the magnesium sheet market hadn't matured enough to warrant commercialization of the TRC process at that time [11] [12], interest in TRC of magnesium has advanced rapidly since 2000, with major research programs initiated in Australia, Germany, Korea, Japan, Turkey and Canada [12] [13]. The feasibility of this process has been assessed by many researchers. Primarily, Watari et al. [4] has published many journal papers reviewing the effect of casting parameters on the TRC process. Their work consisted of examining different magnesium alloys (AZ31, AZ61, AM60, and AZ91) and observing the formability of the higher aluminum content alloys. The thickness of the cast was also investigated with respect to the casting parameters. Usually the cast thickness is a controlled parameter set by the roll gap. Depending on the casting conditions, the roll force required to maintain a desired thickness varies. In this study, however, the roll force was maintained at zero and the thickness of the sheet was observed. It was found that increasing casting temperature or roll speed resulted in thinner sheets. In addition, preliminary process maps for the TRC of magnesium sheet were developed based on experimental trials conducted.

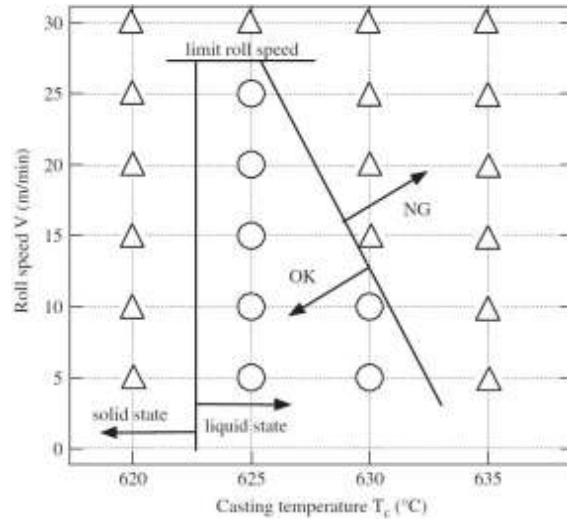


Figure 4 - Process map showing optimal manufacturing conditions for AZ31B alloy (O: successful conditions, Δ: unsuccessful conditions) [14]

Conveniently, operating temperatures required during TRC of magnesium fall in the same range as aluminum TRC, suggesting the same TRC equipment can feasibly be used for both metals. However, there are some unique challenges to applying the TRC technology to magnesium alloys as compared to aluminum, including [11] [12]:

- Molten magnesium readily oxidizes and ignites; it is critical to provide a safe, protected environment for handling molten magnesium as it is being fed into the casting system.
- Liquid magnesium is very reactive to silicon (Si); direct contact between liquid magnesium and ceramic containing Si should be avoided.
- The volumetric heat capacity and latent heat of magnesium are lower than that of aluminum [12], indicating that liquid magnesium freezes faster than liquid aluminum. This fast freezing will make it difficult to achieve uniform solidification across the strip [15].
- Magnesium wrought alloys have larger freezing ranges than typical aluminum wrought alloys produced by TRC which increases the likelihood of both cracking and segregation [15].

2.2.1 Microstructure of TRC Sheet

Majority of the work done with the twin roll casting process involves the microstructure formation. Due to fact that the solidification rates in strip casting (up to 1000°C) are significantly higher than direct chill (DC) casting (1-50°C), the resulting microstructure is a lot finer. Ju and Hu [16] looked into the effects of casting parameters on the microstructure. The authors cast AZ31 alloy under three different roll speeds and temperatures. The roll speeds were 8, 13, and 18 m/min, while the temperatures chosen were 973, 953, and 993 K, respectively. Three different microstructures were observed, which are shown in Figure 5. The first microstructure consists of α -Mg and a mixture of coarse, irregular fibrous and granular Al-rich solid solution and the fully divorced granular eutectic $Mg_{17}Al_{12}$, which are concentrated in the center of Al-rich solid solution. The second microstructure consists of rosette-like α -Mg and cellular eutectic $Mg_{17}Al_{12}$ with fine branches of Al-rich solid solution. The third microstructure consists of a typical columnar dendritic structure with fine featherlike secondary dendrite, where the Al-rich solid solution is located in the interdendritic regions and some granular eutectic $Mg_{17}Al_{12}$ are also concentrated in the center of Al-rich solid solution.

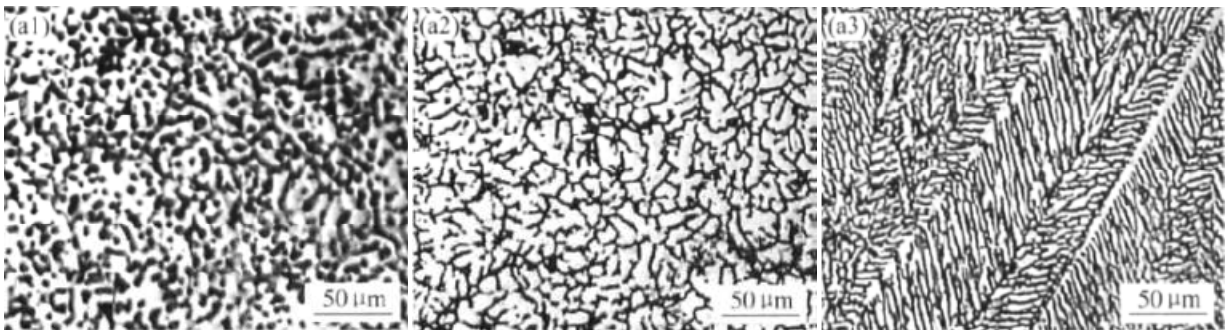


Figure 5 - Optical Micrographs of typical solidification microstructures under different casting conditions: a1-a3) casting speeds of 18, 8, 13 m/min and casting temperatures of 993, 973, and 953 K, respectively. [16]

Figure 5-(a2) was found to be the type of structure observed within the center of the samples, which is the last to cool, implying that this type of microstructure is formed at lower cooling rates. Figure 5-(a3) was found near the surface of most of the samples and the length of the columnar

dendrites increase with increasing cast speed. A comparison was also made between raw material and twin roll cast strip. It was found that the grain size could be reduced from 200-40 μm to 50 μm [16].

Allen et al. [13] conducted experiments to observe the effects of hot rolling AM60 as-cast strips. After obtaining a similar microstructure as Ju and Hu for the as-cast samples, when hot rolled the dendrites morphed into deformed grains. $\text{Mg}_{17}\text{Al}_{12}$ and Al-Mn intermetallics between the grains were seen as well as very fine $\text{Mg}_{17}\text{Al}_{12}$ particles within the grains. Typical dendrite arm spacing of 7-9 μm were transformed into grains of 9-10 μm in diameter. The small grain size is expected to benefit superplasticity [13]. A comparison of AZ91 material properties was made between hot-rolled twin roll cast samples and sand cast and die cast samples. Figure 6 shows the results of the ultimate tensile strength (UTS) and yield strength (YS). A 60% increase in YS and a 17-40% increase in UTS were discovered. However, the grain size was not found to be the cause of the increase since all three materials had similar grain size (approx. 20 μm). Instead, this increase is thought to be attributed to $\text{Mg}_{17}\text{Al}_{12}$ precipitate spacing. Typically, the spacing is greater than 300nm but in their case the spacing was found to be 30-100nm.

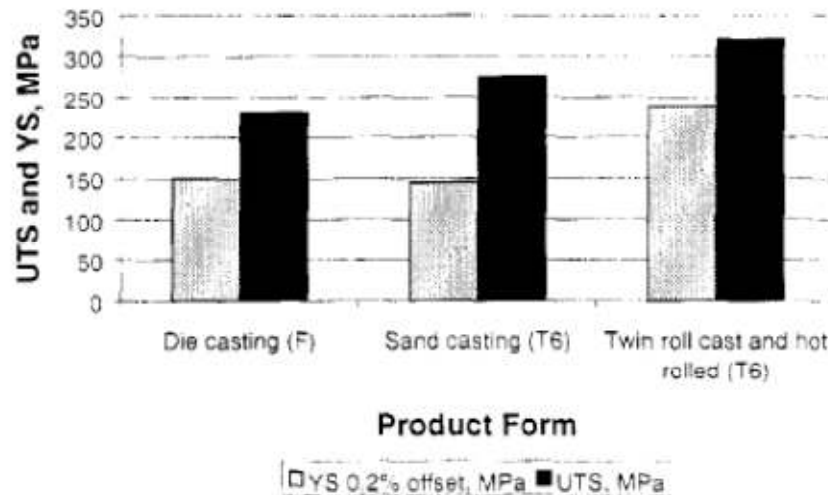


Figure 6 - Material properties comparison of sand cast, die cast, and twin roll cast AZ91 [13]

The mechanical properties of magnesium alloys were also observed by Numano et al. [17]. Two alloys were cast, AZ31 and AZ91, and heat treated and hot rolled and compared with commercial AZ31B. The microstructure of the homogenized AZ31 and AZ91 alloys had grain sizes of 22 μm and 21 μm ,

respectively. The AZ91 alloy, however, showed fine precipitates near the grain boundaries and within the grains themselves. When compared to the commercial AZ31B alloy, large intermetallic compounds (10 μ m) could be seen within the commercial alloy but were absent within the rolled alloys. After the two rolled alloys went through optimized finish rolling paths, the mean grain size decreased substantially. The mean grain sizes at this stage for the AZ31 alloy, AZ91 alloy and AZ31B alloy were 4 μ m, 5.6 μ m, and 8.5 μ m, respectively. Table 3 shows the UTS, YS, and elongation of each of the materials. After conducting drawing tests, the AZ31 rolled sheet showed higher draw ability compared to the commercial AZ31B alloy.

Table 3 - Material properties comparison of AZ31, AZ91 and commercial AZ31B alloys along the rolling and transverse directions

Material	Direction	Ultimate Tensile Strength (MPa)	Yield Strength (MPa)	Elongation (%)
AZ31	RD	280	210	23
	TD	290	230	21
AZ91	RD	340	220	17
	TD	330	230	14
AZ31B	RD	260	170	20
	TD	270	200	16

2.2.2 Cladding during TRC

The introduction of a clad layer during twin roll casting is a novel method to produce a multilayer sheet such that the surface properties are different from the core of the sheet. Papich et al. developed various patents for the clad TRC system for magnesium alloy cores with various aluminum alloy clad layers [18]. The method of inserting the clad layer follows the same method described within section 1.3. Some other modifications were introduced such as thermal spray deposition stations, where an interlayer (such as zinc) was sprayed onto the clad layers. This was done to prevent inter-diffusion between the magnesium core and aluminum clad. These methods are still in their theoretical stage and have not yet underwent actual experimentation. There has been only one case of attempting to clad

magnesium alloys during the TRC process. This was performed at POSTECH University by Prasada Rao et al. [19] who managed to successfully clad a magnesium alloy (Mg – 6 Zn -3 Al) with aluminum using a horizontal lab scaled twin roll caster. The aluminum foil used as the clad material was 50 μm in thickness. The resulting cast was heat treated at 300°C for one hour and hot rolled as well. The microstructures of the as-cast, annealed, and hot rolled samples were observed. The as-cast appeared to form an $\text{Mg}_{17}\text{Al}_{12}$ intermetallic at the interface, while the annealed sample showed the introduction of Mg_2Al_3 intermetallic as well. The hot rolled sample showed a reduction in the overall thickness of the interface and primarily in the thickness of the $\text{Mg}_{17}\text{Al}_{12}$ intermetallic (Figure 7).

The three samples that were observed (as-cast, annealed, and hot rolled) underwent bending tests in order to assess the formability of the clad sheets. It was found that the annealed sheets showed cracks in the reaction zone (interface), which propagated to the aluminum clad layer. The hot rolled samples, however, failed in the core and did not show any signs of cracks within the clad layer or interface. Though the results of the bending test for the as-cast sample were not commented on, it is assumed that the performance of this sample would have been similar or worse than the annealed sample due to the large amount of $\text{Mg}_{17}\text{Al}_{12}$ at the interface. This work conducted by Prasada Rao et al. is a significant contribution towards opening up the applications and possibilities of magnesium usage in today's world.

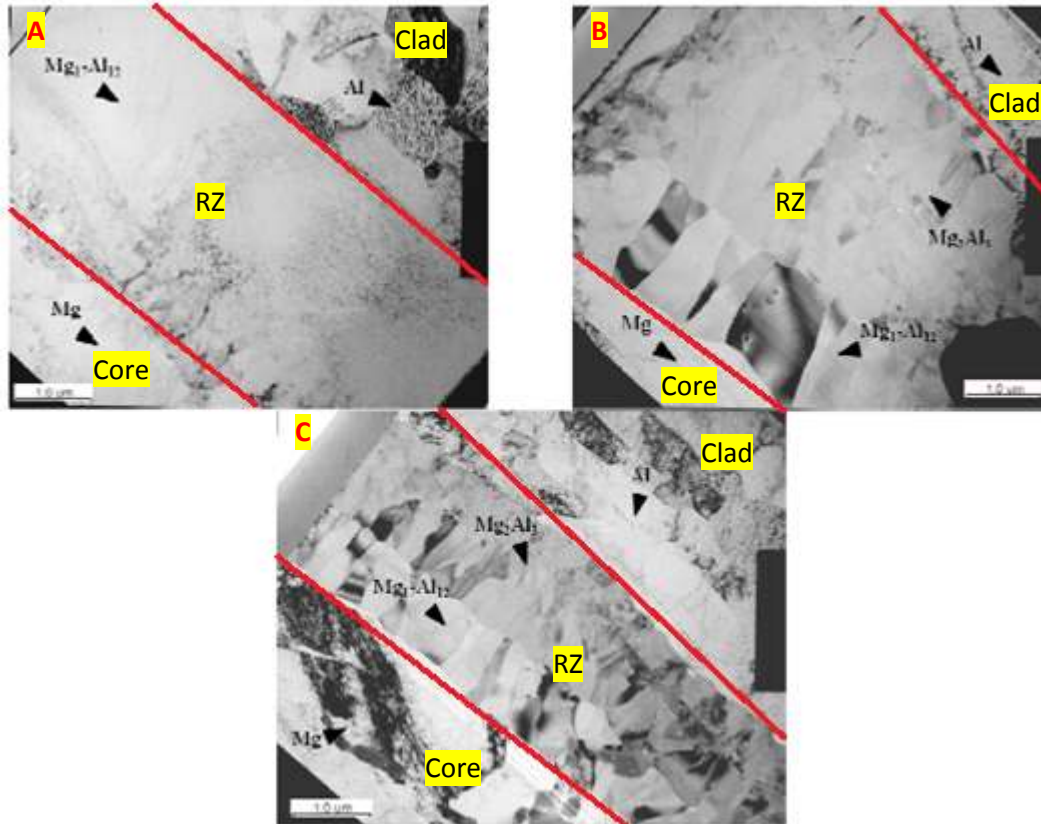


Figure 7 - TEM micrographs of the reaction zone (interface) for: A) as-cast, B) annealed, C) hot rolled samples [19]

2.3 Modelling of TRC Process

Since there is much more to understand about the TRC process with respect to magnesium and its alloys, generating a mathematical model greatly aids in the development and progress of the casting process. Though the importance of developing a model is evident, very few models have actually been created for TRC of magnesium alloys. There are, however, many models developed for other alloying systems, which can be used as a stepping stone in the development of a magnesium TRC model.

Different numerical models have been presented by various authors. The majority of the models developed are thermal-fluid models that consider the transport phenomena coupled with solidification effects. Very few cases also incorporate deformation and stress analysis within the model. The difference between each model lies mainly within the boundary conditions set. Of these boundary

conditions, the most important one is the heat transfer coefficient. Many different methodologies have been used to represent the heat transfer coefficient between the roll and metal. Hwang et al. (1996) [20] suggested a constant heat transfer coefficient could be used in his CFD model to describe the thermal conduction at the interface between metal and roll. Using experimental data for a Sn-15Pb as validation, an HTC of 25kW/m²C in the roll bite provided a good match of the measurements to the predictions. Realizing that the HTC changes along the roll bite, Bae et al. developed a 2D VTRC model for the AZ91 alloy with a different type of boundary condition for the HTC. The roll and melt pool were taken into account and an HTC of 20 kW/m²K was used until the final solidification point, at which the HTC was changed to 8 kW/m²K. This is presumed to be due to the air gap formation during the process. Bradbury *et al.* [21] and Yun *et al.* [22] coupled fluid flow, heat transfer and plastic deformation for Al-8%Cu TRC. In order to represent the HTC for these models three methods were used to apply the HTC over the arc of contact:

- I. Method I; Constant HTC: 30kW/m²C (evaluated by comparing to strip exit temperature through experiment).
- II. Method II; Step function: in this method, the HTC distribution was adopted as a step function in which the step position and shape was determined based on the solid fraction at the centre line. The solid fraction had been predicted by the constant HTC (Method I) and then used for this part. By comparing to the experimental results, low and high values of this step function were evaluated as 22.5 and 60kW/m²C, respectively.
- III. Method III; HTC as a function of contact pressure: the pressure along the contact region was calculated (in Method I) and normalized to be between 0 and 1. Then, HTC was defined as Equation 2.1:

$$HTC = h_{min} + P_{nor}(h_{max} - h_{min}) \quad (2-1)$$

$$HTC = h_{max} \text{ if } HTC > h_{max} \quad (2-2)$$

$$HTC = h_{min} \text{ if } HTC < h_{min} \quad (2-3)$$

where P_{nor} is the normalized contact pressure. h_{min} and h_{max} were determined to be 22 and 60kW/m²C, respectively through comparison the modeling and experimental results. [23]

Another methodology was undertaken by Tavares et al. and Guthrie et al. [24] (1998), who concentrated their CFD-simulation on different molten metal delivery systems for twin roll casting. Their focus was for low carbon steel. They have been the only investigators to apply a varying heat transfer coefficient as a function of the roll force on the cast. Figure 8 shows a schematic of how the heat flux varies along the roll bite. Solidification occurs when the molten metal first comes into contact with the rolls and cools via conduction. At this point a thin film of air forms in between the solid shell and roll. This air gap creates another method of heat transfer, convection (and some radiation as well) for the melt pool to solidify. This results in a lower heat flux. Roll expansion can then occur due to temperature elevation and pressure on the solidified shell rises because the melt pool level increases. These phenomena eliminate the air gap, which allows for more direct contact between the rolls and strip and results in an increase in heat flux. Following this, the solidified shell starts to shrink and the contact area with the roll decreases, thus, decreasing the heat flux once again.

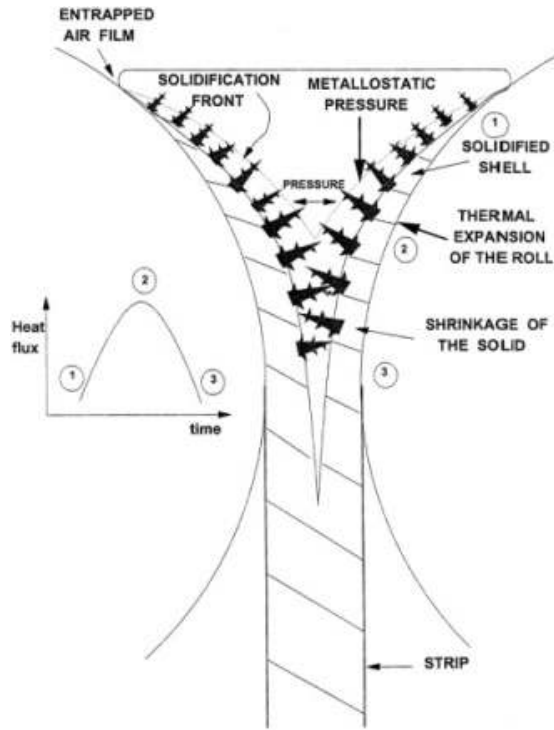


Figure 8 - Heat Flux Variation along the Roll Bite [23]

Other aspects of developing the TRC model were also explored. Ju et al. (2005) studied the effect of type and dimension of delivery nozzles on Mg twin-roll casting process. Both VTRC and HTRC processes were modelled with the assumption of turbulent flow and constant HTC. Building off of this model, Zeng et al. [6] developed a three dimensional model for the AZ31 alloy, which included flow field and temperature distribution. The authors used a turbulent flow model and a temperature dependent viscosity formula to better represent the flow in the mushy zone. The focus of this research was to observe the effects of casting speed and exit thickness on the flow field. An asymmetric casting process was modelled and a reverse flow was observed within the model and was found to decrease with an increase in casting speed. Though the current process modelled for this thesis is symmetric, this has been a staple publication in furthering the understanding of fluid flow within the TRC process. Furthermore, another conclusion that was drawn from this work was that different casting thicknesses change the velocity profiles and symmetrical profiles result in symmetrical microstructures. This can be seen in Figure 9.

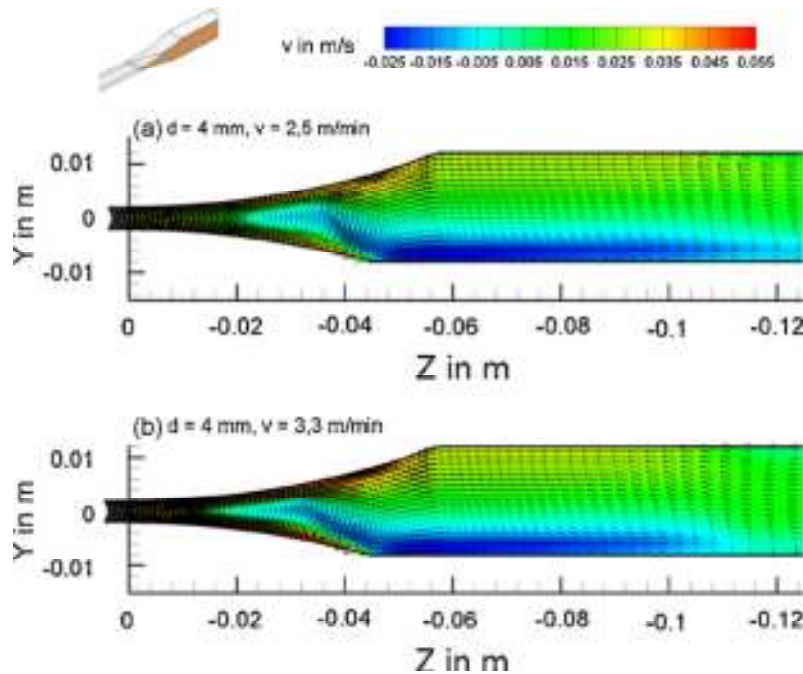


Figure 9 - Velocity Profile at Different Casting Speeds for Asymmetrical Flow [6]

The reversed flow effects were also seen in the research conducted by Zhao et al. [25]. The authors' model was developed with a constant HTC and made the assumption of a linear relationship between solidification and temperature within the mushy zone. Two symmetric vortices appeared in the generated model and the center line velocity occurred in reverse of the casting direction. It was found that this stirring effect was beneficial to the refinement of grain size.

Unfortunately, no modelling work has been done with regards to a cladding TRC system. This would be very beneficial tool since the advantages of having a clad-magnesium sheet are plentiful. A mathematical model would aid in the understanding of the interface development within the core and clad layer as well as the operating conditions in which cladding could be made possible.

2.4 Summary and Problem Statement

After assessing the needs and benefits of magnesium sheet and reviewing the background within the industry, a problem statement was developed for the current project. The scope of this project is to develop a thermo-fluid model of the twin roll casting process for the AZ31 alloy in order to

assess the feasibility of cladding with both zinc and aluminum during twin roll casting. Although POSTECH did clad magnesium successfully, they used a laboratory scale TRC hence the feasibility of a pilot scale of industry scale TRC still needs to be assessed. To determine the validity of the model developed, experimental work needed to be conducted to compare the simulation predictions to the experimental measurements. The purpose of this project is to also the effects of casting parameters on the TRC process. This is done by altering casting speed, casting temperature, and exit thickness via simulations and observing the thermodynamic impact of these changes. This document presents the development and findings of this project.

Chapter 3: Model Development

The scope of this project is to develop and use a mathematical model of the twin roll casting process including the addition of a clad layer for a magnesium AZ31 alloy. The commercial software package ANSYS-CFX was chosen as the computational fluid dynamics (CFD) software to model this process. Two different TRC geometries were simulated using CFX and included: the TRC laboratory scale unit at POSTECH University (roll diameter = 208 mm) and the TRC pilot scale unit located at CANMET's Materials Technology Laboratory in Hamilton, Ontario (roll diameter = 354 mm). This chapter explains the development, validation and, finally, use of the CFX mathematical models to assess the feasibility of producing clad TRC magnesium strips.

3.1 Governing Equations

When developing the mathematical TRC model some important assumptions need to be made. The first assumption is that the change within the physical phenomena that govern the TRC process occurs in two dimensions. The process is modelled at mid width of the cast. Because of this, heat transfer occurring across the width (Z-direction) of the cast is neglected and the model is considered two dimensional (along the X-Y plane). The second assumption is based on the fact that the twin roll casting process is symmetric in nature. Due to this concept, only the top half of the twin roll casting process is modelled. One consideration is that the stress and deformation that takes place during the process is neglected when modelling the TRC process in ANSYS-CFX. Finally, the fluid flow is assumed to be laminar. This is due to the shape of the nozzle where the molten metal is dispensed.

The physical phenomena that govern this process, which are included within the thermal-fluid model can be broken down into different sections. The activity occurring within the liquid phase of the model consists of heat transfer and fluid flow. In addition to that, the activity in the mushy zone phase

also incorporates the release of latent heat of fusion. The solid phase, as well as the contact between the AZ31 core and the roll surface, only consists of heat transfer.

The process is modelled as a steady state process. This means that the equations representing the TRC process are independent of time. The mathematical model solves the following mass, momentum and energy equations [6] in order to simulate the process:

- Mass conservation equation:

$$\frac{\partial}{\partial x_i} (\rho u_i) = 0 \quad (3.1)$$

- Momentum conservation equation:

$$\frac{\partial}{\partial x_i} (\rho u_j u_i) = \rho g_j + \frac{\partial}{\partial x_i} \left(\mu \frac{\partial u_j}{\partial x_i} \right) - \frac{\partial p}{\partial x_j} \quad (3.2)$$

- Energy conservation equation:

$$\frac{\partial}{\partial x_i} (\rho u_i C_p T) = \frac{\partial}{\partial x_i} \left(k \frac{\partial T}{\partial x_i} \right) \quad (3.3)$$

where,

u - Velocity (m/s)

ρ - Density (kg/m³)

g - Gravitational constant (m/s²)

μ - Dynamic viscosity (Pa s)

P - Pressure (Pa)

C_p - Specific heat capacity at constant pressure (J/kg°C)

K - Thermal conductivity (W/m°C)

T - Temperature (°C)

During the solidification of the AZ31 alloy, the behaviour of the fluid undergoes two important effects; change in heat transfer and fluid flow. To account for these changes the equations need to

compensate for the tremendous amount of latent heat of fusion being released and the damping of the flow rate during the mushy zone phase. Firstly, the latent heat of fusion is accounted for by modelling an equivalent specific heat equation, which can be seen in Equation 3.4:

$$H = H_{ref} + \int_{T_{ref}}^T C_P dT \quad (3.4)$$

The mushy zone consists of a mixture of a fluid and solid phase and because of this, the fluid flow is dampened. Because of this the mushy zone is considered to be a porous medium and is assumed to follow Darcy's equation, which alters the conservation of moment equation as follows:

$$\frac{\partial}{\partial x_j} (\rho u_i u_j) = \rho g_i + \frac{\partial}{\partial x_j} \left(\mu \frac{\partial u_i}{\partial x_j} \right) - \frac{\partial p}{\partial x_i} - C \frac{(1-f_l)^2}{f_l^3 + \varepsilon} (u_j - u_{r,j}) \quad (3.5)$$

where,

C - Constant of the liquid phase (between 10^4 - 10^7 for the AZ31 alloy)

f_l - Fraction of liquid

ε - Small number to avoid dividing by zero

u_r - Casting velocity (m/min)

Applying this source term allows for more appropriate fluid flow representation within the mushy zone by forcing the velocity to gradually approach the cast velocity.

3.2 Geometry

POSTECH successfully clad AZ31 magnesium sheet using their small laboratory scale TRC machine in 2009 [19]. When the POSTECH TRC facility underwent laboratory setup changes, cladding the AZ31 sheet was no longer feasible hence experimental verification of the TRC clad process was not possible. It was still decided to do more conventional TRC tests using AZ31 so that measurements could

be made to verify the model predictions. This section outlines, in detail, the different aspects of the modelling process.

3.2.1 Conventional TRC

The geometry of the model was based on the twin roll caster at the POSTECH facility. A 2D model was developed, as shown in Figure 10, taking advantage of symmetry across the mid-width position at the strip centreline. The twin roll caster at POSTECH consists of two copper rolls with a diameter of 208 mm. The strip width achievable by this caster is 150 mm. The constructed model was split into three different regions. The first region, also known as the melt region or entry, was where the AZ31 metal was still in liquid form. This represented the fluid flow of the metal travelling from the nozzle towards the rolls. The second region, known as the roll contact region, started at the point at which the liquid metal comes into contact with the rolls and continued until the metal solidifies and exits the rolls. The third region represented the exit region, where the AZ31 sheet leaves the rolls as a solid. This was also known as the solid region. Though the process was modelled in two dimensions, the CFD package requires a 3D model construction. In order to compensate, the cast was represented with extruded solids of one millimetre in width (Z-direction). However, no energy or mass transfer occurred in this direction. The symmetry of the problem also meant that entry and exit thickness values in the model were half of what they would be during actual experimentation.

Three different exit thicknesses were simulated with the POSTECH TRC reflecting the different casting conditions studied. The model was set-up with a 3.1 mm entry thickness and the various exit thickness were 0.8, 0.9, and 1.0 mm. The roll diameter was important in determining the accurate curvature of the model within the roll contact region. In order to do modeling, only the roll bite region, molten metal in the container and the exit strip are considered. The effects of the other parts of geometry are applied by defining appropriate boundary conditions.

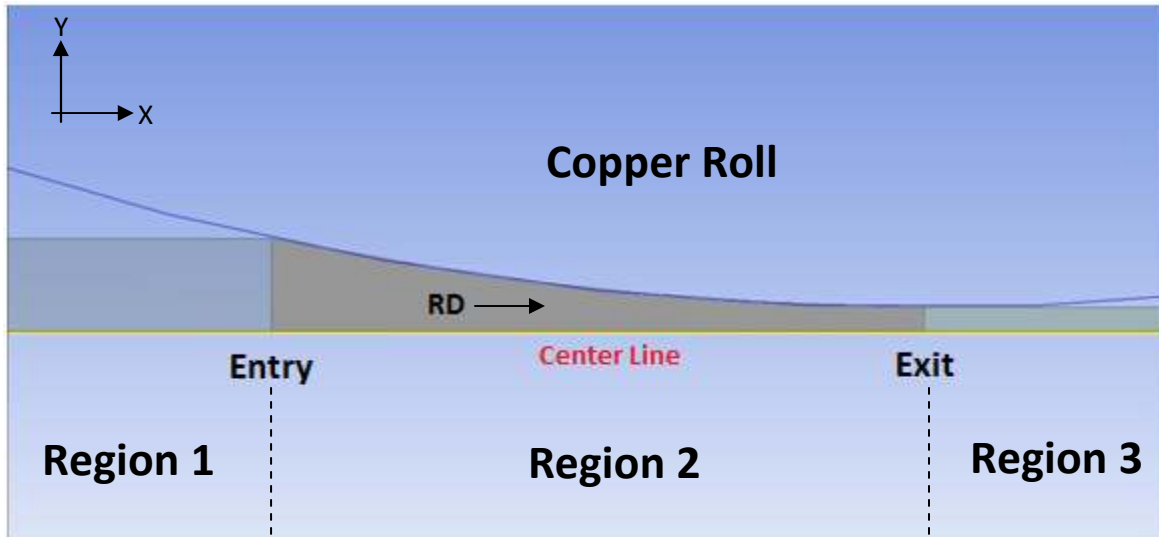


Figure 10 - Isometric View of the TRC mathematical model created based on the POSTECH facility

3.2.2 Clad-TRC Model

Since the POSTECH twin roll caster underwent lab setup changes which prevented the ability to clad during TRC, a conventional TRC model based on the POSTECH facility was created. In order to continue the investigation of the feasibility of cladding during twin roll casting, another model was developed that included a clad layer. This model was built with respect to the twin roll caster at the CANMET facility in Hamilton, Ontario. This facility was chosen to be modelled due to its close proximity to the University of Waterloo and their potential interest in this technology. Any future twin roll casting research and experimental work would be conducted at this location and could be evaluated against simulations run with this model.

The main difference between the conventional TRC model and the clad-TRC model was the geometrical difference with the introduction of a new solid domain to represent the clad layer. Unlike the AZ31 core, the clad layer is introduced to the process in the solid phase. Though the majority of the boundary conditions remain the same, introducing a new domain makes the model fairly complex. The geometry of the clad layer did not change as it passed through the rolls. Instead, the thickness of the layer was modelled as the final desired thickness. Since deformation and stress analysis was not taken

into account within ANSYS, there was no need in showing the deformation of the clad layer. Though the latent heat of fusion of the clad material was considered, any melted portion of the clad layer was not modelled as a fluid and, thus, mixing of the two domains (clad and core) was not considered. Figure 11 depicts the clad-TRC model.

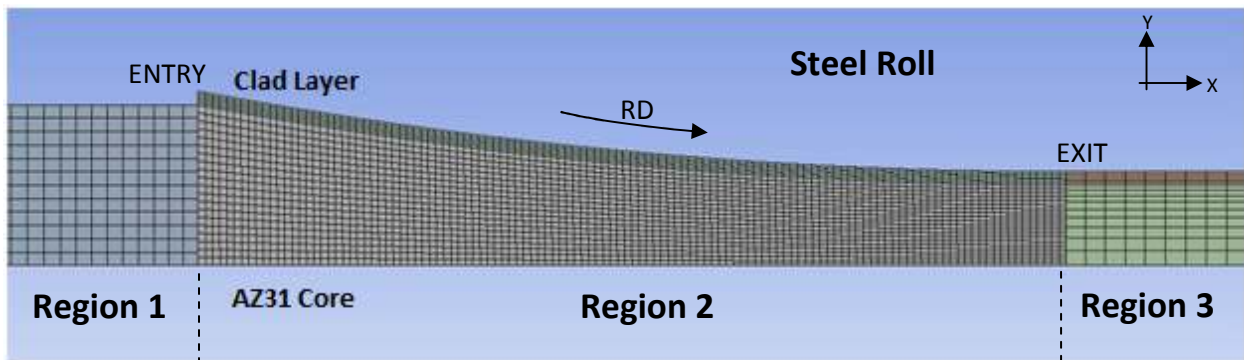


Figure 11 – Clad TRC Model

3.2.3 Mesh

The size of the mesh is an important aspect to consider when modelling the twin roll casting process. As mentioned in Section 3.2.1 Geometry, the various regions were subject to different levels of change in terms of heat transfer and geometrical change. For this, the mesh was varied spatially such that regions that underwent large variation in temperature and fluid flow had a finer mesh density than other regions that did not. In total 12,238 nodes and 5,550 elements were used during the simulations. A bias factor was used for the coarser regions (Region 1 and 3) which allowed for the elements to gradually decrease in size as they approached Region 2. This was applied in order to minimize the number of calculations that needed to be made, thus, decreasing the computational time to run the simulation.

The second region, or roll contact region, had a significantly finer mesh compared to the other two regions. The reason for this was because all of the activity within the twin roll casting process occurs at this region. The majority of the heat transfer takes place from the AZ31 core to the rolls. The change

in geometry of the core also takes place in this region, where the metal enters the rolls at one thickness and exits at another. With all of these geometrical and energy changes taking place over this small region, a very fine mesh needs to be applied in order to accurately calculate and depict the activity that takes place. The roll contact region's mesh size had 200 divisions by 20 divisions in the core and 200 divisions by 5 divisions in the clad layer. Even after taking all of this into account, the main reason the second region's mesh was such a challenge to apply was due to the fact that the phase change that occurred within the molten metal during the twin roll casting process occurred at this region. More specifically, the exact borders of the mushy zone are unknown, which causes the challenge for the computation. A significant amount of latent heat is released during solidification and a problem occurs when the border of the mushy zone passes through an element. The boundary conditions of the situation are the initial values used in the energy and momentum equations solved during a simulation. Calculations are made over the course of one element and the result becomes the initial values for the next element. When a phase change occurs in the middle of an element, its change is not fully taken into account and results in the creation of a residual in the calculation. This can be minimized by refining the mesh enough so that the location of the mushy zone boundary would, for the most part, coincide with the edges of elements. However, doing so poses a new challenge of weighing the number of elements within the roll contact region to the computational time required to perform all of the necessary calculations.

In order to overcome this, a mesh adaption was created within the CFX-Pre stage of the simulation process. The mesh adaption allows for an improvement of the resolution of flow features at specified locations. This tool helps create finer meshes without a significant increase in computational efforts. Another interesting feature of the mesh adaption tool is that the location chosen to perform the mesh adaption can be based on chosen criteria rather than geometry. This serves well with the problem that the phase change in the roll contact region poses. Even though the locations of the mushy zone

boundaries are unknown a priori, the mesh adaption can be applied when a change in material properties occurs. The variable used to determine when to apply the mesh adaption was specific heat at constant pressure. When a maximum variation in this variable occurred, the mesh adaption would refine the mesh to improve the resolution near the mushy zone boundaries.

3.2.3.1 Mesh Sensitivity Analysis

A mesh sensitivity analysis was conducted to ensure an appropriate mesh size for the simulation. Four different mesh sizes were implemented while the resulting temperature histories were compared. In order to show that the results were reliable two different boundaries were chosen to be of interest; the symmetry plane (Figure 12) and the clad-core interface region (Figure 13). Within these two boundaries six equally spaced locations were chosen for comparing temperature readings. It can be seen that based on the resulting temperature results from the various mesh sizes, the 2400 elements within the second region was appropriate enough. A smaller size would yield in a less precise result and a larger size would have simply performed redundant calculations which would yield the same result.

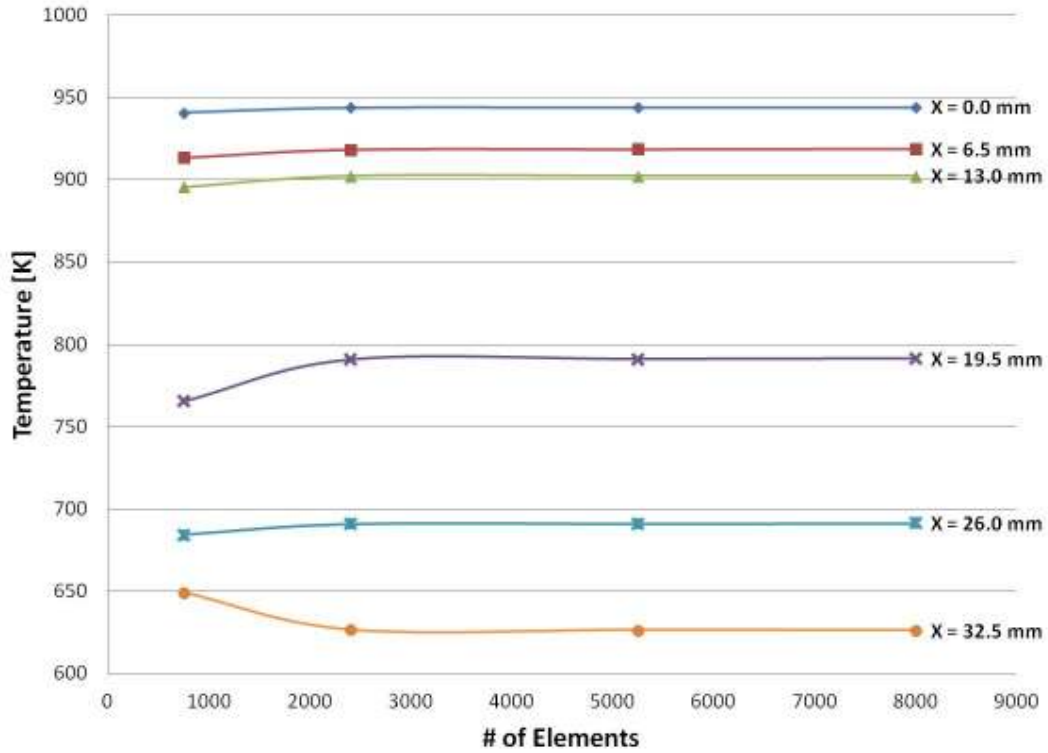


Figure 12 - Mesh Sensitivity Analysis of Temperature Readings along the Symmetry Plane

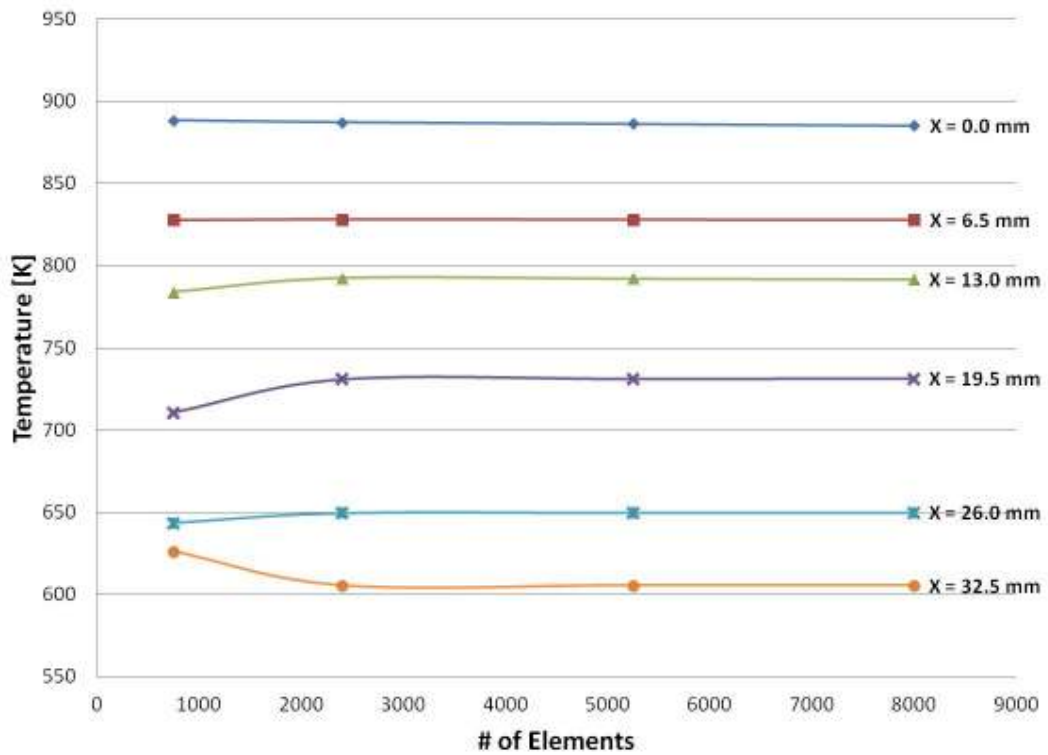


Figure 13 - Mesh Sensitivity Analysis of Temperature Readings along the Clad-Core Interface

3.2.4 Boundary Conditions

A critical aspect of the model development was quantifying the boundary conditions to describe the TRC process accurately. While the geometry controls the bounds of flow movement, the boundary conditions dictate the external conditions applied to the system. Refer to Appendix A for a complete set up guide of all of the boundary conditions in the CFX model.

Some of the process boundary conditions, as shown in Figure 14, are described below:

- Inlet (region 1): the boundary condition in this region consists of the casting temperature and a velocity. The liquid velocity is calculated from the casting speed. The inlet is located 100mm before the first contact between the melt and roll. The mass and momentum were modelled by a total static pressure set to the reference pressure of 1 atm.
- Melt container upper surface and upper part of nozzle (region 1): this region is assumed to be adiabatic and that there is a no-slip wall condition.

$$Q'' = 0 \quad (3.6)$$

where Q is the heat flux of the boundary.

- Roll/strip interface (region 2): In this region a no-slip rotating wall is defined. The heat transfer between the roll and the strip is defined using a constant heat transfer coefficient (HTC). The roll surface temperature is assumed to be constant at 27°C, due to its internal water cooling system. This boundary condition is discussed in further detail.
- Exiting strip upper surface (region 3): radiation is neglected in this region because of the low temperatures. This surface is also defined as free-slip, adiabatic wall.

- Outlet (region 3): The exit velocity is equal to the casting speed. The outlet is 100 mm away from last contact point between the strip and the roll surface. This boundary condition is further discussed.
- Symmetry Plane (centre line): the symmetry plane is considered to be a symmetry boundary with no fluid flow or heat transfer across the plane.

$$Q'' = \dot{m} = 0 \quad (3.7)$$

where \dot{m} represents mass flow rate at the boundary.

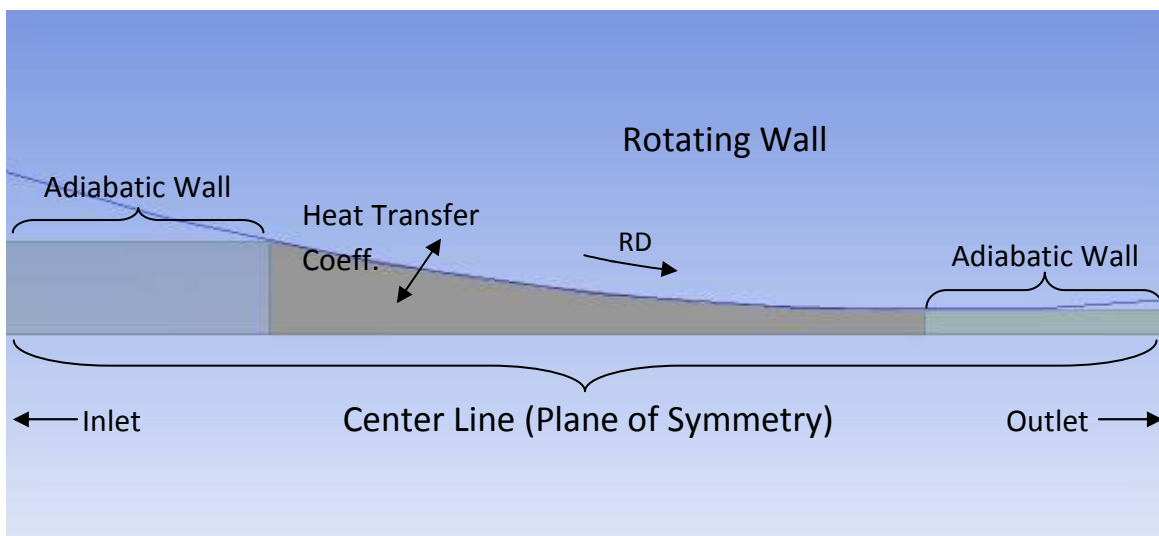


Figure 14 - Boundary Conditions of Mathematical Model

The first step in setting up the boundary conditions was to state the domain type and apply an associated material to the domain. In this case, the AZ31 core was modelled as a fluid domain despite the fact that it changed from a fluid to a solid. To compensate for this, the fluid's material properties were dynamically adjusted as the phase of the material changed. This allowed for the accurate representation of each phase in spite of the domain type selected. The reference pressure was set to 1 atm. This pressure value represented the entire domain, unless otherwise specified. The fluid flow was also considered to be laminar in order to decrease the complexity of the model.

It is important to note that the twin roll casting process is a steady state process. The CFD model does not consider the transient (beginning and end) portion of an actual experiment and only focuses on the steady state part of the process. It is also important to note that many of the boundaries considered as adiabatic walls or planes of symmetry are not an exact representation of the physical nature of the process. Though heat transfer exists from all surfaces of the cast, the amount of heat loss is negligible.

The surface adjacent to the roll, labelled as the “roll surface”, was modelled as a rotating wall. This is where all of the heat transfer took place within the model. Since the rest of the surfaces were, either, adiabatic walls or symmetry planes, the only location for any heat transfer to take place with respect to the external environment was through this surface. During the twin roll casting process, the rolls play two parts; they act as the primary source of cooling and they dictate the cast speed. The rolls, in turn, must be modelled with both of those aspects in mind. As a rotating wall, the roll surface was given an angular velocity as well as a heat transfer coefficient. The angular velocity was inputted from the coordinates of where the center of the roll would be located. The heat transfer coefficient is further discussed in section 3.2.4.1.

For the clad-model the interface between the clad and core was only modelled for heat transfer and did not include any mass transfer. This was due to the fact that the clad layer needed to be modelled as a solid domain because of software limitations. This prevented any mixing between the clad and core materials.

The “Outlet” surface of the domain is located at the opposite end of the domain where the mass flow ends. The boundary conditions at this location model the flow regime as subsonic as well. The mass and momentum are modelled as an average static pressure over the entire outlet. The relative pressure was kept at 0 Pa, keeping it equivalent to the reference pressure. In accordance with setting the mass and momentum option to ‘Average Static Pressure’, a pressure profile blend value must be set. This

value is a measure of enforcement of the specified pressure profile. The pressure at the outlet is determined by the following equation

$$P = \theta \times P_{profile} + (1 - \theta) \times P_{floating} \quad (3.8)$$

where θ represents the pressure profile blend, $P_{profile}$ is the pressure value calculated from the user-specified profile and $P_{floating}$ is the value of the pressure just upstream of the outlet. The pressure profile blend value was set at 0.05 having minimal enforcement at the outlet boundary.

As previously mentioned, the POSTECH twin roll caster was modelled as a fluid domain despite the fact that the fluid undergoes a phase change where it transitions into a mushy zone and, finally, a solid strip. This phase change was initially taken into account using different viscosity values. The values for viscosity were altered based on the temperature calculated at each node. Though, theoretically, this helped distinguish a different behaviour of the flow when it started to solidify, preliminary results proved otherwise. The changes in viscosity negatively impacted the flow rate to the point where flow velocity vectors pointed in all directions indicating a chaotic turbulent flow. The velocity vectors of the flow rate were highly unorthodox and deemed the results of the model inadmissible. As an alternate solution, the source term, previously mentioned in section 3.1, was introduced within the CFX-Pre boundary conditions in order to regulate momentum of the mass flow. Equations to illustrate the motion of the mass flow were created in the X and Y Cartesian coordinate directions. The momentum equations were derived to be a function of the solid fraction and cast velocity in order to determine how the mass flow would behave with regards to its solid fraction. This allowed for a better representation of the flow behaviour and a better velocity vector distribution as well. The difference in velocity flow fields between the two methods can be found in Figure 15. The equations and source term settings can be found in Appendix A.

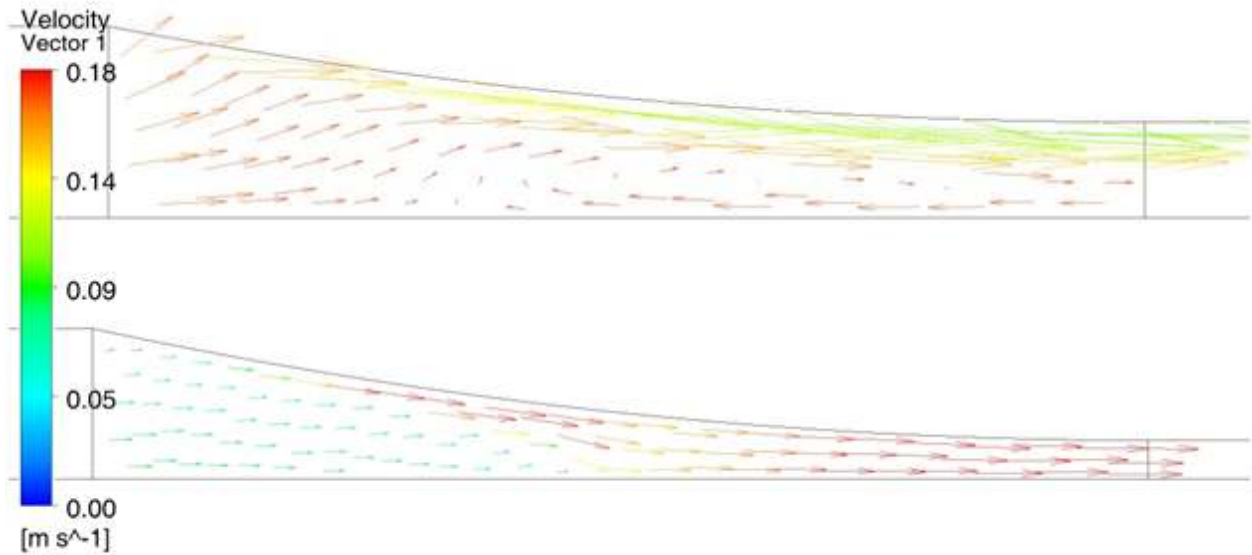


Figure 15 - Fluid Flow Velocity Profile Comparison: Top - Without Source Term, Bottom - With Source Term

3.2.4.1 Heat Transfer Coefficient

The most important and least well known boundary condition is the HTC between the strip and roll surface. Research has shown that the HTC is a roll pressure dependent value and hence can vary spatially in the contact region. In this study, however, a preliminary assumption of a constant heat transfer coefficient was made. An $HTC=20kW/m^2C$ (spatially constant in the contact region) was assumed for the POSTECH model, which consisted of copper rolls and an $HTC=10kW/m^2C$ was used for the CANMET facility based clad models, which consisted of steel rolls. This boundary condition plays such a significant role in the overall temperature profile of the model due to the fact that it dictates the rate at which heat is extracted from the model as it passes through the rolls.

Considering the fact that the POSTECH and CANMET twin roll casters both have rolls made up of different materials, it can be assumed that the correct heat transfer coefficient to be used during simulations would be different for each model. Though the HTC equation is not a function of any thermo physical properties, the heat dissipation rate is dependent on material properties. This implies that the HTC will vary depending on the materials involved. Another factor that influences the HTC is the

pressure. As the cast passes through the rolls, the pressure exerted varies along the roll from the point of contact to the “kissing point”, or the point at which the maximum deformation of the cast occurs. A large spike in the heat transfer coefficient is predicted to occur at the “kissing point” due to the drastic increase in pressure. During the twin roll casting process, an air gap between the cast and the rolls is always present. The pressure induced by the rolls helps reduce the size of this air gap. Since the pressure at the “kissing point” is at its highest, the size of the air gap present at this location is at its lowest, in turn, resulting in a higher heat transfer coefficient. This implies that the HTC is not constant throughout the twin roll casting process. However, to simplify the model a constant HTC was used and is considered a reasonable assumption as noted in the literature.

3.2.5 Material Properties

The material chosen was AZ31 which was not an alloy listed within the ANSYS material database. For this reason, the material had to be created as a user specified material. All of the material properties, such as density, specific heat, thermal conductivity, etc., needed to be inputted into the database. The complete list of all the material values can be found in Table 4. Values for specific heat, conductivity and liquidus and solidus temperatures were inputted based on values obtained from previously published literature. The solid fraction values were determined using Scheil cooling calculations of solidus and liquidus temperatures obtained within the literature. The material properties of the specific clad material chosen for each simulation were inputted in a similar fashion.

Table 4 - Material Properties of AZ31 [23]

Property	Value/Function							
Density, ρ (kg/m ³)	1780							
Latent heat of fusion, L (J/kg)	340000							
Specific heat, C_p (J/kgC)	$820 + (0.79 \times T) - (3.6 \times 10^6 / (T - 225)^2)^*$							
Thermal conductivity, K (W/mC)	50°C	100°C	200°C	300°C	400°C	566°C	630°C	650°C
	83.9	87.3	97.0	101.8	107	118.5	60	120
Solidus, T_s (°C)	566							
Liquidus, T_l (°C)	630							
Dynamic Viscosity, μ (Pa s)	0.001							

3.3 Solver

The solver control part of the modelling process is one of the most important aspects when conducting simulations. When a simulation is conducted, calculations are performed to determine a solution for different variables. The various variables that undergo these calculations are mass transfer, momentum in the U, V, and W direction and, finally, enthalpy. The solver control settings are what determine the length of time, or number of iterations, to run a simulation and the timescale or intervals to perform calculations. The goal of the solver stage of the simulation process is to repeatedly calculate all equations until the residuals of each variable reach a user-specified convergence criteria. The convergence criterion is a small value, usually set at 10^{-4} , in order to ensure accurate results. The importance of the solver control step is simply due to the fact that the values used for the settings can significantly dictate whether or not the simulation would reach convergence.

The number of iterations determines the number of times calculations are made in order to help reach convergence of the different solver criteria. It is vital to ensure that the number of iterations is set to a high enough value so that the simulation has sufficient number of calculations to converge. It is also important to set the number of iterations to run the simulation for a long enough time period for the problem to reach steady state. Though the entire model is simulated in steady state, all simulations are obtained by a transient evolution of the flow from initial conditions to the steady state conditions set by the user. This, however, is not usually a problem since the problem will reach a steady state before it converges.

The timescale determines how frequent calculations are performed. Adjusting this value could potentially change the behaviour of the solution from being noisy and having an inability to converge to a smooth, converging solution. Unfortunately, using a certain timescale value for one simulation may not necessarily be fitting for another simulation under different casting parameters. Because of this,

each experiment had its own unique solver control criteria to reach convergence. If the time scale is too large then the simulation may not be able to capture sudden changes within the system and, thus, the solution will not converge. On the contrary, if the time scale is too small then the simulation will take very long to converge or, more importantly, may not allow for sufficient relaxation for the solution and result in non-convergence.

Along with the convergence of the momentum and energy equations, the percent error of these variables is also something that dictates the accuracy of the solution. Essentially, the convergence of the solution refers to the residuals of each of these variables from calculation to calculation. The percent error expresses the difference between what goes in the system and what comes out, whether it be mass or energy transfer. The percent error is deemed acceptable if, by the end of the simulation, the value is no higher than 5%. The convergence and percent error are criteria to help assess the accuracy of the resulting solution from the simulation run.

Chapter 4: Experimental Procedure

This chapter describes experiments conducted at POSTECH University in Pohang, South Korea. The initial goal was to obtain cast samples of zinc or aluminum clad AZ31 sheet using the twin roll caster (TRC). As mentioned in the literature review, POSTECH University was chosen as the primary facility to complete these experiments as previous cladding experiments were successful at this university. Unfortunately, changes in the POSTECH University lab Twin Roll Caster (TRC) setup prevented the insertion of a clad layer during the casting process. As a result, a series of non-clad TRC sheet were cast so that the effects of superheat as well as exit strip thickness could be assessed. The material also provided a means to validate the mathematical model developed of the TRC process. Nine different experiments were conducted at the POSTECH facility and the superheat and exit strip temperatures were used as the controlled variables. Table 5 provides details of the different experiments.

After casting the sheets were cut so that the microstructure could be examined and characterized. Characterization included measurements of the secondary dendrite arm spacing (SDAS) in the centre region of the strip as this would be directly related to the cooling history experienced by the sheet. This parameter was then used to validate the mathematical model by comparing predicted SDAS values to measured values.

Changing the initial temperature of the metal changed the amount of thermal energy that needed to be extracted from the cast. Similarly, modifying the casting speed altered the speed at which heat needed to be extracted from the metal in order for the cast to still be successful. However, since the heat extraction rate is generally constant, accommodating for the consistency of the equipment, modifying the speed, essentially, changed the solidification front distance along the roll.

4.1 POSTECH TRC

The twin roll caster used at POSTECH University is a small lab scale horizontal twin roll caster. The roll diameter was 208 mm and had a width of 150 mm as well as a setback distance of 40 mm. The important difference between this caster and the CANMET facility caster was the rolls were much smaller (208 mm versus 354 mm at CANMET) and the rolls were made from copper instead of steel. This difference in roll material is very important as it will influence how much heat can be extracted from the sheet during the TRC process. This, in turn, affects the appropriate heat transfer coefficient to accurately model the interaction between the material and the rolls during the twin roll casting process. Figure 16 shows the twin roll caster used at POSTECH University. Figure 17 depicts the ceramic nozzle used during the casting of all experiments conducted at this facility. For more detailed pictures of the twin roll caster and details on the tundish refer to Appendix B.

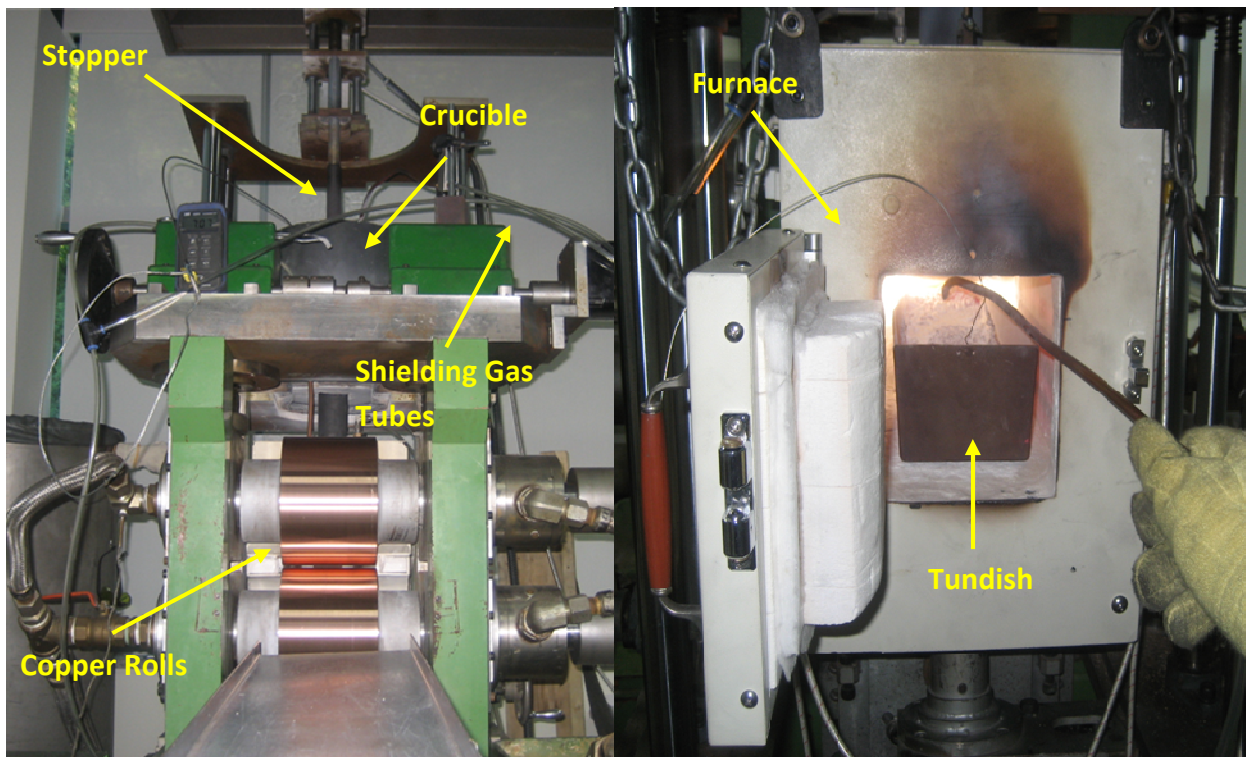


Figure 16 - Annotated picture of the horizontal Twin Roll Caster at POSTECH University

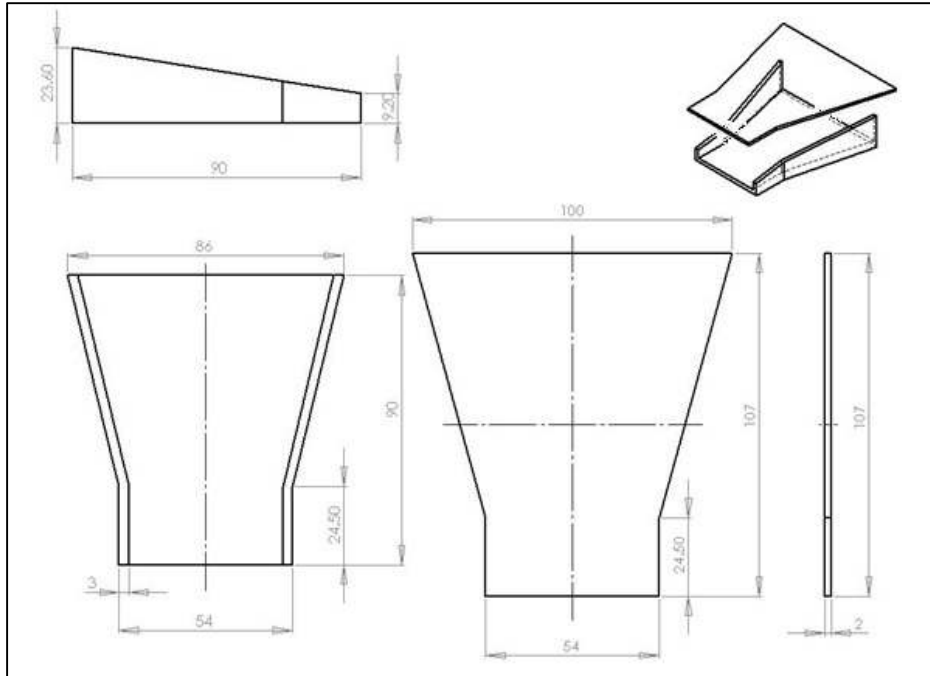


Figure 17 - Nozzle used for all conducted experiments at POSTECH University. All dimensions in mm.

4.2 Procedure

In order to conduct an experiment, operation of the twin roll caster required many steps. Depending on the casting conditions of the experiment, the appropriate exit thickness (or roll gap) and initial temperature of the cast needed to be set prior to casting. Once casting was complete, the sample needed to be appropriately labelled and cut. The caster required a rigorous clean-up process after each experiment and could only be operated, at most, once a day. For a detailed description of the casting procedure, refer to Appendix B.

4.2.1 Surface Temperature Measurements

In addition to obtaining the cast samples, some temperature measurements along the surface of the cast were desired. The reason for the temperature measurements was to help determine an accurate heat transfer coefficient that represented the situation. This heat transfer coefficient would then be implemented within the simulations conducted. At first, when it was presumed that the experiments conducted at POSTECH University would involve cladding, a preliminary plan of embedding

thermocouples on the bottom side of the clad sheet was proposed. With this approach a relatively small thermocouple with good heat resistance would have been required, as well as a long enough cord to attach to a receiver, which would be located away from the twin roll caster.

After the change for the experiments to be conducted at POSTECH University occurred, it was proposed to perform measurements of surface temperatures as the cast exited the rolls. This was going to be completed by using a hand held thermocouple probe and placing it on the cast at designated places away from the rolls. With knowing the surface temperature at certain distances away from the caster, the amount of heat loss could then be calculated. This heat loss would aid in the prediction of the heat transfer coefficient.

Unfortunately, at the time of running the experiments, the speed at which the cast exited was not anticipated which made measurements no longer possible. A total of two measurements were made at a distance of 80 cm away from the rolls and the accuracy of those measurements was questionable due to large fluctuations during the readings. The response time of the thermocouple was not fast enough and resulted in inaccurate temperature readings. Therefore, with the inability to record accurate readings, the surface temperatures were no longer recorded.

4.3 Experiment Matrix

Nine different casts were prepared using the TRC to vary both the superheat and the exit thickness. When designing the experiments and choosing the operational parameters to modify, the main factor to consider was the cooling rate that the metal undergoes. Changes in each parameter affect the cooling rate of the system and, in turn, impact the microstructure of the as-cast sample. The operational parameters that could be controlled were roll speed, initial temperature, and cast thickness. It is important to note that, usually, to ensure quality during the casting process the casting speed is constantly changed based on qualitative observations of the exiting cast. This was an important factor to

consider when planning the initial experiments. Due to the fact that these experiments needed to be recreated as a model for simulations, the roll speed needed to be held constant. This is because the roll speed is, essentially, inputted into the model as a boundary condition and cannot be dynamically changed over the course of the simulation.

The parameters that were chosen to be controlled were casting thickness and initial temperature. Three levels were chosen for each of these parameters; a low speed and thickness, a medium speed and thickness, and, finally, a high speed and thickness. The roll speed was chosen to be held constant throughout each of the experiments because it was assumed that the speed would influence the cooling rate to the point that certain conditions would not allow for successful casts. If there was a scenario where the initial temperature was high and the roll speed was fast, the AZ31 sheet would not undergo sufficient cooling for it to completely solidify. Similarly, if the initial temperature was low and the speed was very slow, the cast would solidify too early and may break as it exited the rolls. For this reason, the speed of the cast was held constant and only the thickness and initial temperature were changed. Table 5 provides a summary of the nine different experiments that were conducted.

The goal was to choose a lower and higher temperature that was physically feasible but at the same time would provide results that were significantly different in terms of microstructure. This was a challenging aspect of designing the experiments because the effects of the operational parameters had never been documented with the POSTECH twin roll caster. The thickness was also changed based on previous experience from the POSTECH students. The experiments were not optimized for quality. The purpose of this study was not to optimize the quality of the cast but to observe the effects of the casting parameters on the microstructure.

Table 5 - Experiments conducted using the TRC at POSTECH University for AZ31

Exp. #	Casting Temp. (°C)	Exit Thickness (mm)
1	710	1.8
2	730	2.0
3	730	1.8
4	730	1.6
5	710	1.6
6	710	2.0
7	690	2.0
8	690	1.8
9	690	1.6

4.4 Sample Preparation

As-cast samples were taken from the steady state region (typically near the middle of the strip length) of the cast for each experiment. When observing the microstructure of the cast, it is important to ensure that the sample of the metal is taken from a section where the cast would have reached steady state. The beginning of the cast is usually in some transient state where the quality and structure of the metal would not represent the actual microstructure based on the operating conditions. The end of the cast is in a different transient state, where only a small amount of molten metal remains and needs to be pushed through the rolls at a much faster rate in order to maintain the cast thickness. This increase of flow rate is controlled manually based on qualitative observations of the cast as it exits the rolls. Due to this, the end sections of the cast are usually of poor quality and do not reflect the microstructure of the actual cast to be expected under the specified operating conditions.

A piece from one of the middle sections was cut and mounted using a clip to hold it upright. The surface of interest was the thickness along the rolling direction. Figure 18 depicts an example of the surface under investigation for each sample. Due to the low melting temperature of AZ31, the mounting

process could not be completed using regular mounting powders. Instead, a cold mounting process was used.

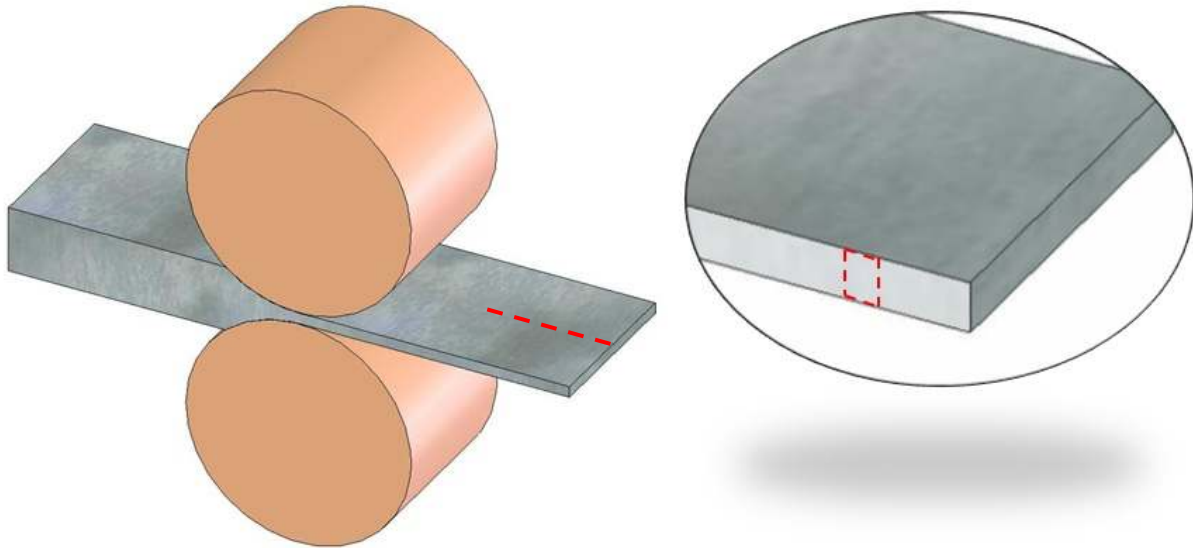


Figure 18 - Schematic of the location of interest for metallography taken at mid-width of cast

Struers' EpoFix Kit was used to mount the AZ31 samples in SeriForm mounting cups. The EpoFix consisted of 15 parts resin and 2 parts hardener (by volume). The viscous solution needed to be stirred for two minutes to ensure that proper mixing between the hardener and resin took place. During the stirring process, however, the air bubbles that were produced due to the agitation of the solution needed to be minimized. This was a very important step, especially with regards to the material that was being investigated. As mentioned before, magnesium and magnesium alloys oxidize very rapidly. One thing that can occur within the mounted sample is oxidation due to the air bubbles surrounding the material. These air bubbles, though at the side of the sample, can extend and cause corrosion on the edges of the surface of interest. This is why it is very important to minimize the number of air bubbles as much as possible. After this is done, the epoxy was poured over the samples and left to harden for 12

hours. After the hardening process, the samples were popped out of the SeriForm cups and were able to start the grinding stages. Figure 19 shows the nine mounted samples.



Figure 19 - Samples from Experiments 1 through 9 from left to right, mounted in an EpoFix cold mount and covered in colloidal graphite

4.4.1 Grinding and Polishing

To minimize the time spent grinding and polishing, three different experiment samples were placed in one mounting clip and mounted together. This meant that only three separate mounts needed to be ground and polished. Before any grinding took place, each sample was bevelled for better control during the grinding process. After this, the samples went through three stages of grinding. The three stages used 500 grit, 1200 grit-coarse, and 1200 grit-fine grinding paper, respectively. Water was used as a lubricant during this stage of the grinding process as well as to wash away debris during and after grinding. Ethanol was used as the lubricant and wash for the last two stages. The reason ethanol was used instead of water was to prevent any corrosion from occurring. Since the material for this study was AZ31, oxidation became a major factor to consider and using water as a lubricant and wash would greatly hinder the quality of the sample. After each stage of grinding, the samples were placed in an

ethanol filled beaker and placed in the ultrasonic cleaner to remove and finer debris. The samples were also cleaned with compressed air in between each grinding stage.

Each sample also underwent three stages of polishing. The first stage used the Md-Mol polishing cloth in coercion with a 3 μ m diamond stick. The lubricant used at this stage was ethanol as well. The second stage used the Md-Nap polishing cloth along with a 1 μ m diamond stick. At this stage, the lubricant was switched to a solution of, half part, colloidal silica fluid and, half part, distilled water. At this point, the samples had a scratch free, near mirror finish to the human eye. The final stage used the Md-Chem polishing pad. The same colloidal silica based solution was used at this stage as well. As similar to the grinding process, each sample was washed and placed in an ethanol filled beaker for the ultrasonic cleaner in between each polishing stage. Each sample was, again, dried using compressed air after every stage. Obtaining a mirror finish with AZ31 and magnesium and magnesium alloys, in general, is very challenging due to the fact that it is a softer metal and very easy to scratch. Upon completion of the polishing, the samples were placed in a humidity controlled chamber for corrosion protection.

4.4.2 Etching

In order to better view the microstructure of the samples under the microscope, an etchant needed to be used. According to the ASM handbooks, two different etching solutions were selected that would aid in the contrast of the microstructure. One etching solution was chosen specifically for making grain boundaries more apparent. This solution consisted of 10 ml of distilled water, 70 ml of ethanol, 4.5 g of picric acid, and 10 ml of acetic acid. In order to effectively apply the etching solution onto the sample, the specimen needed to be immersed in the solution with gentle agitation. Afterwards, the sample needed to be washed with ethanol once the face of it turns brown.

The other etching solution was chosen, specifically, to make dendrites more apparent. The recipe for this etching solution consisted of 10 ml of hydrofluoric acid and 90 ml of distilled water. For

this etching solution to take proper effect on the sample, the specimen needed to be immersed face up in the solution for 1 to 2 seconds. Proper safety precautions needed to be taken when handling the hydrofluoric acid in the dendrite etching solution. The non-latex Nitrile gloves did not provide the sufficient protection required when handling hydrofluoric acid. Special natural rubber, flock lined gloves from BEST CHEM Master were used. These gloves, once come into contact with the hydrofluoric acid, would change in colour to identify when it is time for a replacement pair. After the etchant had been applied, the sample needed to be washed in water and then ethanol and dried using compressed air. It is important to wash the samples thoroughly after etching commences. This is to remove any etching solution still remaining on the surface of the sample. If sufficient etching solution still lingered on the specimen, it would continue to corrode the metal beneath the surface until the sample became over etched and the microstructure would no longer be clearly visible.

Both etching solutions cannot be applied at the same time. In order to successfully etch the sample with the etching solutions mentioned, the etchants need to be applied separately. The microstructure needs to be observed after one etchant is used and then the samples need to undergo grinding and polishing again in order to remove the affected area of the etching solution. After this, the second etching solution can be used. Since the main objective of the experimental part of this study was to measure secondary dendrite arm spacing and, secondly, to assess the general microstructure of the as-cast AZ31. To conserve time, only the dendrite etching solution was used on the samples to get better pictures of the dendrite microstructure.

4.5 Microstructure Analysis

After the polishing and etching of the samples was completed, the microstructure needed to be observed. To fully characterize the microstructure the samples were observed under, both, an optical microscope and scanning electron microscope (SEM). The optical microscope was used for measuring

secondary dendrite arm spacing as well as looking at the overall microstructure through the thickness of the sample. The SEM was mainly used for energy-dispersive spectroscopy (EDS) to identify the composition of the phases within the samples.

4.5.1 Optical Microscopy

The microstructure of all the samples was observed under various magnifications. The overall thickness was observed under 50x magnification, while the secondary dendrite arm spacing was measured under 200x and 500x magnification. The mounted samples were levelled and observed under an ocular microscope. Figure 20 is an example of one of the images collected. From these optical micrographs, secondary dendrite arms were measured. The use of the line intercept method was considered for measuring the SDAS. Due to the fact that the microstructures consisted of columnar and equiaxed dendrites this method seemed to be very challenging to use. Instead, significant sized samples of randomly selected dendrites were measured.

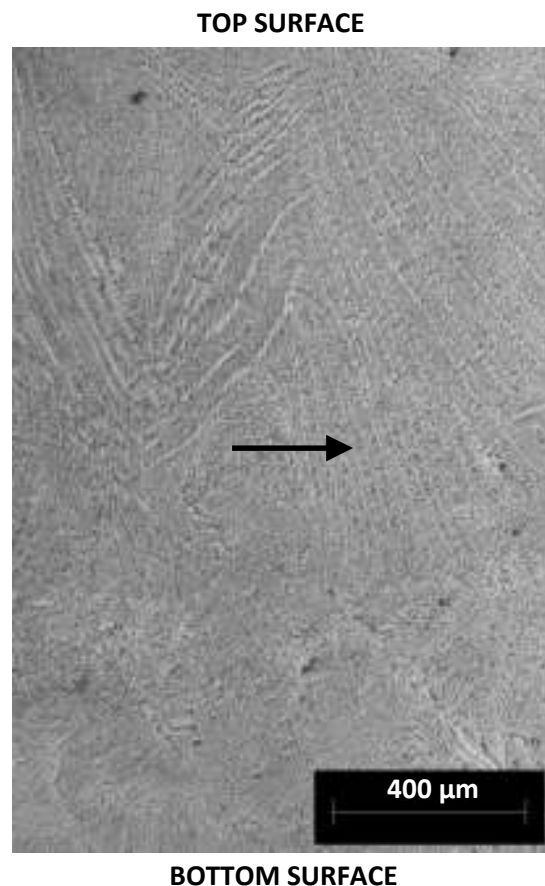


Figure 20 - Experiment 7 Sample thickness from top surface to bottom surface. Arrow refers to casting direction

4.5.2 EDS Procedure

In order to conduct the EDS analysis, certain preparation of the samples needed to take place. The scanning electron microscope operates by scanning the material using a high energy beam of electrons. Once targeted towards the sample surface, these electrons produce signals that contain details about the sample's properties and composition. This method works on the samples ability to be electrically conductive. Since the cold mounts that the samples were embedded in are not conductive, a coating needed to be applied. A colloidal graphite coating was painted all around the mount in order to make its surface conductive. This coating was gently applied to the edges of the actual samples as well. This was done so that the electrons can freely flow from the sample, through the coating, to the base of the SEM machine. Once placed in the SEM machine, the sample was analyzed in different areas and probed in places of interest to extract the chemical composition of the alloy.

Chapter 5: Results and Discussion

This chapter will explore the results from the experiments and mathematical model predictions as well as discuss pertinent trends. After completing the required experiments at POSTECH University, the as-cast samples displayed many defects. All the samples showed edge cracking, while a lot of them showed many cracks and other surface defects. Similar to Watari et al. [4], many of the cracks occur perpendicular to the rolling direction on the surfaces and are attributed to solid fraction differences and different deformation resistances. Darker regions were also visible, indicating the oxidation that took place [27] [28]. Though cracks were found in all samples, the cast quality varied greatly from experiment to experiment. This was attributed to the casting parameters of the experiments. Typically, all of the casting parameters need to complement each other in order to optimize for excellent cast quality. Experiment 4 (Casting conditions: 730°C, 1.6 mm) showed the best cast quality, while experiment 8 (Casting conditions: 690°C, 1.8 mm) showed the worst quality. Figure 21 shows the comparison of the difference in quality of the best and worst cast.

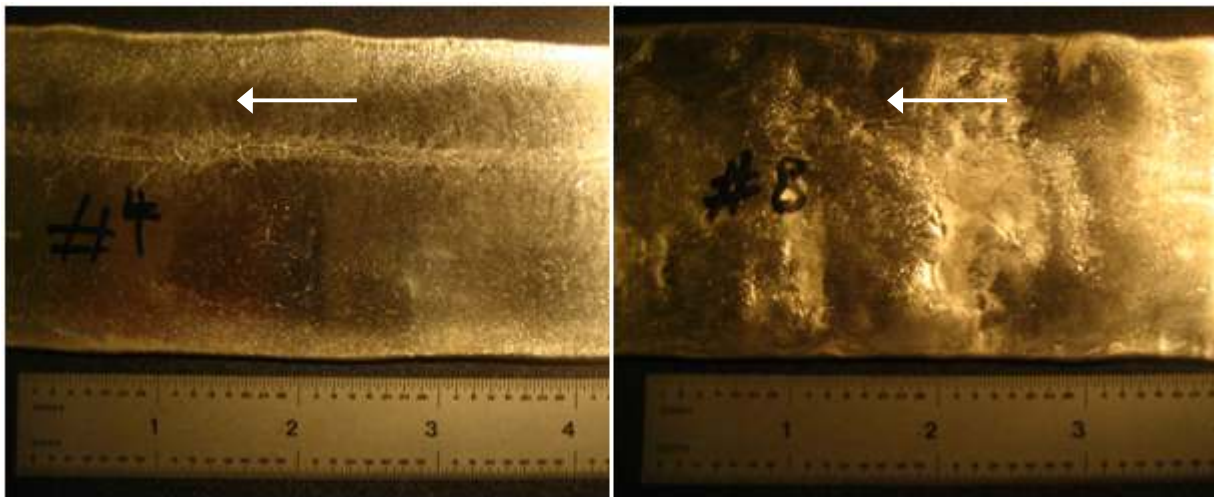


Figure 21 - Surface quality of POSTECH experiments; Left: Decent cast quality (Experiment 4), Right: Poor cast quality (Experiment 8). Scale in inches. Arrow refers to cast direction

5.1 Microstructure Analysis

This section describes the observed microstructure of the samples obtained from the nine experiments conducted as well as a generic observation of the phases present. In addition, this section further describes the secondary dendrite arm spacing values measured for each experiment for use in model validation.

5.1.1 Optical Microscopy

Observing the polished samples across the thicknesses, it can be seen that the majority of the samples show symmetry from the top through the bottom of the strip. As shown in Figure 20, the top and bottom areas of the samples, which were in contact with the rolls, showed a columnar dendritic region and an equiaxed central region. The microstructure of these regions coincides with the trends of the expected microstructure based on the thermal histories and temperature gradients experienced. Typically, higher cooling rates and lower temperature gradients result in a columnar dendritic structure, whereas, lower solidification rates and higher temperature gradients result in equiaxed dendrite formation. The former is what the molten metal experiences at the surfaces during casting and the latter is what is experienced by the middle section of the cast. In most casting solidifications, columnar dendrites form as a single front away from the mould wall. Equiaxed dendrite growth predominantly occurs in random heterogeneous nucleation sites ahead of the columnar zone. This can be seen within all the samples. Figure 22 is a sample of the thicknesses observed obtained from Experiment 5. The microstructure images of all the experiments can be found in Appendix C.

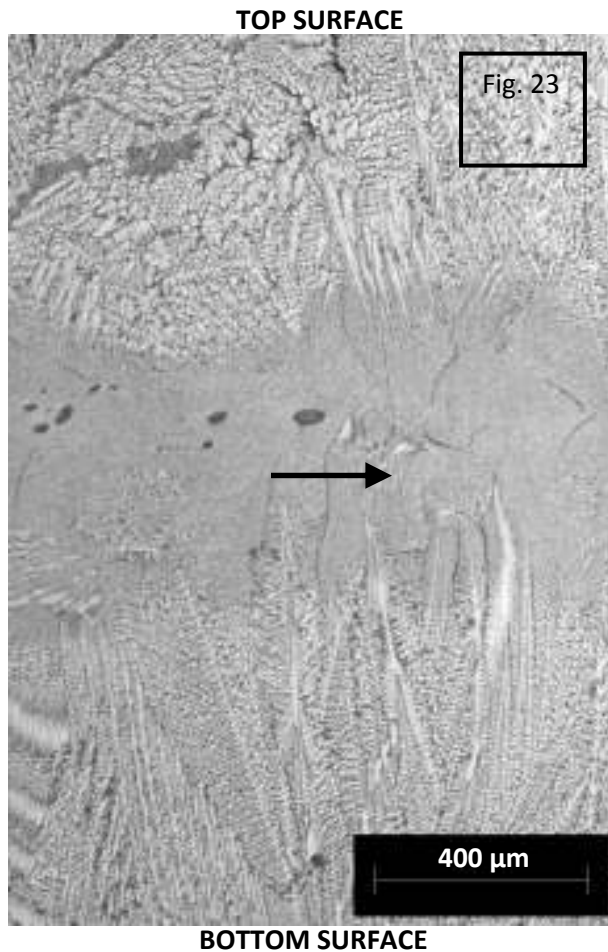


Figure 22 - Optical Micrograph of Experiment 5 at 50x Magnification. Arrow refers to casting direction

A closer inspection of the sample can be seen in Figure 23. This optical micrograph clearly shows the dendritic microstructure of the sample. In accordance with Ju et al., a very similar structure can be seen consisting of a columnar dendritic structures with fine feather like secondary dendrite arms of α -Mg. Aluminum rich solid solution is located in the interdendritic and some granular eutectic $Mg_{17}Al_{12}$ is concentrated in the center of the Al-rich regions [16]. This inter-metallic phase can be seen throughout all the samples.

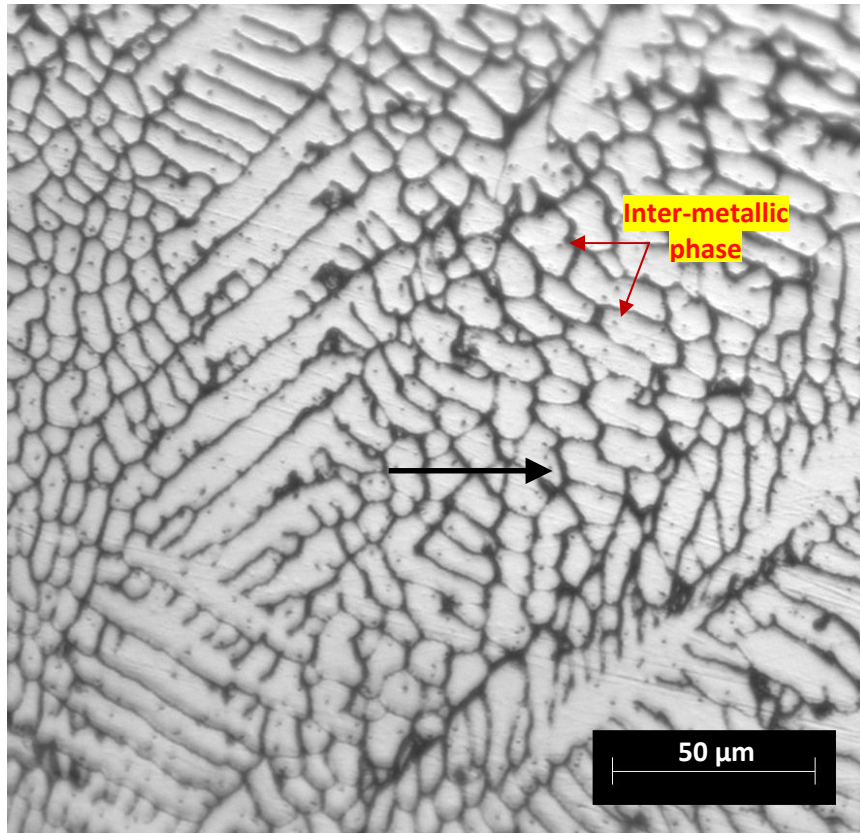


Figure 23 - Optical Micrograph of the Top Surface Columnar Dendrite Region below the chill zone at the edge of Experiment 5 at 200x Magnification. Arrow refers to casting direction

The centre-line segregation is a common and inherent defect that occurs during TRC and is related to the solidification from the surface to the centre of the strip. This is a defect that cannot be removed by subsequent thermal processing as diffusion in the solid state is relatively slow. This defect was observed in a few of the experiments conducted. Figure 24 is an example of the segregation that formed during casting. Experiments 4 (Casting conditions: 730°C, 1.6mm) and 8 (Casting conditions: 690°C, 1.8mm) clearly showed this defect.

Another observation made was the thin layer at the surfaces of each of the casts where the outer chill zone of fine grains can be seen. These results are in direct agreement with twin roll cast microstructures published in literature [16]. Figure 25 depicts the chill zone at the bottom surface of Experiment 9's cast.

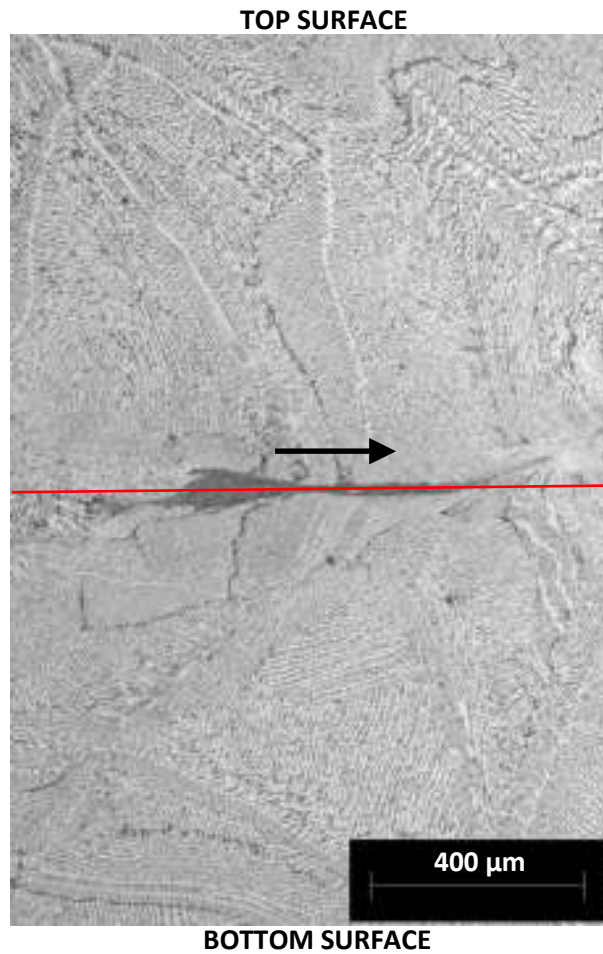


Figure 24 - Center line (red line) segregation of Experiment 4. Arrow refers to casting direction

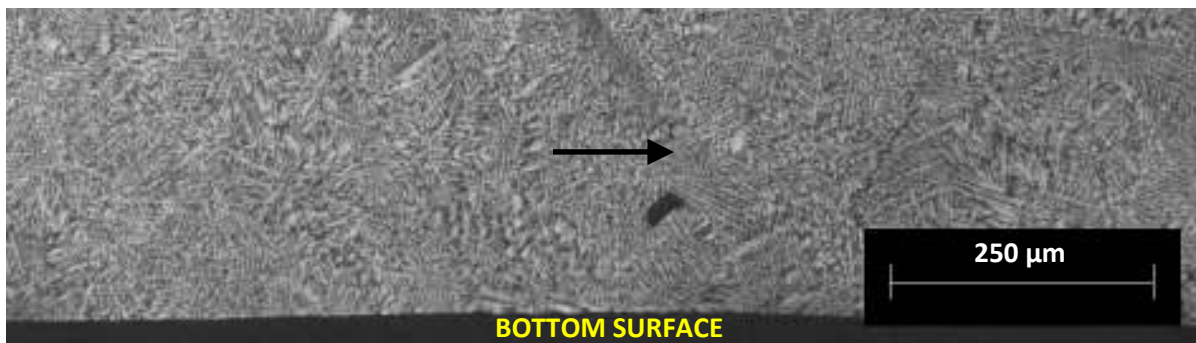


Figure 25 - Experiment 9 Bottom Surface Chill Zone. Arrow refers to casting direction

Although most samples showed similar symmetrical microstructures of columnar dendrite regions and a central equiaxed region, Experiment 3 (Casting conditions: 730°C, 1.8mm) showed some very interesting behaviour. The sample can be seen in Figure 26. The sample appears to have a granular structure transitioning into a columnar dendritic structure. An abrupt boundary can be seen where the

microstructure changes from a coarse columnar dendritic structure to a very fine columnar structure, which can be seen in higher magnification in Figure 27. As the sample was viewed towards the bottom surface, the microstructure transitioned from an equiaxed region to a columnar region at the bottom surface. For this particular sample, the equiaxed region seems to be located very close to the bottom surface and the columnar dendritic region near the bottom surface is very thin.

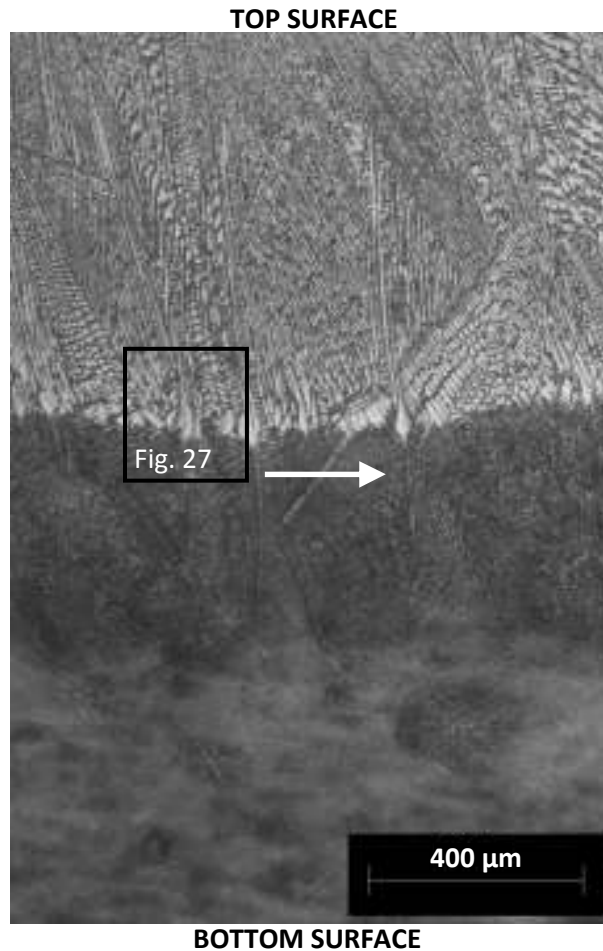


Figure 26 - Optical Micrograph of Experiment 3 Sample at 50x Magnification. Arrow refers to Rolling Direction.

The abnormal result of this sample is assumed to be attributed to asymmetric cooling during the casting of this experiment. Normally, cooling would be symmetric from the top and bottom rolls. However, in this case, if the top roll was significantly cooler than the bottom roll, a majority of the heat would be dissipated via the top surface [29]. In that case, faster cooling would occur at the top surface resulting in larger dendrite formations. Since the optical micrograph in Figure 26 depicts similar

behaviour, the reason for such a microstructural formation could be attributed to irregular cooling. However, this is considered to be strictly an assumption and requires further investigation. The results from SDAS measurements of this sample were still used to validate the mathematical model.

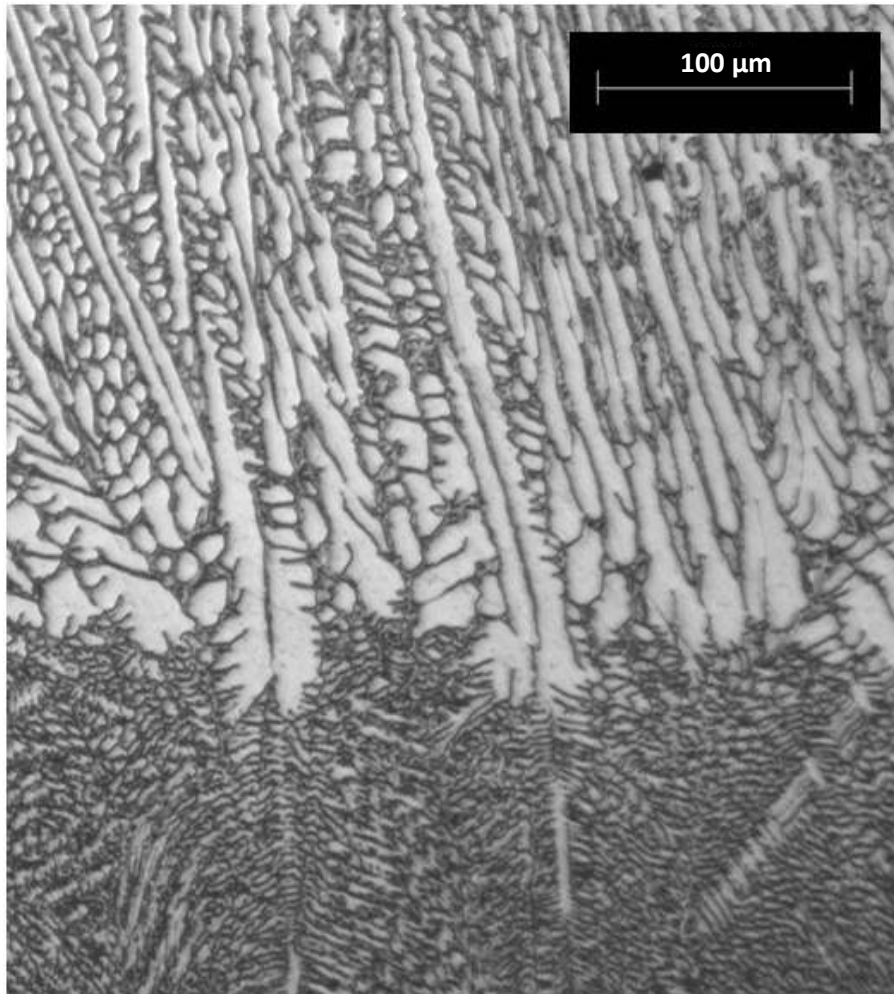


Figure 27 - Optical Micrograph of the Boundary Region in Experiment 3 at 100x Magnification

Overall, most of the microstructures seemed very similar, which indicates that the values of the casting parameters chosen were not considerably different in order to show significant microstructure differences.

5.1.2 SEM and EDS Analysis

Scanning electron microscope pictures were taken to help identify specific microstructure features for the AZ31. Although characterizing the exact composition of the samples and their relationship to the casting parameters goes beyond the scope of this project, it was desired to identify some of the general phases present. According to the magnesium-aluminum phase diagram shown in Figure 28, inter-metallic phases such as Mg_2Al_3 and $Mg_{17}Al_{12}$ can exist. All of the samples seemed to have shown similar phase distributions. EDS analysis was performed on sample from Experiments 1, 2 and 3. However, these phases could not be found. As explained by Prasada Rao et al. [19], these phases managed to come into effect during twin roll casting with aluminum cladding. Though the $Mg_{17}Al_{12}$ eutectic phase can be seen in the optical microscope, the EDS was not able to capture this exact composition.

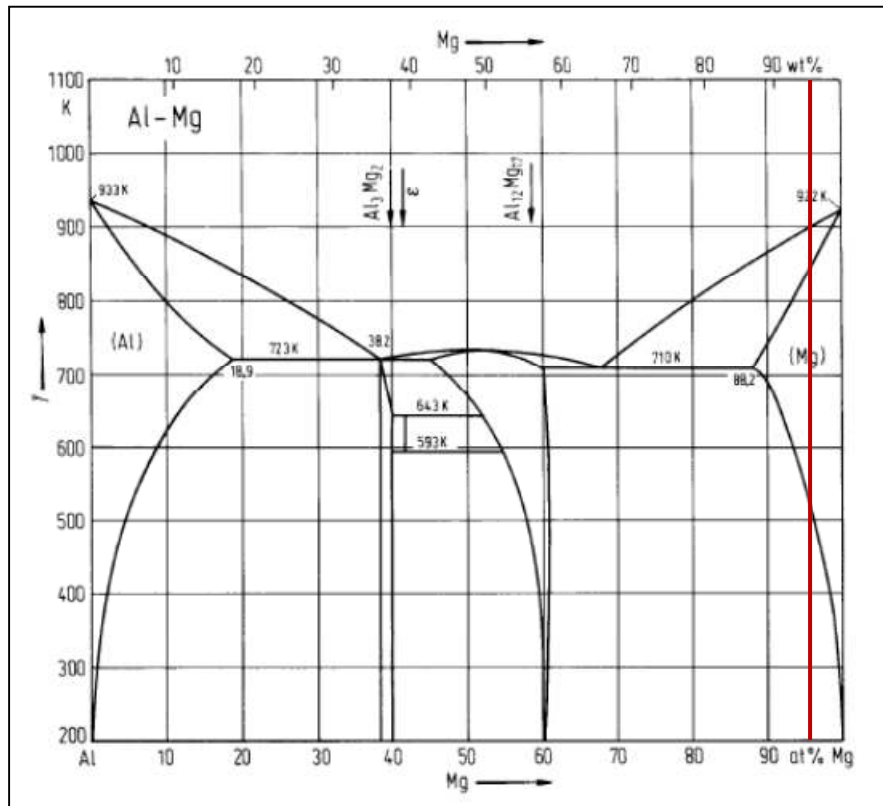


Figure 28 - Al-Mg Phase Diagram. Red line represents alloy composition [30]

Figure 29 corresponds to the SEM image obtained for Experiment 1. EDS analysis was performed in three different regions. From simply observing the SEM image by itself, it can be seen that the darker regions correspond to more aluminum and zinc rich areas due to the fact that darker regions usually correspond to heavier elements. The phases corresponding to these regions, however, could only be determined through the use of EDS. Table 6 shows the atomic percent of each element for each region. As mentioned earlier, the composition of the $Mg_{17}Al_{12}$ phase was not recognized during EDS analysis. However, a rich aluminum area can be found in Region 1. Region one shows much higher aluminum and zinc content than expected within the regular AZ31 alloy. Region 2 consists of actual AZ31 since the phase is roughly 96%-Mg, 3%-Al, and 1%-Zn. Due to the fact that region 3 has almost zero zinc content, this implies that some segregation of the aluminum and magnesium elements occurred from zinc.

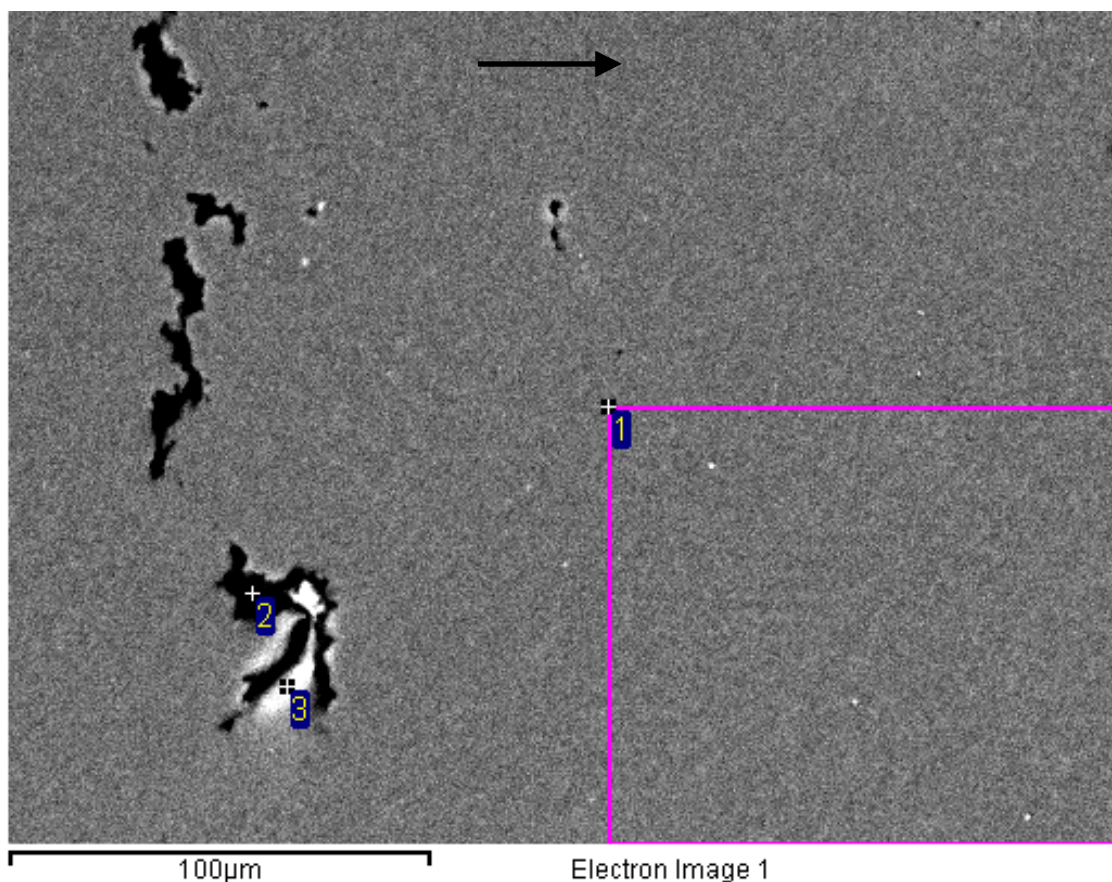


Figure 29 - SEM Image of Experiment 1 at the top Surface below chill zone. Arrow refers to casting direction

Table 6 - Atomic % of Each Element by Region

Spectrum	In stats.	Mg	Al	Zn
1	Yes	95.58	3.42	1.00
2	Yes	87.08	9.21	3.72
3	Yes	98.42	1.56	0.02
Mean		93.69	4.73	1.58
Std. deviation		5.90	3.99	1.92
Max.		98.42	9.21	3.72
Min.		87.08	1.56	0.02

5.1.3 SDAS Measurements

The measurements for the secondary dendrite arm spacing were taken under the 200x and 500x magnifications. The average SDAS was determined from the 200x magnification pictures. This was due to the fact that more SDAS could be measured in one picture with a larger area under this magnification compared to 500x. The secondary dendrite arm spacing measurements were taken at the center region of the samples. The reason for this was because all of the SDAS predictions made from the simulations were based on data collected from the center line of the models. In order for a direct comparison, the SDAS measurements should be made, approximately, at the same location.

A standard for the number of measurements to be made, to be considered statistically significant, could not be found in ASM handbooks or other standardized documentation. Because of this, the number of SDAS measurements that were made in this study was based on previous literature practices. Twenty SDAS measurements were made for each sample. Based on the literature, 20 measurements seemed like a reasonable amount to consider the measured data statistically significant [31] [32]. This was further validated with a sensitivity analysis on the impact of more measurements. The first sample underwent 10 additional measurements to ensure that the deviation in the average SDAS was not significant. The average for the first 20 measurements of Experiment 1 was $4.637\mu\text{m}$ with a standard deviation of $0.59\mu\text{m}$. The average with the 10 additional measurements was $4.639\mu\text{m}$ with a standard deviation of $0.60\mu\text{m}$, which indicates that the number of measurements made was significant enough. Figure 30 shows the measurements that were made for the first experiment under the 200x

Table 7 outlines the average measured secondary dendrite arm spacing of each sample along with their corresponding standard deviations. The equiaxed dendrites within the central regions of the samples showed clusters of dendrites of varying size. This aided in the larger standard deviations of the SDAS measurements. Rather than the average SDAS values themselves, the trends illustrate more interesting features. The average SDAS decreases as the casting thickness or casting temperature increases. It was assumed that the opposite effect would occur with respect to the trend of the casting thickness due to the fact that more energy would be present within the thicker samples. Also, a thinner sample would allow for easier heat extraction, causing higher cooling rates, which would, in turn, lower the secondary dendrite arm spacing. A further investigation of the phenomena causing such results is described within section 5.2. The trend with respect to the cast temperature followed as expected. The higher cast temperature experiments were expected to have lower secondary dendrite arm spacing since there would be a higher temperature differential, thus, inducing higher cooling rates during solidification.

Table 7 - Average Measured SDAS Values

Exp. #	Temp./Thick.	Measured Ave. SDAS (μm)	Std. Dev.
1	M/M	4.64	0.59
2	H/H	4.32	0.39
3	H/M	4.13	0.45
4	H/L	4.64	0.47
5	M/L	4.78	0.47
6	M/H	4.42	0.39
7	L/H	4.54	0.42
8	L/M	4.70	0.43
9	L/L	4.83	0.47

5.2 Conventional TRC Model Validation Results

Using the results obtained from the simulations run under the nine experimental casting conditions, the expected secondary dendrite arm spacing can be calculated. This was done using

predicted temperature and velocity data calculated at the centerline of the simulation. Using the temperature data, the locations of the liquidus and solidus (mushy zone) were determined and the corresponding velocities along that region were used to determine the solidification time of the cast during this phase. Figure 33 graphically represents this. This was determined based on the relationship between time, velocity and position. Equation 5.1 was integrated with respect to the positions where the solidus and liquidus temperatures were located at the centreline of the strip:

$$t = \int_{x_1}^{x_2} \frac{1}{v} dx \quad (5.1)$$

Using the calculated solidification time, the cooling rate can be determined using Equation 5.2:

$$R = \frac{T_l - T_s}{t} \quad (5.2)$$

The temperature vs. time curve was assumed to be linear within the mushy zone. This assumption allows for the difference between the liquidus and solidus temperatures to be used in determining the cooling rate during the solidification process and is considered an acceptable assumption based on practices within literature [25]. Finally, Equation 5.3, developed by Allen et al. for AZ31 alloys, was used to predict secondary dendrite arm spacing for cooling rates within the range of 10^{-1} to 10^6 °C/s.

$$\lambda = 35.5 \times R^{-0.31} \quad (5.3)$$

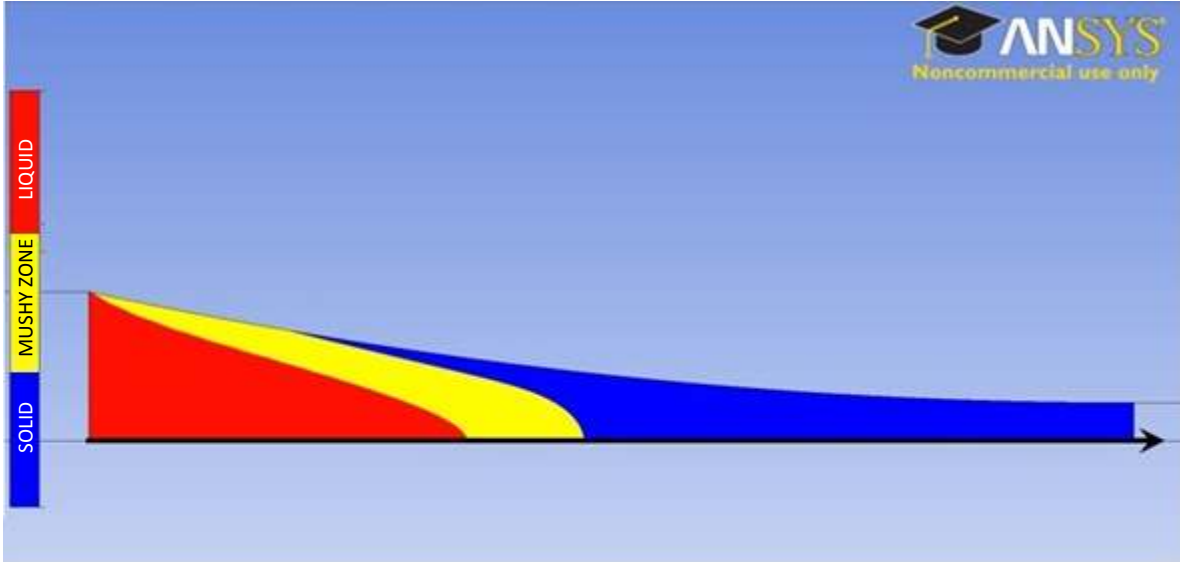


Figure 32 - Center Line Vector of Velocity and Temperature Predicted Values of Experiment 9 (Conditions: 690°C and 1.6 mm)

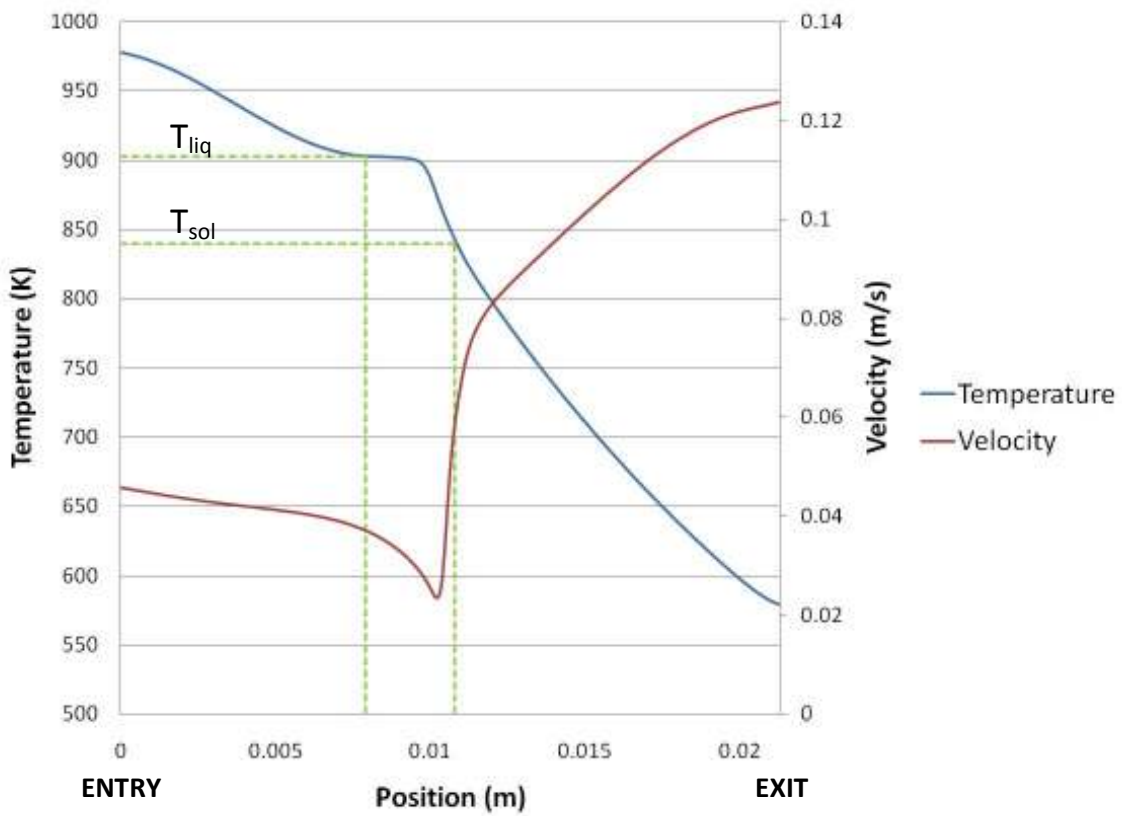


Figure 33 - Velocity and Temperature Data Collected at the Center Line of the Simulated Casts

Using Equation 5.3, the secondary dendrite arm spacing for each of the nine simulations were predicted. Table 8 shows the predicted values in comparison to the measured values for each experiment conducted.

Table 8 - Secondary Dendrite Arm Spacing Values: Predicted vs. Measured

Exp. #	Temp./Thick.	Measured Ave. SDAS (μm)	\pm 95% Conf. Interval	Predicted SDAS (μm)
1	M/M	4.64	1.18	4.66
2	H/H	4.32	0.79	4.44
3	H/M	4.13	0.90	4.56
4	H/L	4.64	0.94	4.74
5	M/L	4.78	0.93	4.89
6	M/H	4.42	0.78	4.52
7	L/H	4.54	0.84	4.65
8	L/M	4.70	0.86	4.79
9	L/L	4.83	0.94	4.97

Good agreement can be seen when the predicted SDAS is compared to those measured, which can be seen in Figure 34. Though statistically the standard deviations overlap measured SDAS averages of other experiments, this does not necessarily imply that there is no correlation between casting parameters and SDAS. The predicted values seem to show similar patterns to the measured values. The only discrepancy was with Experiment #3 which showed a 10% difference. This discrepancy corresponds to the sample showing a microstructure of what was thought to have experienced asymmetrical cooling. This discrepancy is also evident in Figure 34 skewing the medium thickness trend. However, considering that the rest of the samples have less than a 3% difference, the predicted values are within an acceptable error range. Overlooking the quantitative values, the more important aspect to consider are the trends. The predicted values seem to follow the same trends that the measured values follow. The SDAS values decrease as the cast thickness or cast temperature increases.

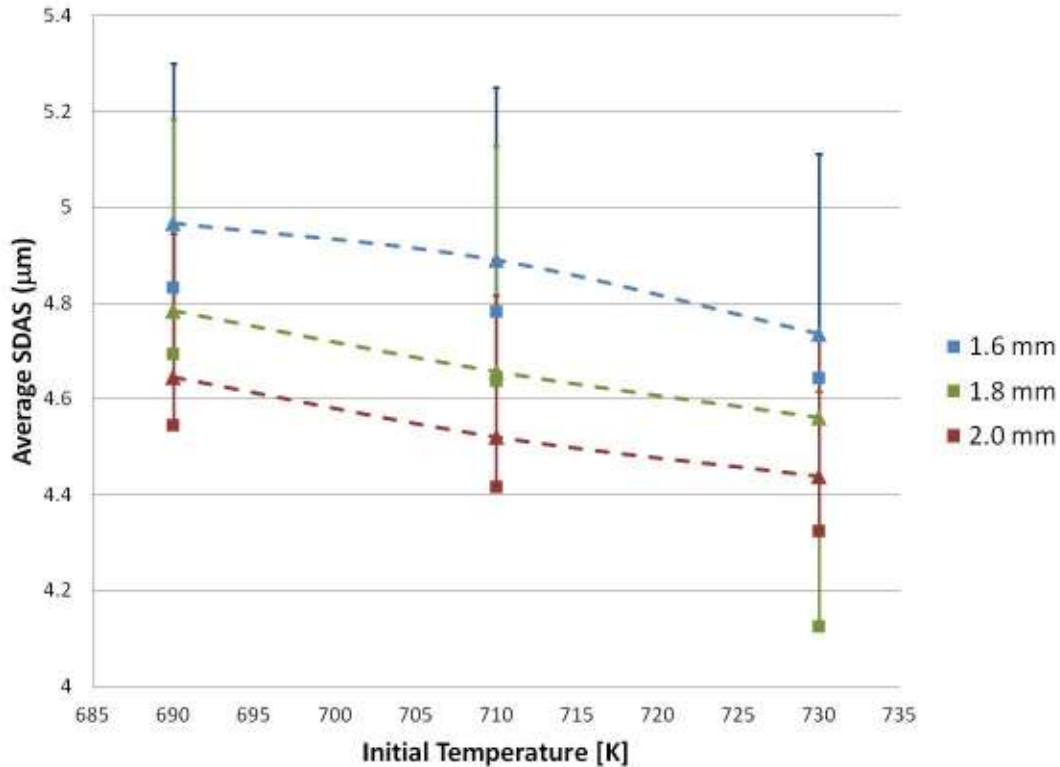


Figure 34 - Comparison of Measured (with 1 standard deviation of error) to Predicted SDAS values of all experiment cases. Dotted lines represent predicted values from simulations. Solid lines represent measured averages.

As mentioned in section 5.1.3, the trend observed with respect to the cast thickness was opposite to the expected trend. This was further investigated using the data generated from the simulations run. Figure 35 shows the temperature curve at the center line position of Experiment 7, 8, or 9 along the roll bite. It can be seen that the temperature profiles of each cast thickness follow the expected temperature trend. The 2.0 mm thick sample (Experiment 7) has the highest exit temperature. Though the slopes of the three experiments seem similar, the sections of the curves that are used for the cooling rate analysis are within the mushy zone. Within this zone, we can see different slopes for each experiment, implying different cooling rates. This effect can further be observed in Figure 36, which shows the velocity curves at the center line of the cast along the roll bite.

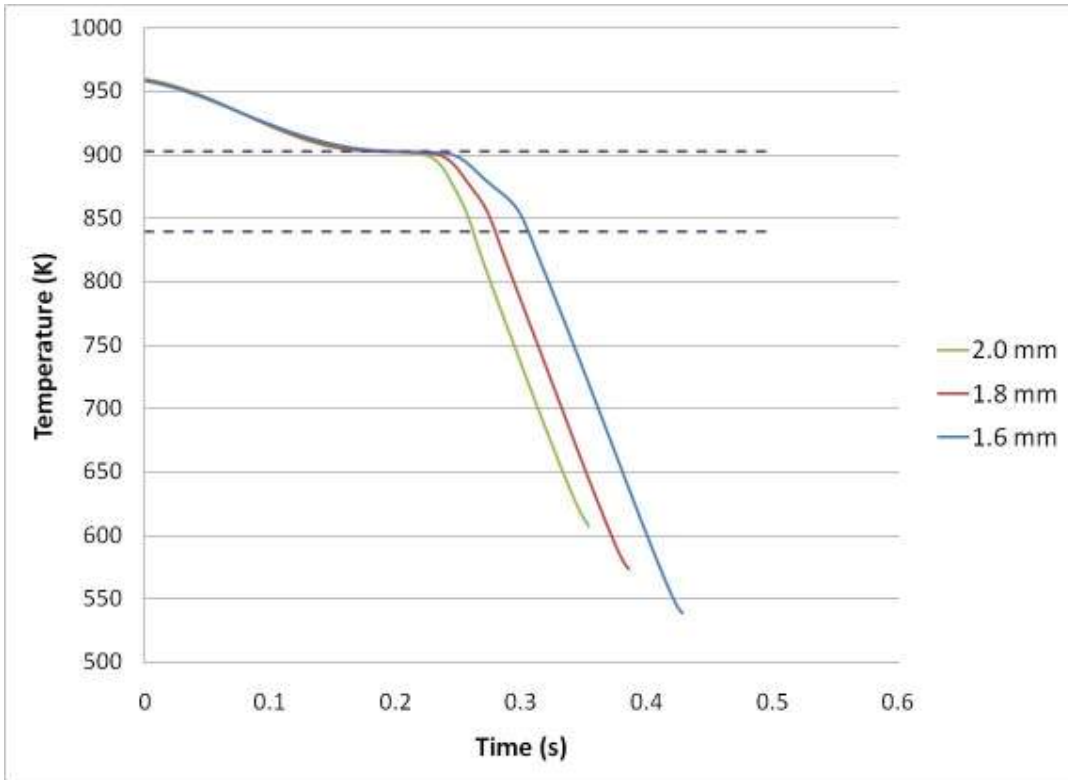


Figure 35 - Predicted thermal history for Experiment 7 (2.0mm), 8 (1.8mm), and 9 (1.6mm) cast at 690°C

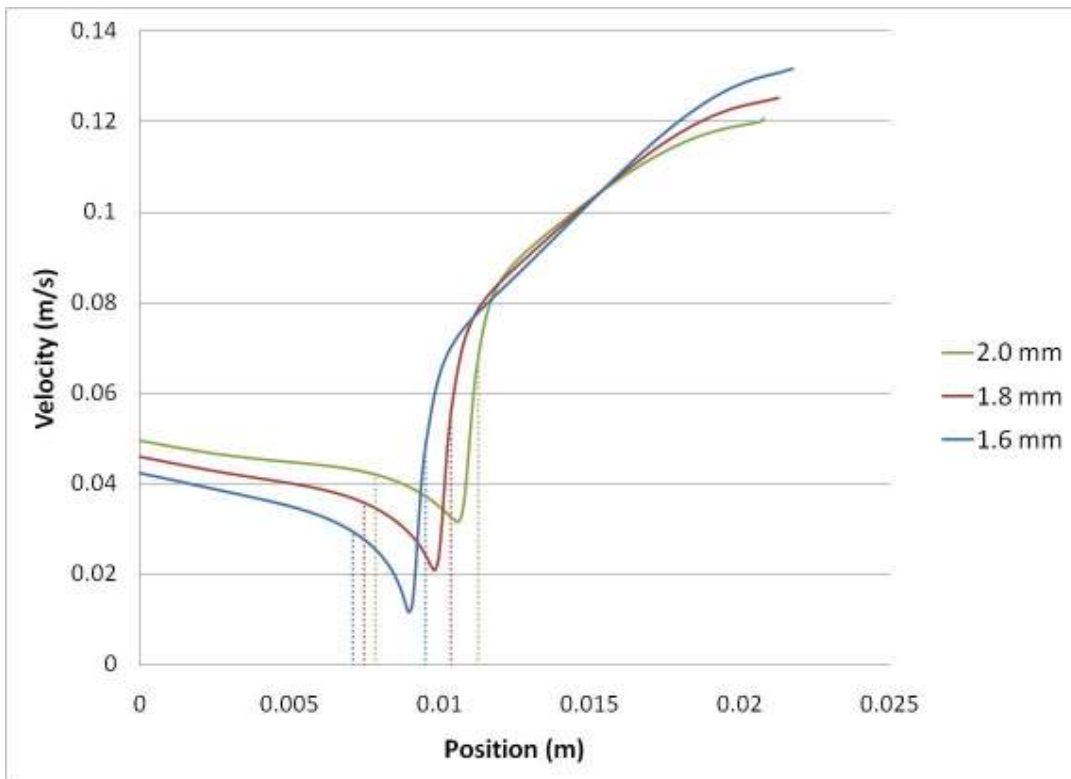


Figure 36 – Velocity Curves of Experiment 7 (2.0mm), 8 (1.8mm), and 9 (1.6mm) cast at 690°C

Figure 36 shows the velocities within the mushy zone to be higher as the cast thickness increases. Based on Equation 5.1, this trend affects the cooling rates of each experiment. Faster velocities generate faster cooling rates which, in turn, result in smaller secondary dendrite arm spacing. It can be seen that faster velocities occur within the mushy zone for thicker samples. This is simply due to a flow field stand point.

Based on the evidence provided from the experimental work conducted at POSTECH University and relative accuracy of the model simulation predictions, the model was deemed successfully validated. The validated model was then used to examine the ability of the TRC material to be clad with a solid layer of another material.

5.3 Clad TRC

This section outlines the model predictions on the feasibility of cladding TRC magnesium based on the CANMET facility. Using the validated POSTECH TRC model, a model with similar boundary conditions was created to investigate the feasibility of inserting a clad layer during the twin roll casting process. The following feasibility results strictly examine the process from a heat transfer perspective. Unfortunately no experiments could be conducted to ensure proper microstructure bonding would take place.

The simulation predictions indicated the ability of whether or not cladding could take place during the TRC process. Introducing the clad layer into the mathematical model also presented various other controlled variables. The feasibility of an aluminum and zinc clad layer was investigated. Along with this, the thickness of that clad layer and the effects of roll speed were also examined within the feasibility investigation. Overall, it was found that cladding would be feasible but under certain conditions.

5.4.1 Clad Thickness Effects

The first study involved observing the effects of the clad thickness on the temperature profile of the laminate strip during casting. This investigation involved observing the temperature along the interface between the core of the cast and the clad layer. The temperature profile within the clad showed how much melting would occur throughout the clad layer. The amount of melting within the clad layer is very important because it dictates the appearance of the resulting cast. The overall goal of cladding is to ensure that the exiting cast has a fully coated surface of the clad material. If significant melting occurs, the clad and core materials would undergo mixing and the exiting cast may not be completely coated with a clad layer. However, if insufficient melting occurs then the clad layer and the core may not form a strong metallic bond. The clad thickness was expected to affect the amount of melting the clad layer experienced. Three different clad thicknesses were simulated; 0.5 mm, 1.0 mm, and 1.25 mm. In reality, the clad thickness would most likely be no more than 0.5 mm but these clad layer thicknesses were chosen for theoretical purposes. Figure 37 shows the resulting temperature profile of each of the different clad thickness simulations run. It can be seen that the temperature at the surface of the cast is lower for the thicker clad layers. The temperature of the clad material decreases from the interface through to the tops surface in direct contact with the rolls.

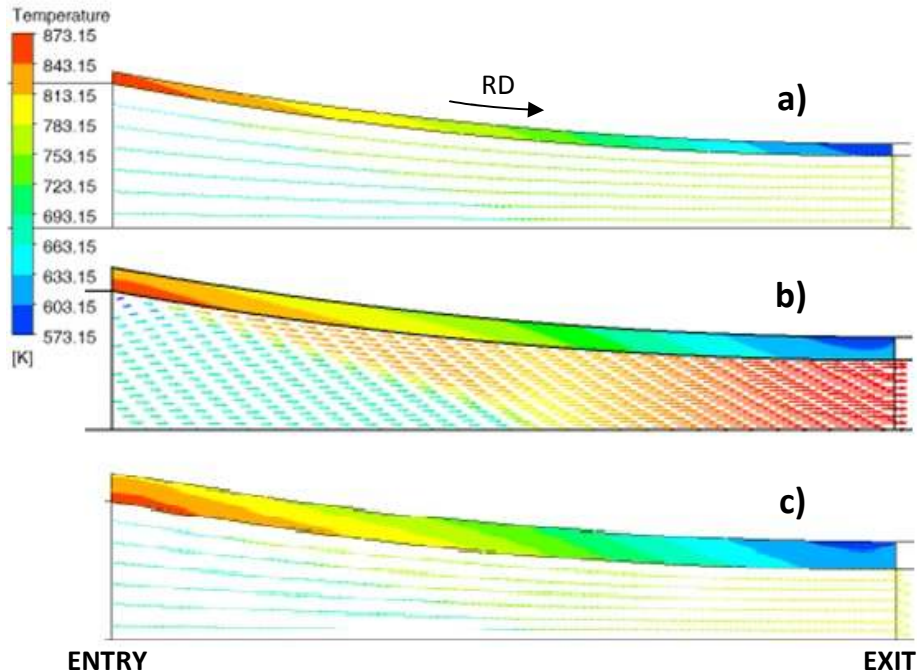


Figure 37 - Various Zn Clad Thickness Temperature Profiles: a) 0.5 mm, b) 1.0 mm, c) 1.25 mm. AZ31 core exit thickness: 2.5mm with roll speed of 1.7 m/min.

This study showed that the thickness of the clad sheet did not greatly affect its temperature distribution and changing this variable is not a realistic option. The clad layer would have to be greatly increased to see the benefit of thicker clad materials. This is because the gradient along the thickness of the clad sheet is not very large. For example, if under a certain set of casting conditions, a 0.5 mm clad layer showed 100% melting, then in order to operate at those same conditions while still maintaining a solid surface, the clad thickness may have to be increased to 300% or 400% of the value. This poses a problem in using the clad layer thickness as a controlled variable during casting because an upper limit to the thickness of the clad layer exists. Realistically, a clad layer should be no more than 10% of the core thickness. The majority of the exiting sheet should consist of the AZ31 cast.

5.4.2 Casting Speed

The next parameter investigated was the effect of casting speed on the thermal history of the clad material. For this study two different clad materials were chosen; zinc and aluminum. The clad thickness and casting temperature were held constant at 0.5mm and 950K, respectively. The different

casting speeds ranged from 0.9 - 3.0 m/min. Figures 38-40 show the thermal history of the aluminum and zinc clad layers, as well as the AZ31 core for a casting speed of 0.9, 1.7, and 3.0 m/min. The temperature profiles are coloured to represent the phases (solid - blue, liquid - red and semi-solid – yellow).

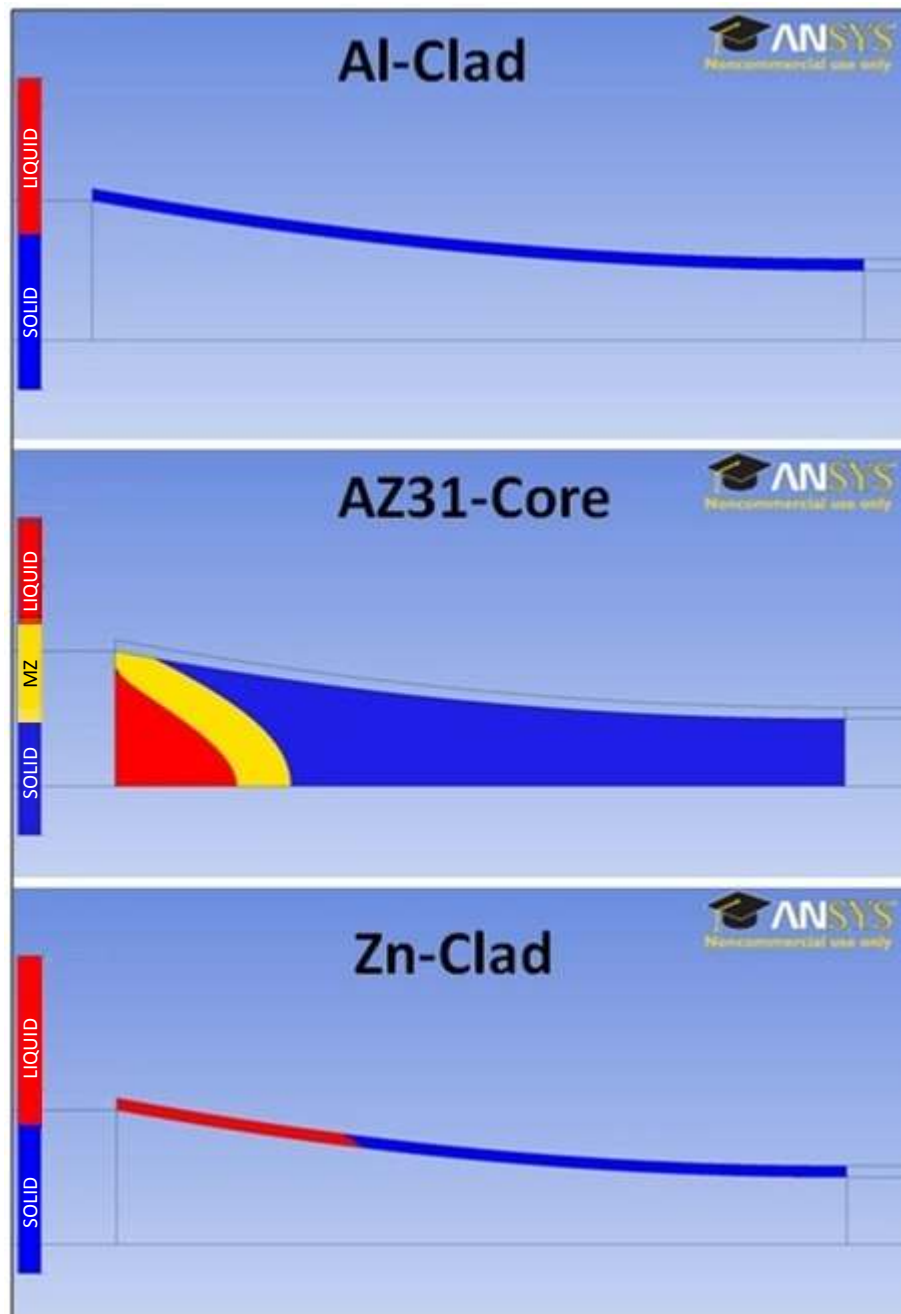


Figure 38 - Temperature Profile of Clad (AZ31) and Core (Al and Zn) at 0.9m/min casting speed

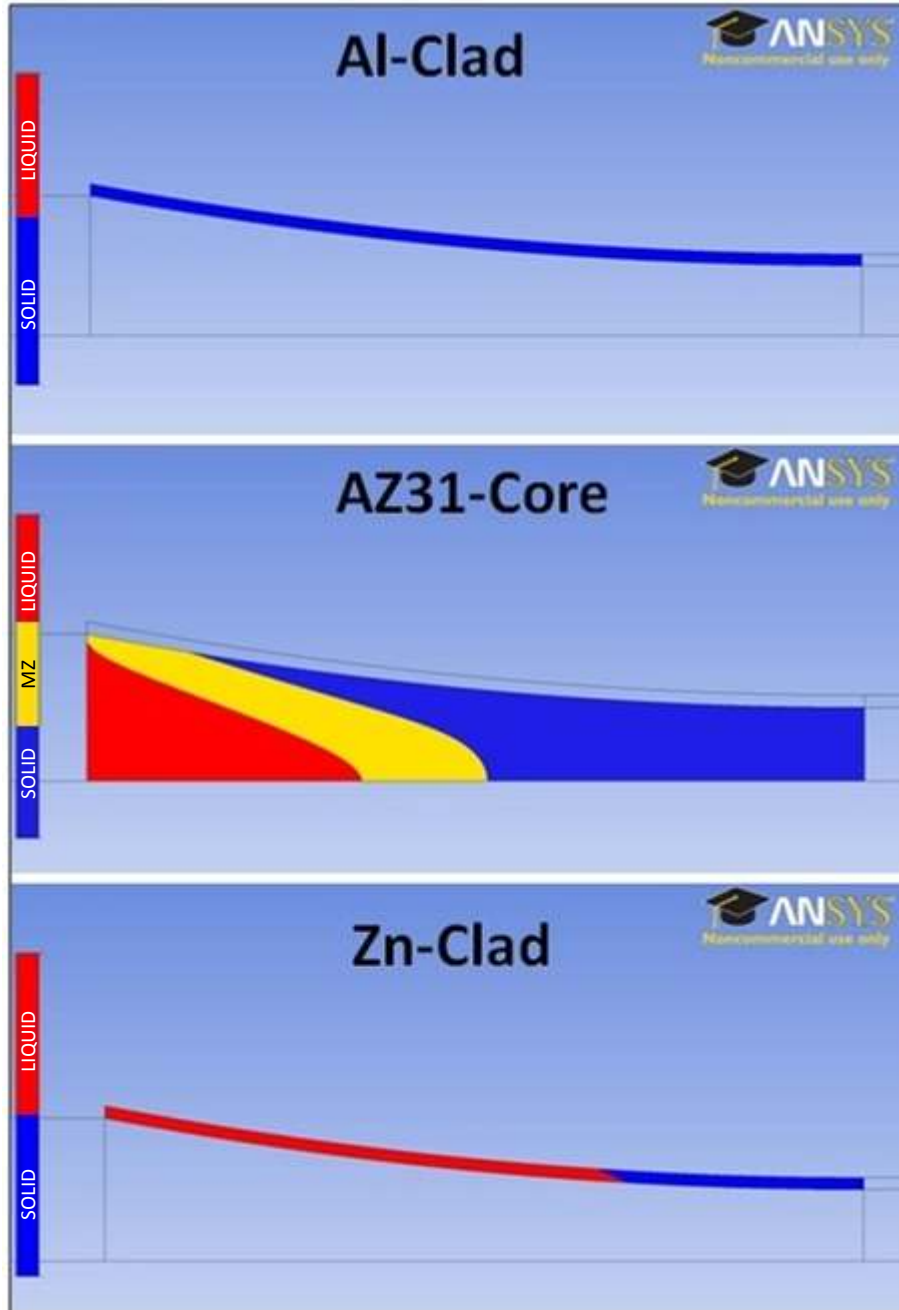


Figure 39 - Temperature Profile of Clad (AZ31) and Core (Al and Zn) at 1.7m/min casting speed

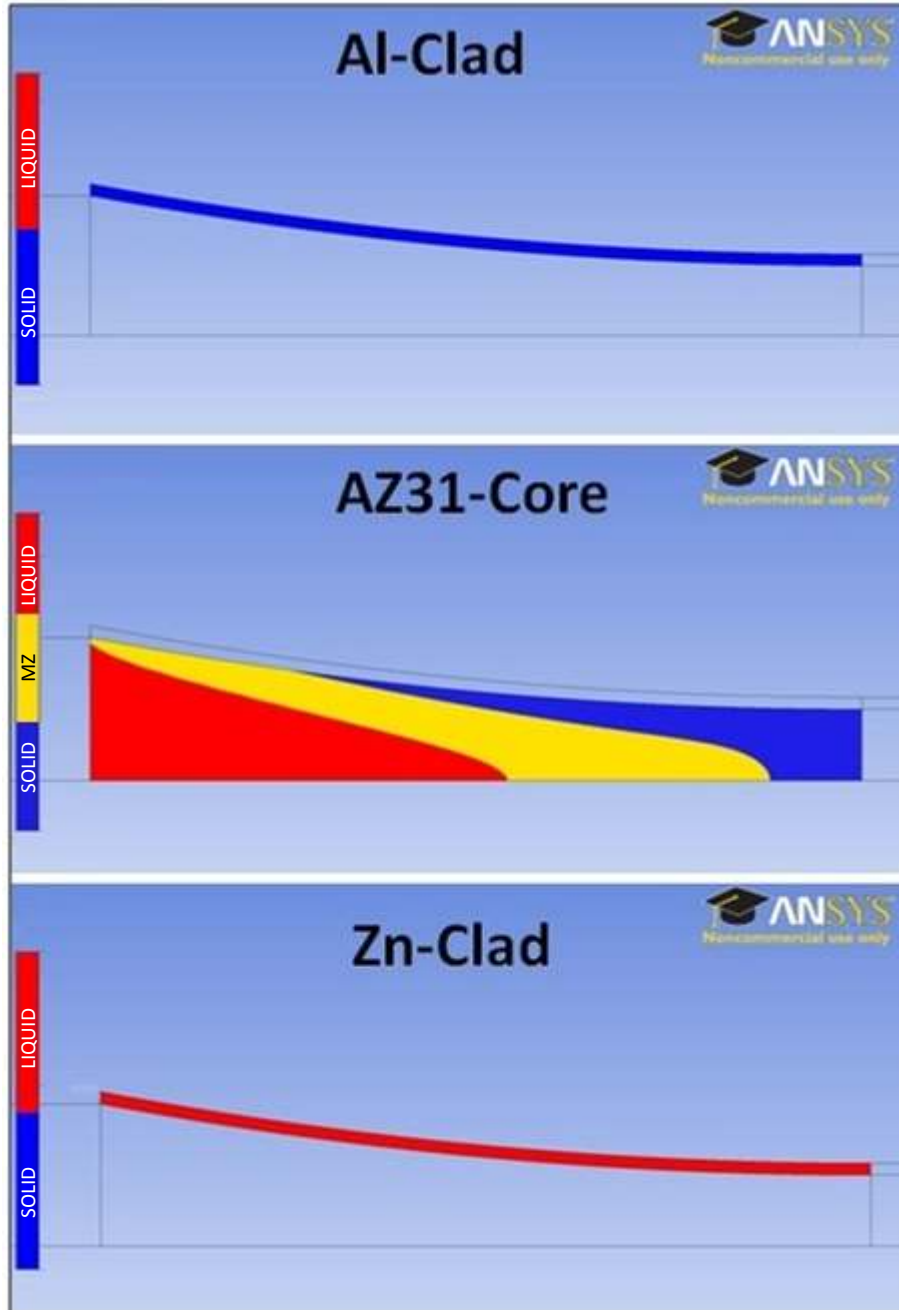


Figure 40 - Temperature Profile of Clad (AZ31) and Core (Al and Zn) at 3.0m/min casting speed

For the AZ31 core, it can be seen that as the speed increases, the sump depth and depth of the mushy zone increases. As the casting speed increases the position under the roll where the material becomes fully solid also shifts to positions closer to the TRC exit. When observing the aluminum clad layer, it can be seen that due to the high melting point of the material, the aluminum layer remains solid

throughout each of the simulation trials. In contrast, the results of the zinc clad layer show significant amounts of melting. The extend of the liquid phase in the clad layer increases as the cast speed increases until the final simulation, where only the liquid phase is present.

These results show that as the speed increases, the feasibility of cladding decreases. The simulation results presented in Figure 38-40 for the Zn-clad layer can be graphically represented in Figure 41. The temperature versus roll bite position of the aluminum simulations can be seen in Figure 42.

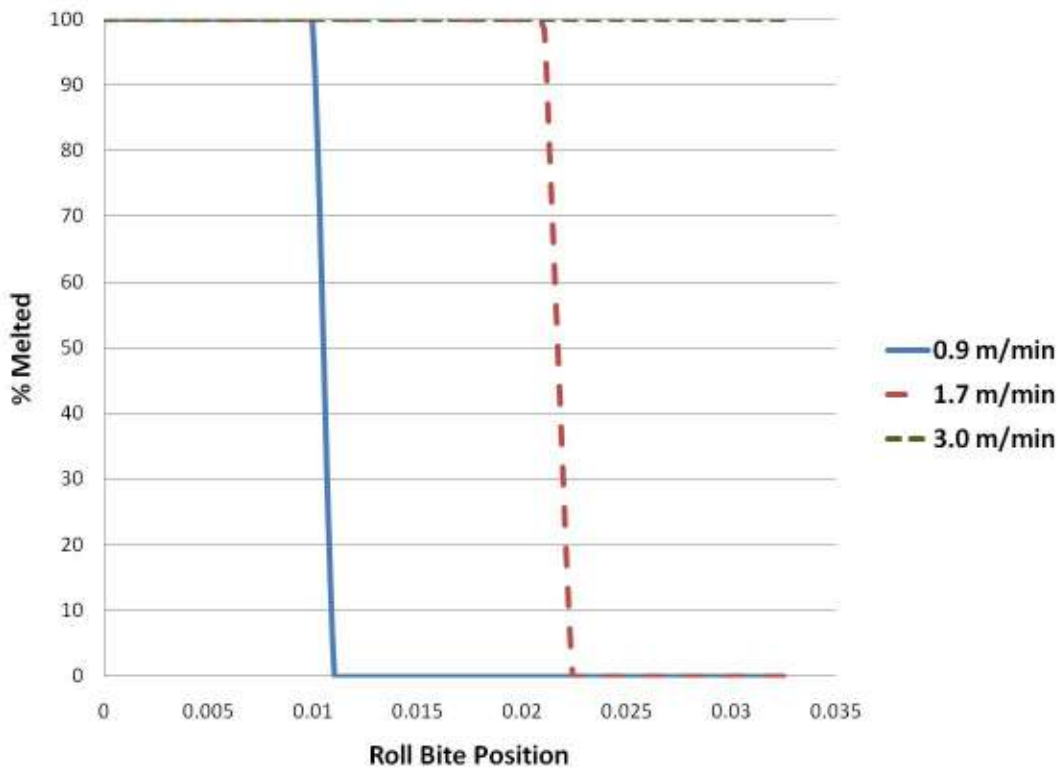


Figure 41 - Percent melting that occurs across the thickness of the zinc clad layer along the roll bite position

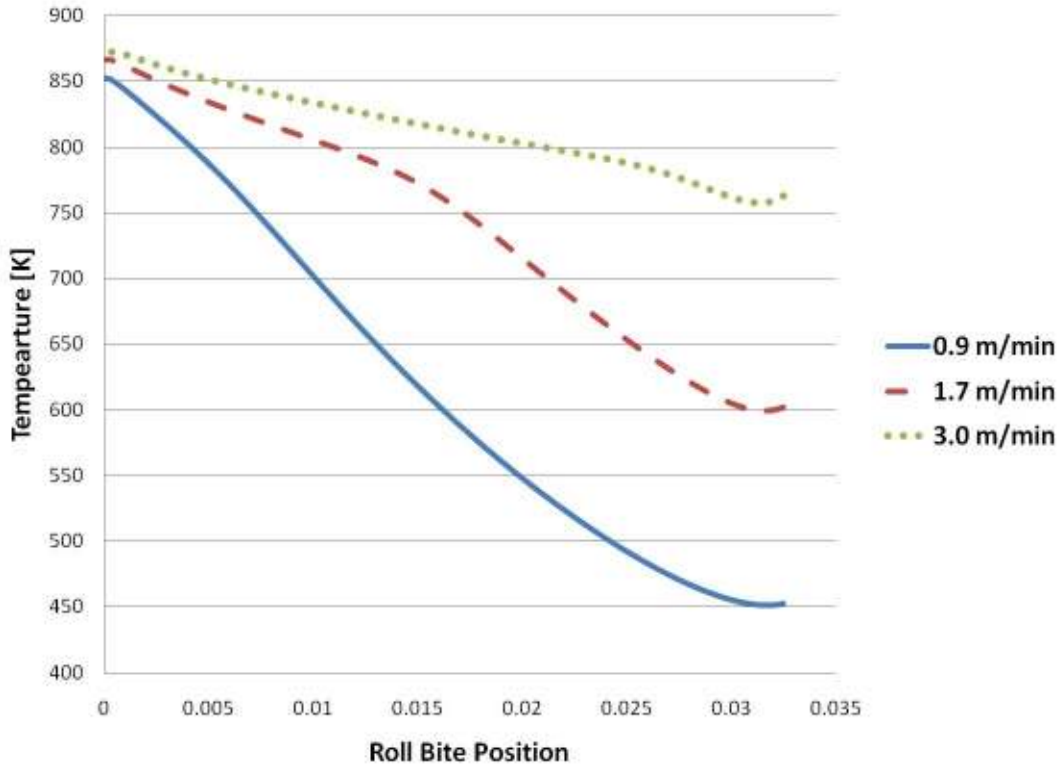


Figure 42 – Temperature of Al Clad – AZ31 Core Interface along the Roll Bite Position for various casting speeds

5.4.3 Clad Material Influences

Many simulations were conducted with the clad layer consisting of either zinc or aluminum properties. Under the same casting conditions, the resulting temperature profiles for each simulation seemed almost identical. This implied that the software package does not consider the various material properties inputted for each clad material to have a strong impact on the resulting temperature profile and that the main characteristic that contributes to the change in the temperature profile is the heat transfer coefficient. This is redundant, however, because the clad material directly influences the heat transfer coefficient. Though, for the purposes of these simulations, the heat transfer coefficient was held constant for various clad materials. This is important to consider for future simulations since the software, essentially, recognizes a change of material based on a change of heat transfer coefficient.

5.4.4 Process Window

In applying the results of all the simulations conducted, a process window was developed to clearly show the operational range and feasibility of the CANMET TRC process to produce clad materials. Various casting speeds and initial temperatures were simulated to predict the boundaries of the operational range. The clad layer thickness was held constant at 0.5 mm. A successful cast was defined as the cast material (core) entering the roll bite as a liquid and exiting as a complete solid throughout its thickness. Figure 43 shows the results of a successful and failed simulation.

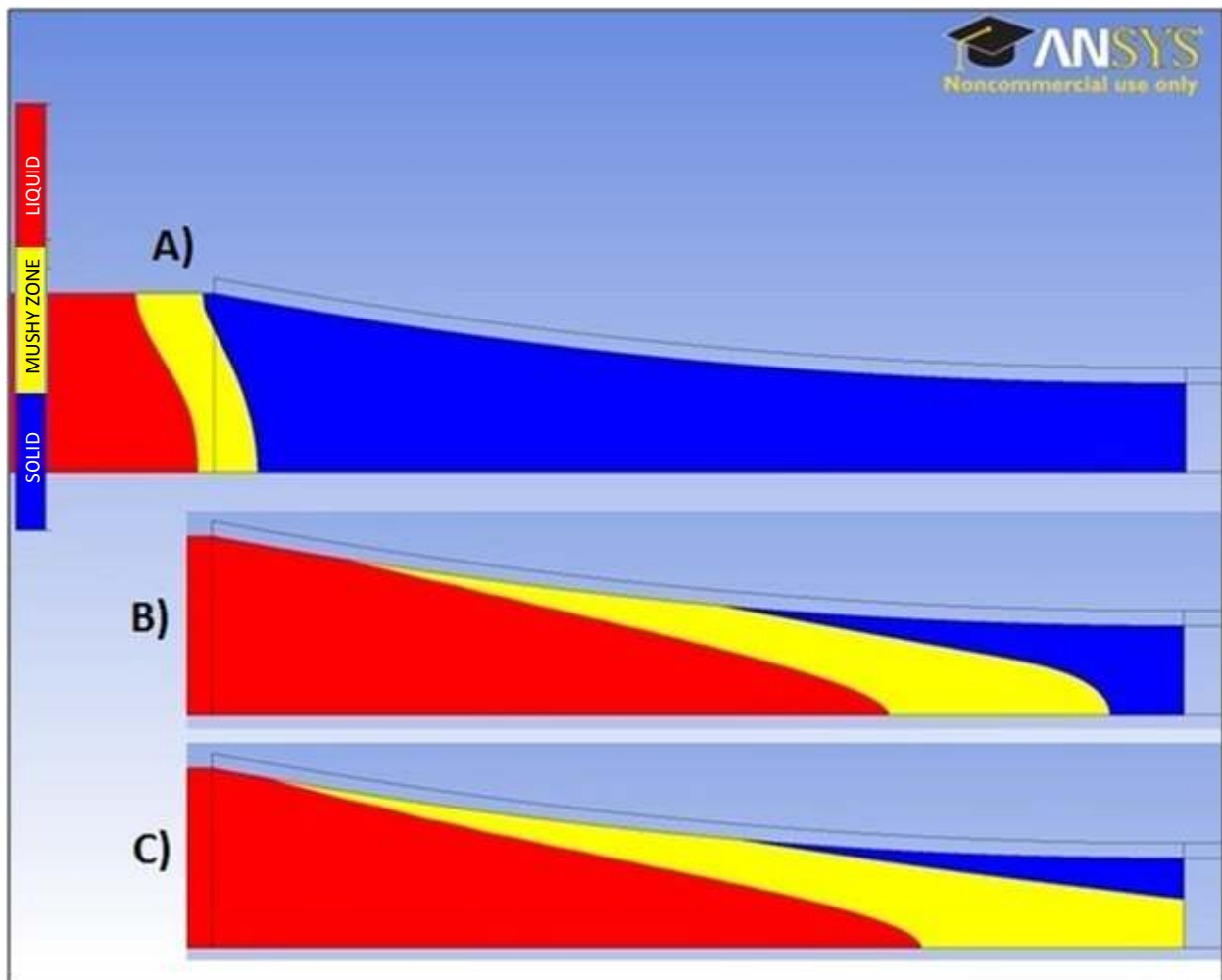


Figure 43 - Results from Simulations Conducted at Various Casting Parameters: A) A failed cast due to cooling before entry, B) A successful cast, C) A failed cast due to insufficient cooling

Figure 44 depicts the process window created from conducting 15 simulations. The process window was developed by altering casting temperatures and speeds. This process window is bound by the liquidus line and boiling point of the AZ31 alloy. Casting at a temperature below the liquidus would make the AZ31 in a mushy phase when exiting the nozzle and casting above the boiling point would imply the AZ31 is in a gaseous state; both of which are undesirable and unrealistic casting conditions. For practical purposes, casting would occur closer to the liquidus line. Simulations were only conducted at higher temperatures in order to predict the curves of the boundaries more accurately. The green squares represent the successful casts and the red squares represent the failed casts. The boundary between these two regions is drawn in purple and, along with the liquidus and boiling point line, is considered to be the region where twin roll casting can successfully be implemented for the AZ31 alloy. In addition to traditional twin roll casting, the feasibility of cladding is also depicted. The light blue line represents the boundary for successful casting of aluminum-clad AZ31 sheet. The cladding during the TRC process was considered a failure if too much melting within the clad layer occurred. Excessive melting was defined as melting throughout the entire thickness of the clad layer. According to the process window plot, a successful cast with aluminum cladding could occur anywhere from the boundary towards the left side of the plot. However, for practical purposes, the most optimal place to clad would be along the boundary so that little melting is present in order for a good metallic bond to form between the core and clad layer. As was shown in the sub-section 5.4.2, a zinc clad layer would endure too much melting to be considered successfully cast. The initial temperature of the cast would have to be below the liquidus line of the AZ31 alloy, which, in turn, would make the core cast unsuccessful. This is why a zinc boundary is not even present within the process window. Furthermore, using the temperature profiles generated from the 15 simulations of different casting conditions, boundaries of other clad materials can also be determined and labelled on the generated process window. For example, a hypothetical clad material with a melting point of 100° below that of the AZ31

alloy was simulated and is depicted by the yellow boundary. This shows the feasibility range of such a material. The process map generated from simulations coincides with the general shape of the early process maps developed by Watari et al. from the experimental trials they conducted, which was shown in Figure 4. Some differences, however, include the higher casting speeds they were able to achieve and the straight boundaries they established versus the curved boundaries predicted. One other very important difference is the lower limit of casting speed that is not present within their process map. Figure 45 shows the influence of clad thickness on the boundaries of the clad layers. Increasing the clad thickness allows for a greater operational range and shifts the boundaries to the right. However, based on the investigation conducted on clad thickness, the shift of these boundaries would be minimal unless the clad thickness was drastically increased.

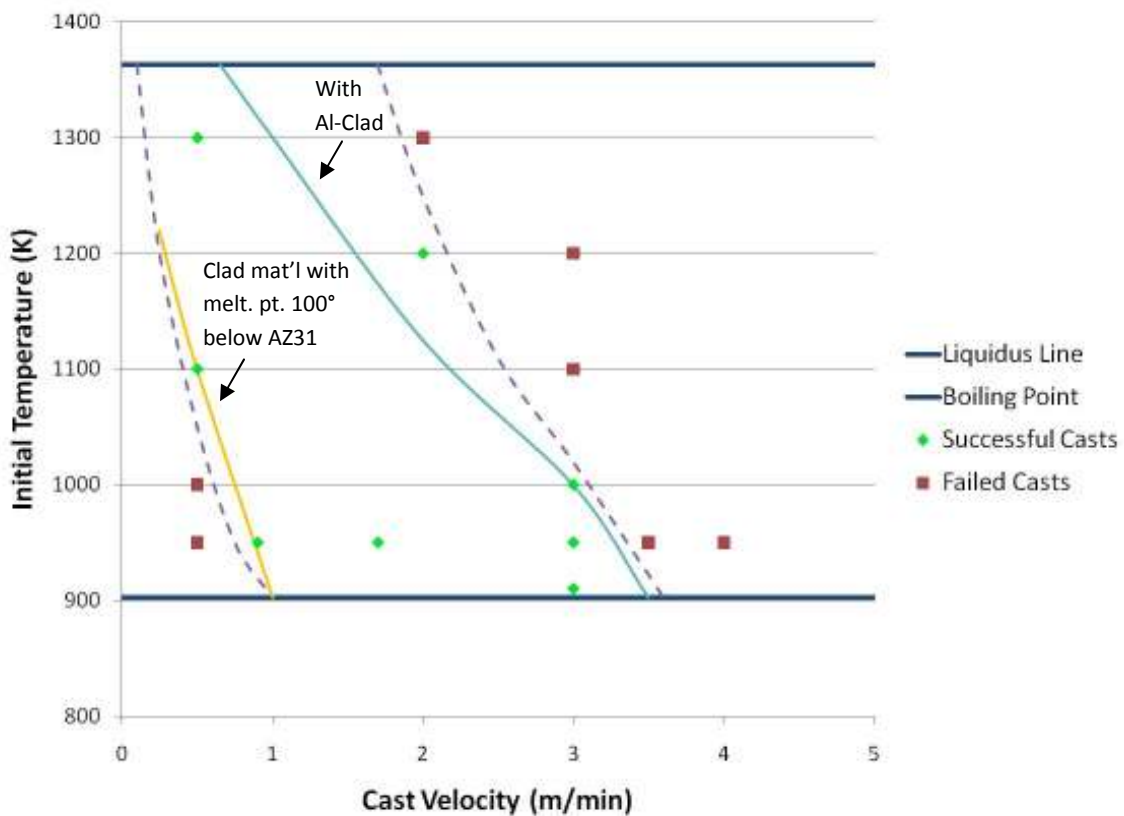


Figure 44 - TRC Process Window for the CANMET facility for a clad thickness of 0.5 mm

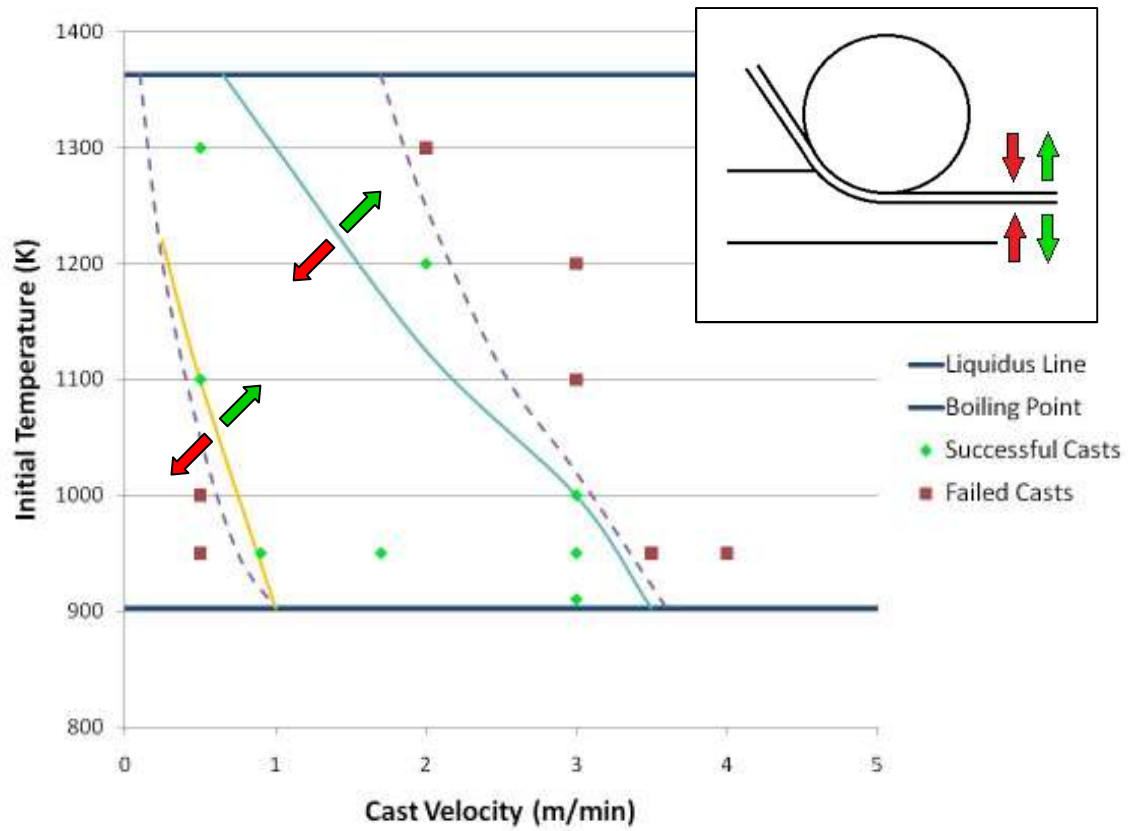


Figure 45 - TRC Process Window influences from clad thickness. Red arrows represent the direction clad boundaries move if clad thickness decreases. Green arrows represent the direction clad boundaries move if clad thickness increases.

Chapter 6: Summary, Conclusions, and Future Work

The scope of this project was to develop a validated mathematical model to simulate and assess the feasibility of cladding during the twin roll casting process for magnesium alloys. A 2D mathematical model of the twin roll casting process was created using the commercial CFD package ANSYS-CFX. Nine conventional twin roll casting experiments, under various operating conditions, were conducted for validation of this model. Experiments took place using the twin roll caster at POSTECH University. Each sample had their secondary dendrite arm spacing measured as a means of comparison with predictions made from the mathematical model. The measured secondary dendrite arm spacing values matched with the predicted values fairly accurately, in turn, validating the created model.

The samples were also observed for their microstructure. As expected, the samples showed similar microstructures with symmetry from the top to the bottom surfaces. The surfaces showed a very thin chill zone of fine grains followed by columnar dendrites. The centers showed an equiaxed dendritic region. The centerline SDAS did not change significantly with the change of casting conditions but trends were observed and were in good agreement with predicted values. The statistically insignificant difference in average SDAS values could have been attributed to an insignificant difference in casting parameter values. However, the casting parameters did influence the cast quality of the surface significantly. The small change in values did make a difference in surface defects observed within the samples.

Using the conventional model as a template, another model was created which, in addition to the twin roll casting process, introduced a cladding process. This model was simulated under various operating conditions to assess the feasibility of the cladding process. The feasibility was assessed through a thermodynamic standpoint without taking into account the actual material bonding

capabilities on a microstructure level. If clad layers could withstand the heat exchange from the AZ31 core to the rolls without incurring significant melting it was deemed successful.

One aspect that was explored was the impact of clad thickness on the temperature distribution. Since this is one of the controlled variables within the clad process of twin roll casting, the assessment of its impact on the feasibility needed to be investigated. It was found that the clad layer thickness did not affect the temperature profile of the cast to the point of impacting the success and/or failure of the simulation until the thickness was increased to an unrealistic size.

Another factor that was investigated was the influence of roll speed on the feasibility. Two clad materials were simulated for this study. This investigation showed results with trends in a predictable fashion. It was found that faster roll speeds would make the cladding process less feasible. This, along with the known boundaries of casting temperature, implicated that the feasibility of cladding during twin roll casting only occurred within a predefined window.

This window of feasibility was further investigated for conventional twin roll casting processes and TRC process with various clad materials. A process window was developed that showed the range of cast ability with respect to initial casting temperature and casting speed. From this window it can be seen that the use of zinc as a clad material is not feasible under any operating conditions. Furthermore, other materials with low melting points with respect to AZ31 would either be unsuccessful as clad materials or would only be feasible within a very small process range, thereby making casting very difficult. Materials with higher melting points such as aluminum prove to be more feasible as clad materials.

Though the boundaries of the window were developed based on simulations conducted at a constant heat transfer coefficient, the approach and boundary conditions of the model could be applied to any clad material. The developed process window is the most important conclusion drawn from this

research and offers twin roll casting operators a better idea of the bounds of casting and the potential limitations of cladding.

For future purposes, experimental work with cladding should be performed in order to integrate the material bonding properties within the feasibility window. This would provide a more realistic window of when cladding can be successful from a thermodynamic point of view and an actual material bonding perspective.

To further this research, the generated TRC process window should be validated through experimental means. Though model validation occurred for the conventional TRC model, the clad-TRC model is based off of a different caster with different roll materials and dimensions. This affects the heat transfer coefficient of the system greatly and, thus, influences the simulation results. Validating the TRC process window will aid in, both, legitimizing the boundary conditions of the model as well as the precision of the predictions made based on process parameters.

One recommendation would be to develop individual TRC process windows for various clad materials. Since the clad material affects the heat transfer coefficient of the system, the model should more accurately depict the heat transfer coefficient for each clad material. This would make the boundaries for successful casting more accurate.

Another aspect to consider is the ability to predict alloy microstructure based on simulation results. Microstructure prediction would include phase distribution within the sample and the quantity of each phase present, along with the amount of segregation. This would require a further detailed study on the influence of operational parameters on the microstructure. Having a better understanding of the resulting microstructure of a cast would help aid in the prediction of the quality of cast as well.

References

- [1] <http://www.magnet.ubc.ca/>
- [2] H. E. Friedrich, B. L. Mordike, *"Magnesium Technology"*, Springer, 2006.
- [3] F. Czerwinski, *"Magnesium Injection Molding"*, Springer US, 2008.
- [4] H. Watari, T. Haga, N. Koga, K. Davey, (2007) *"Feasibility study of twin roll casting process for magnesium alloys"*, Elsevier, *Journal of Materials Processing Technology* 192–193 (2007) 300–305
- [5] W. H. Hunt, *"Technical Cost Model for Magnesium Sheet Production"*, Technical Report, Aluminum Consultants Group Inc., 2005.
- [6] J. Zeng, R. Koitzsch, H. Pfeifer, B. Friedrich. (2008). Numerical simulation of the twin-roll casting process of magnesium alloy strip. *Journal of Materials Processing Technology*, 209, 2321-2328.
- [7] H. S. Di, Y. -L. Li, Z. -L. Ning, Z. Li, X. Liu, G. -D. Wang, *"New Processing Technology of Twin Roll Strip Casting of AZ31B Magnesium Strip"*, *Materials Science Forum*, 2005, Vols. 488-489, pp. 615-618.
- [8] D. Klein, *"Method of Manufacturing Composite Strips by Continuous Casting"*, United States Patent, US Patent #4224978, 1980.
- [9] T. Haga, K. Tkahashi, M. Ikawa, H. Watari, *"Twin Roll Casting of Aluminum Alloy Strips"*, *Journal of Materials Processing Technology*, 2004, Vols. 153-154, pp. 42-47.
- [10] R. Wechsler, *"The status of twin-roll casting technology"*, *Scandinavian Journal of Metallurgy*, 2003, Vol. 32, pp. 58-63.
- [11] D. Liang, C. B. Cowley, *"The Twin-Roll Strip Casting of Magnesium"*, CSIRO Manufacturing & Infrastructure Technology, 2004
- [12] S. S. Park, W. -J. Park, C. H. Kim, B. S. You, N. J. Kim, *"The Twin-Roll Casting of Magnesium Alloys"*, *Journal of the Minerals, Metals and Materials Society*, 2009, Vol. 61, No.8, pp. 14-18.
- [13] R. V. Allen, D. R. East, T. J. Johnson, W. E. Borbidge, D. Liang, *"Magnesium alloy sheet produced by twin roll casting"*, CSIRO Division of Manufacturing Science and Technology, The Minerals, Metals and Materials Society, 2001.

- [14] H. Watari, N. Koga, K. Davey, T. Haga, M. T. Alonso Ragado, "Warm Deep Drawing of Wrought Magnesium Alloy Sheets Produced by Semi-Solid Roll Strip-Casting Process", International Journal of Machine Tools & Manufacture, 2006, Vol. 46, pp. 1233-1237.
- [15] H. Watari, T. Haga, R. Paisern, N. Koga, K. Davey, "Mechanical Properties and Metallurgical Qualities of Magnesium Alloy Sheets Manufactured by Twin-Roll Casting", Key Engineering Materials, 2007, Vols. 345-346, pp. 165-168.
- [16] D.-Y. Ju, X.-D. Hu, (2006), "Effect of casting parameters and deformation on microstructure evolution of twin roll casting magnesium alloy AZ31", Transactions of Nonferrous Metals Society of China, pp 8874-s877
- [17] M. Numano, N. Mori, Y. Nakai, N. Kawabe, "Properties of AZ31 and AZ91 Sheets made by Twin Roll Casting", Materials Science Forum, Vols 539-543 (2007) pp 1650-1655
- [18] K.S. Papich, "Clad Metallurgical Products and Methods of Manufacture", United States Patent, US Patent #5476725, 1995.
- [19] A. K. Prasada Rao, K. H. Kim, J. H. Bae, G. T. Bae, D. G. Shin, N. J. Kim, "Twin-roll cast Al-clad Magnesium alloy", Materials Science Forum Vols. 618-619 (2009) pp 467-470
- [20] Hwang, J.D., Lin, H.J., Jang, S.C., Hwang, W.S., Hu, C.T., 1996. Relationship between flow characteristics and surface quality in inclined twin roll casting. ISIJ International 36, 690–699.
- [21] - P. Bradbury, "A Mathematical Model for the Twin Roll Casting Process", PhD Thesis, Department of Materials, University of Oxford, Oxford, UK, 1994.
- [22] - M. Yun, S. Lokyer, J. D. Hunt, "Twin Roll Casting of Aluminum Alloys", Materials Science and Engineering A, 2000, Vol. 280, pp. 116-123.
- [23] A. Hadadzadeh, "Mathematical Modelling of the Twin Roll Casting Process for AZ31 Magnesium Alloy", PhD Comprehensive Research Proposal, University of Waterloo, 2011
- [24] Tavares, R.P., Guthrie, R.I.L., 1998. Computational fluid dynamics applied to twin-roll casting. Canadian Metallurgical Quarterly 37, 241–250.

- [25] H. Zhao, P. Li, L. He, (2010) *"Coupled analysis of temperature and flow during twin-roll casting of magnesium alloy strip"*, Elsevier, Journal of Materials Processing Technology 211 (2011) 1197–1202
- [26] R. I. L. Guthrie, M. I. (2000). Measurements, Simulation, and Analyses of Instantaneous Heat Fluxes from Solidifying Steels to the Surfaces of Twin Roll Casters and of Aluminum to Plasma-Coated Metal Substrates. *Metallurgical and Materials Transactions B*, 31B, 1031-1047.
- [27] T. Haga, H. Watari, S. Kumai, (2006) *"High speed roll casting of Mg alloy strip by a vertical type twin roll caster"*, Journal of Achievements in Materials and Manufacturing Engineering, Vol. 15, Issue 1-2.
- [28] H. Watari, T. Haga, Y. Shibue, K. Davey, N. Koga, (2006) *"Twin roll casting of magnesium alloys with high aluminum contents"*, Journal of Achievements in Materials and Manufacturing Engineering, Vol. 18, Issue 1-2.
- [29] F. Incropera, D. Dewitt, T. Bergman, A. Lavine, Fundamentals of Heat and Mass Transfer 6th Ed., John Wiley & Sons, 2007
- [30] H. Rothery, (2007) *"THE CONSTITUTION OF THE MAGNESIUM-RICH ALLOYS IN THE SYSTEMS ALUMINIUM-MAGNESIUM, GALLIUM-MAGNESIUM, INDIUM-MAGNESIUM, AND THALLIUM-MAGNESIUM"*, J. Inst. Met., Vol. 63, 1938, p 201-226
- [31] M. S. Turhal, T. Savaskan, *"Relationships between secondary dendrite arm spacing and mechanical properties of Zn-40Al-Cu alloys"*, JOURNAL OF MATERIALS SCIENCE **38** (2003) 2639 – 2646
- [32] R. N. Grugel, *"Secondary and tertiary dendrite arm spacing relationships in directionally solidified Al-Si alloys"*, Journal of Material Science 28 (1993) 677-683
- [33] Hunt, J. D., 1984. Steady State Columnar and Equiaxed Growth of Dendrites and Eutectic. Materials Science and Engineering. Vol. 65, pp 75-83.
- [34] Kurz, W., Bezencon, C., Gaumann, M., 2001. Columnar to equiaxed transition in solidification processing. Science and Technology of Advanced Materials. Vol. 2, pp 185-191.
- [35] M. Yun, S. Loky, J. D. Hunt, *"Twin Roll Casting of Aluminum Alloys"*, Materials Science and Engineering A, 2000, Vol. 280, pp. 116-123.
- [36] M. A. Wells, Associate Dean of Outreach, University of Waterloo, Personal Communications.

- [37] A. Basernia, Post-Doctoral, University of Waterloo, Personal Communications.
- [38] S. Kou, Welding Metallurgy 2nd Ed., John Wiley & Sons, 2003
- [39] D. A. Porter, K. E. Easterling, M. Sherif, Phase Transformation in Metals and Alloys 3rd Ed., CRC Press, 2009.
- [40] S. R. Agnew, (2004) "*Wrought Magnesium: A 21st Century Outlook*", Dept. of Materials Science & Engineering, University of Virginia.
- [41] Z. Bian, I. Bayandorian, H. W. Zhang and Z. Fan, "*Twin roll casting and melt-conditioned twin roll casting of magnesium alloys*", Brunel Center for Advanced Solidification Technology, Brunel University.
- [42] G. D. Stuble, Computational Fluid Dynamics for Fluid Engineering Design-ANSYS CFX Student User Manual Version 11. Dept. of Mechanical Engineering, University of Waterloo, 2008.
- [43] P. S. Cooper, P. Fisher, "*Grain Refining of Strip Cast Aluminum*", 123rd TMS Annual Meetings and Exhibition, London & Scandinavian Metallurgical Co Limited, U.K., 1994
- [44] B. Wang, J. Y. Zhang, J. F. Fan, S. L. Zhao, S. B. Ren, K. C. Chou, "*Modelling of Melt Flow and Solidification in the Twin-Roll Casting Process*", Process Metallurgy (2008)
- [45] M. K. Kulekci, "*Magnesium and Its Alloys Applications in Automotive Industry*", International Journal of Advanced Manufacturing Technology, 2008, Vol. 39, pp. 851-865
- [46] H. Geduld, Zinc Plating, ASM International, Finishing Publications, 1988.
- [47] D. R. Askeland, P. P. Phule, The Science and Engineering of Materials 5th Ed., Thomson, 2006
- [48] Y. Nakaura, K. Otori, "*Properties of AZ31 Magnesium Alloy Sheet Produced by Twin Roll casting*", Materials Science Forum, 2005, Vols. 488-489, pp. 419-426.

Appendix A - CFX Model Setup

This appendix details the setup of the boundary conditions and material properties of the mathematical twin roll casting process model. The first few figures show the material setup settings for the inputted materials AZ31 and Zinc. The reference temperatures and specific heats need to be accurate in order for ANSYS to calculate appropriate latent heat values for these materials.

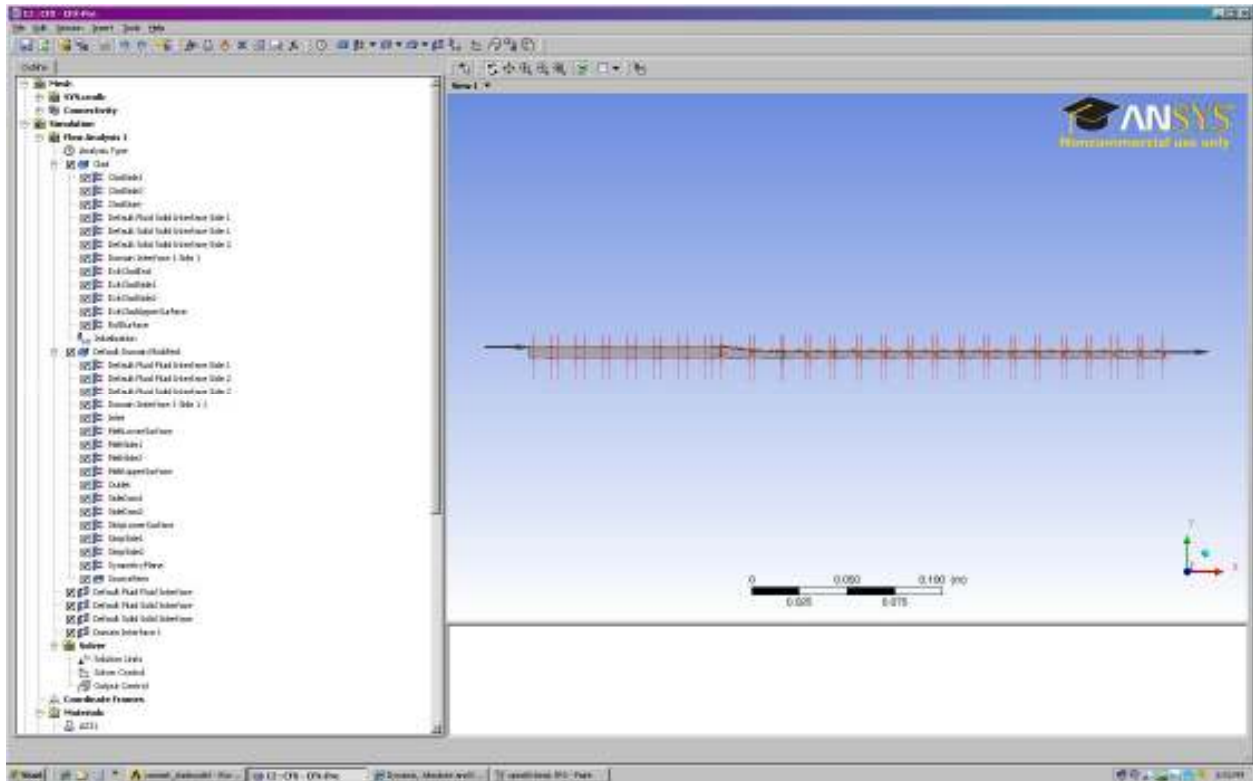


Figure 46 - CFX-Pre Model Setup Screen

Next, the domains have to be set as either solid or fluid and also need to be assigned materials. Refer to figures for further details on other settings. A boundary condition is required for all surfaces of the model. The majority of surfaces consist of symmetry boundary conditions. The only exceptions are the inlet, outlet, and top surfaces. The top surface of region 1 and 3 are modelled as adiabatic walls. Refer to appropriate figures for details on setup. The roll surface is the only face within the geometry that is modelled as a wall with heat transfer. Details on roll surface setup are based on the twin roll caster (roll diameter, speed, HTC, etc.).

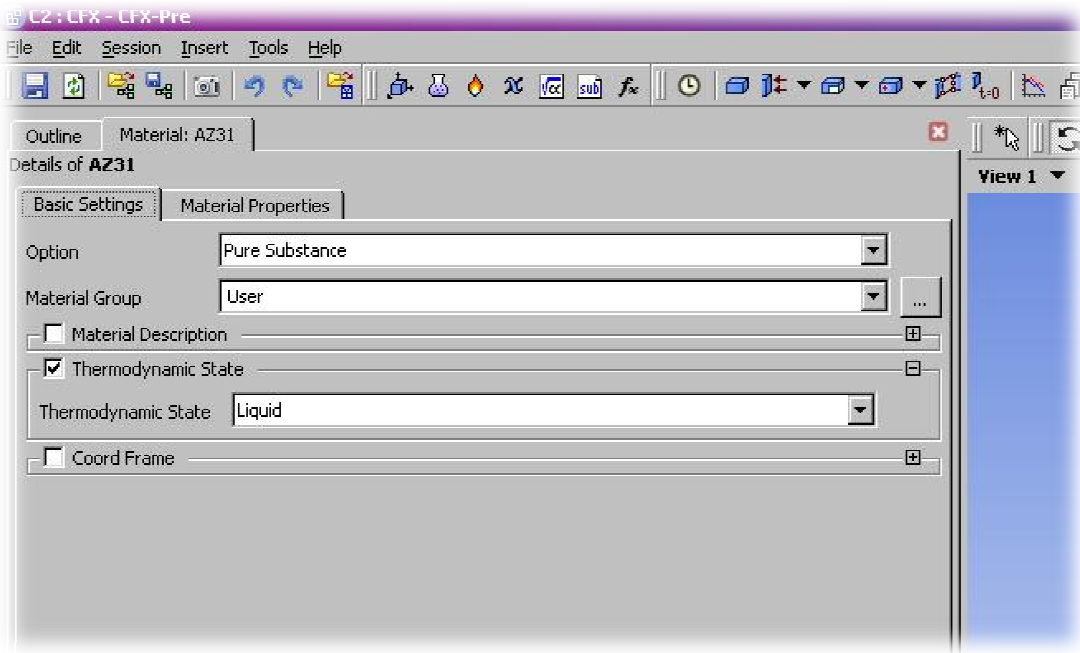


Figure 47 - AZ31 Material Properties Setup

The source term is added in order to accurately model the fluid flow of AZ31 during the transition from a liquid to solid phase. The equations are derived from the solid fraction within the AZ31 core and refer to expressions inputted by the user. All data tables used for the generated expressions were obtained from literature. Refer to the appropriate figures for details on data tables and equation expressions.

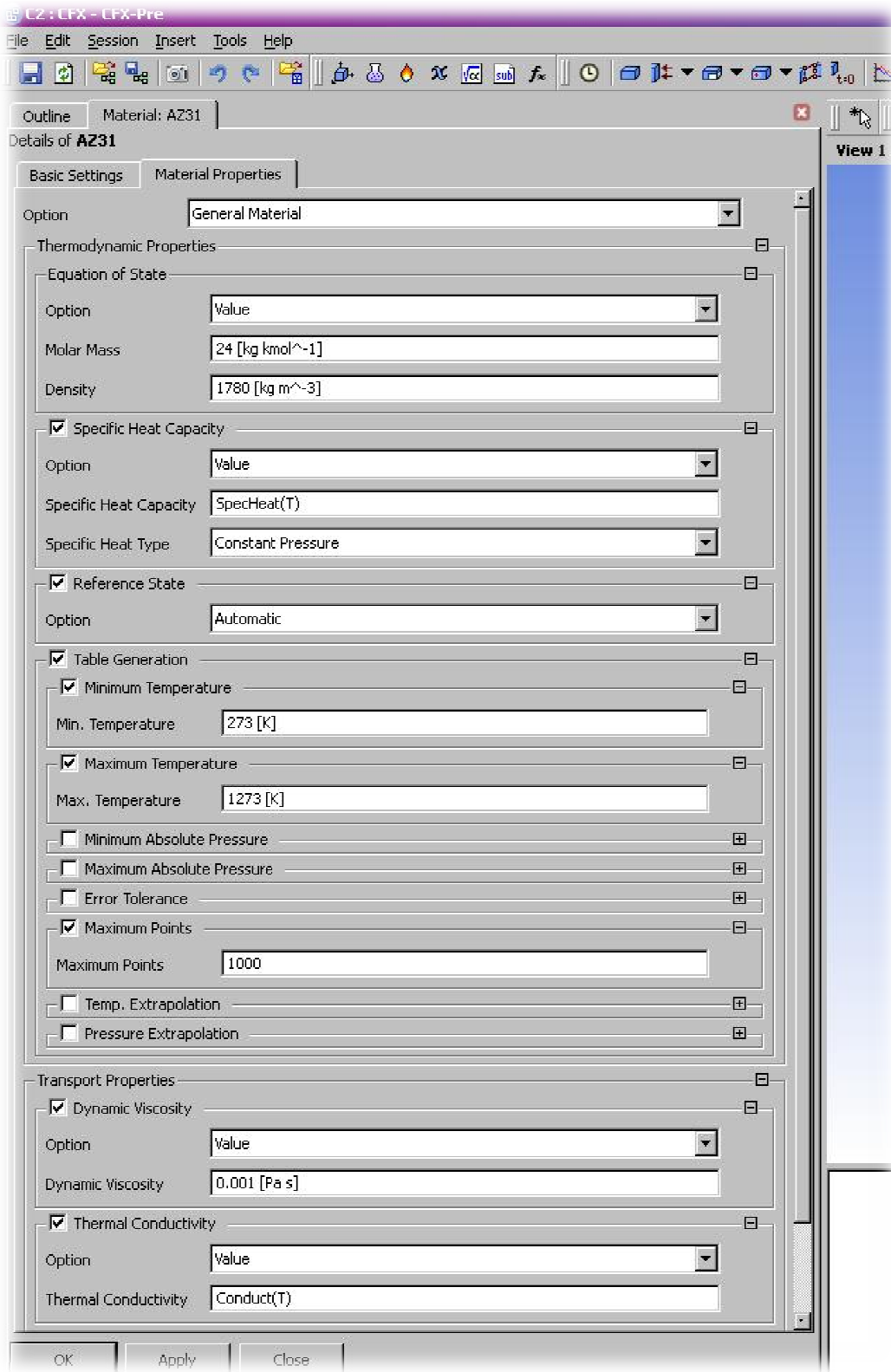


Figure 48 - AZ31 Material Properties Setup cont'd

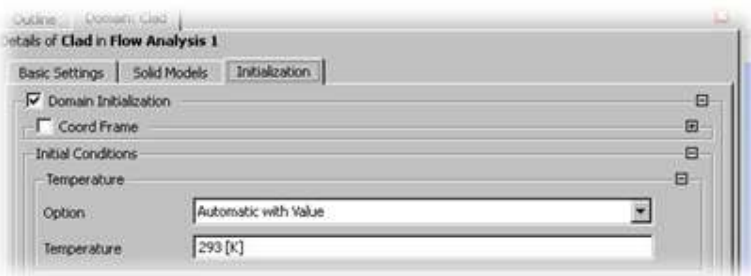
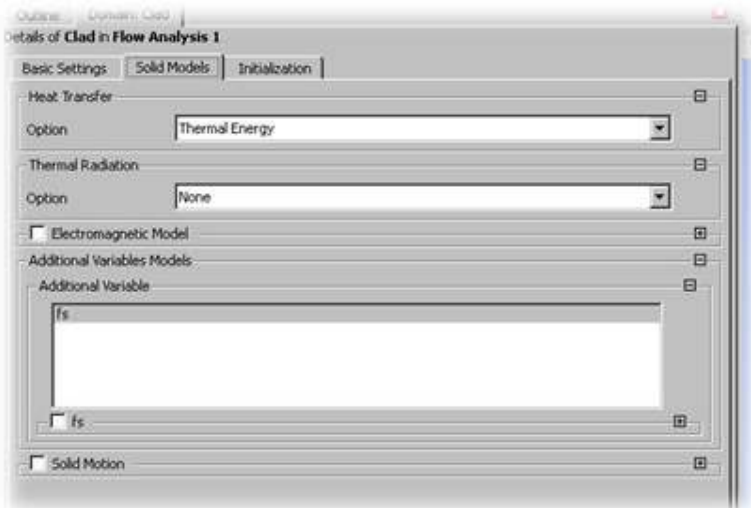
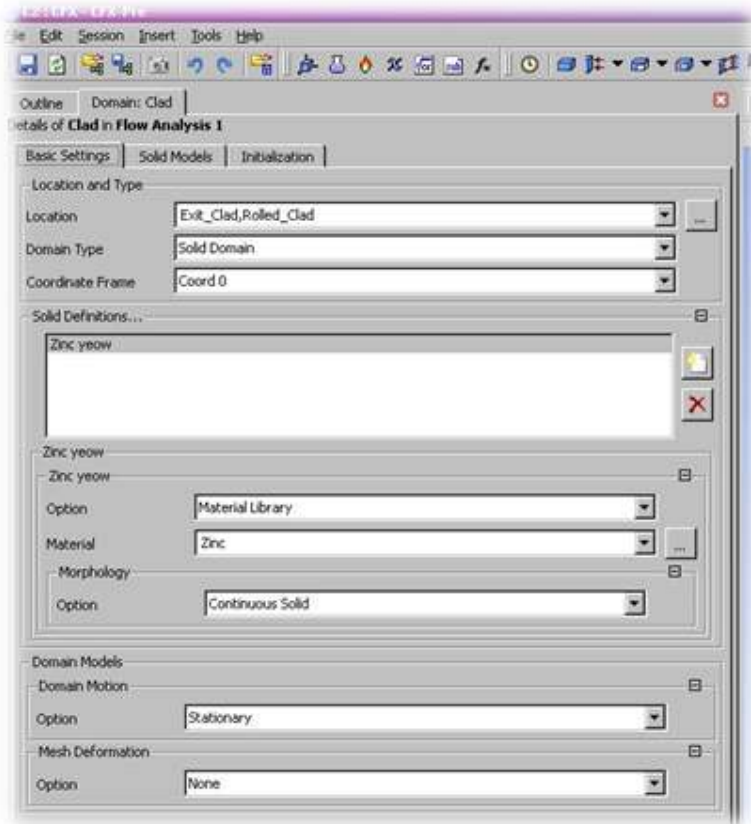


Figure 49 - Clad Domain Setup

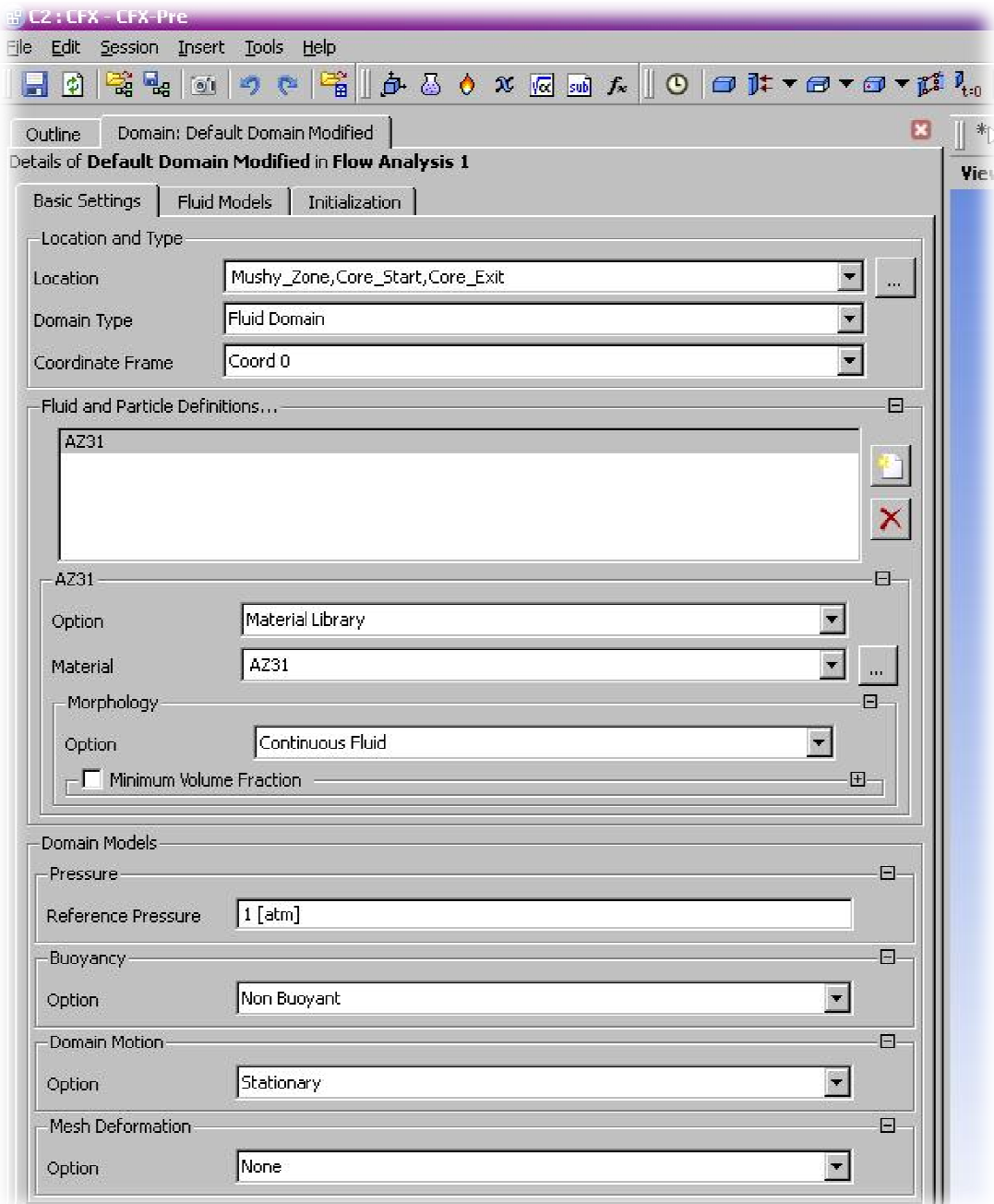


Figure 50 - Core Domain Setup

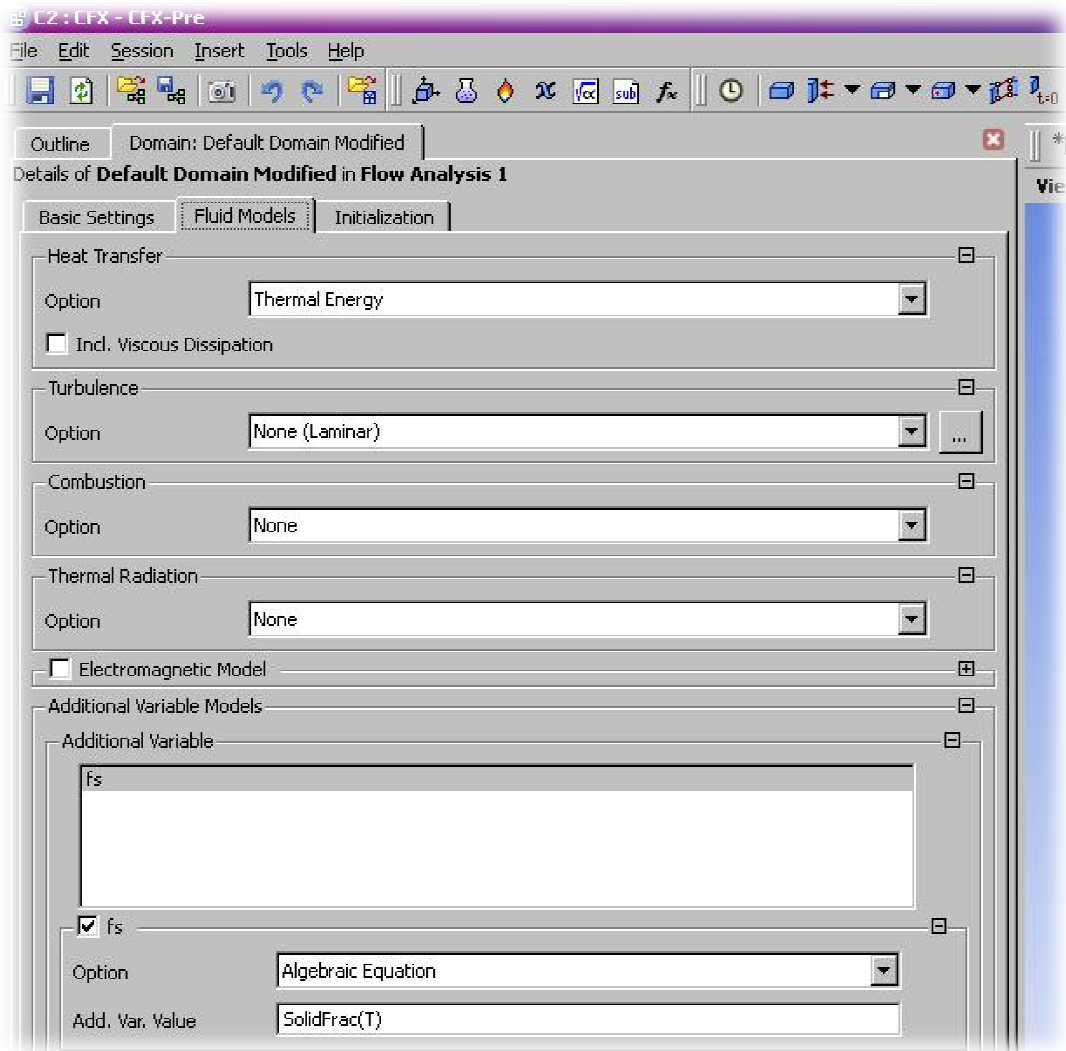


Figure 51 - Core Domain Setup cont'd

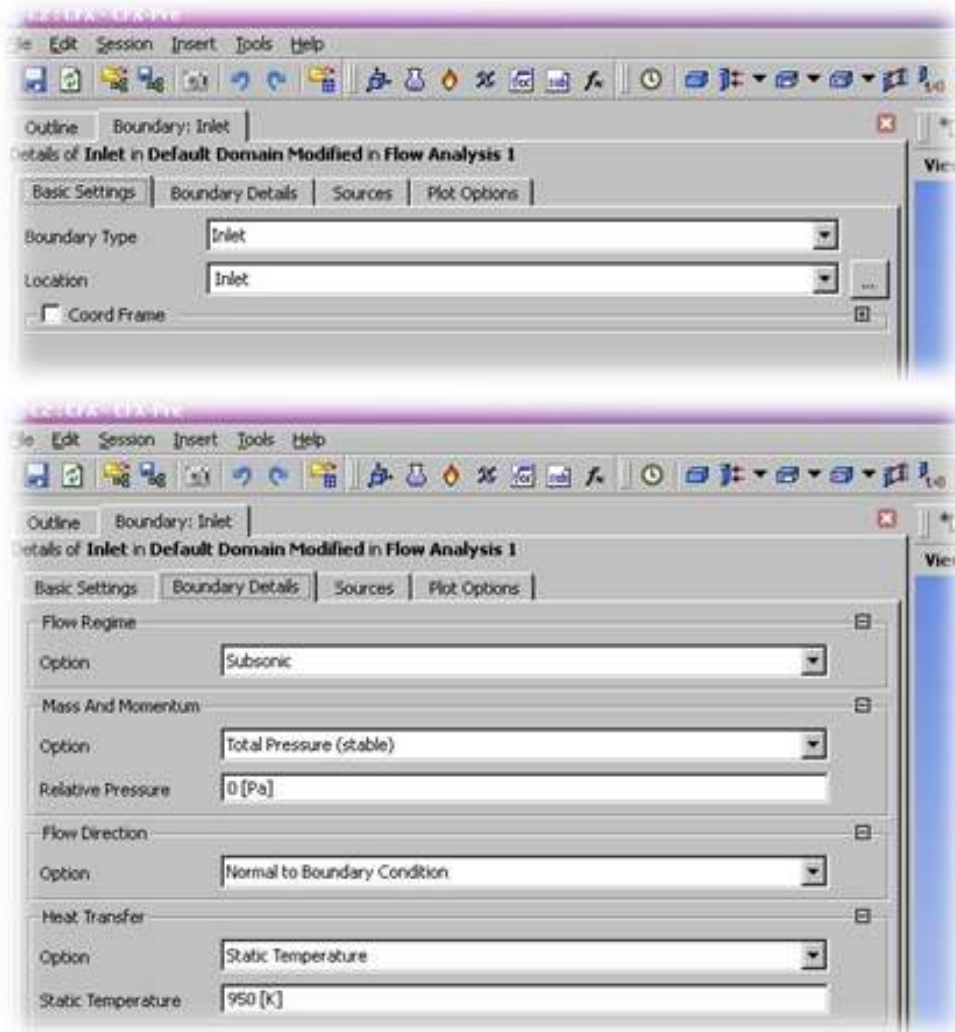


Figure 52 - Inlet Setup

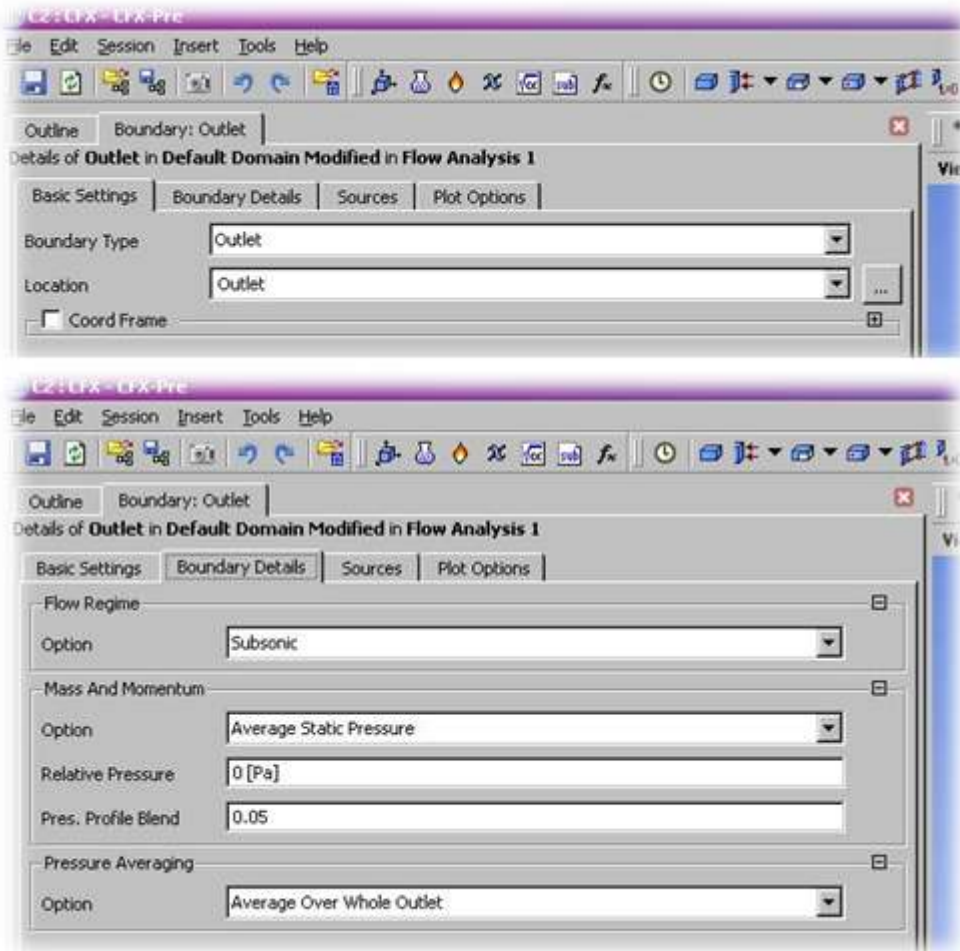


Figure 53 - Outlet Setup

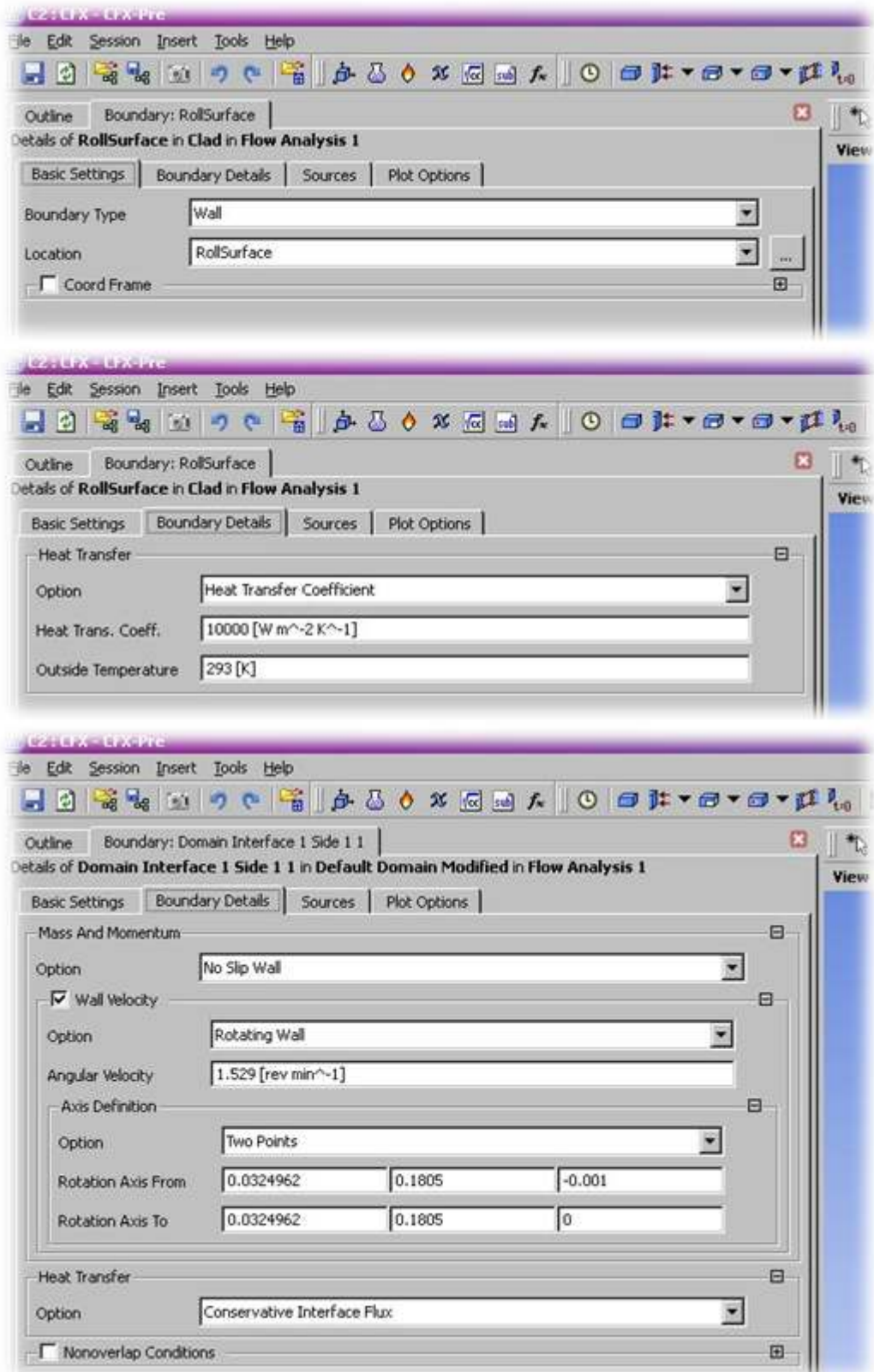


Figure 54 - Roll Surface Boundary Condition Setup. Rotating wall is setup at domain interface for the clad model

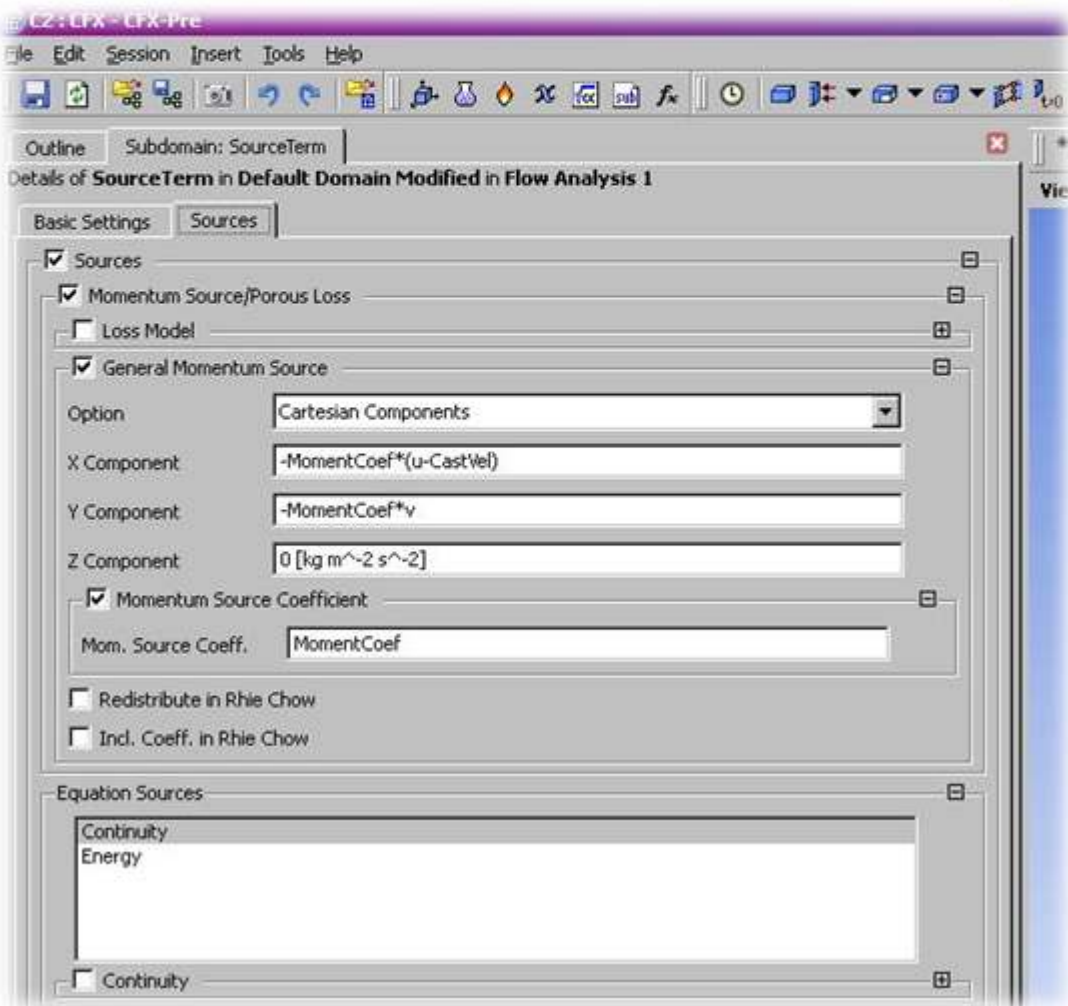
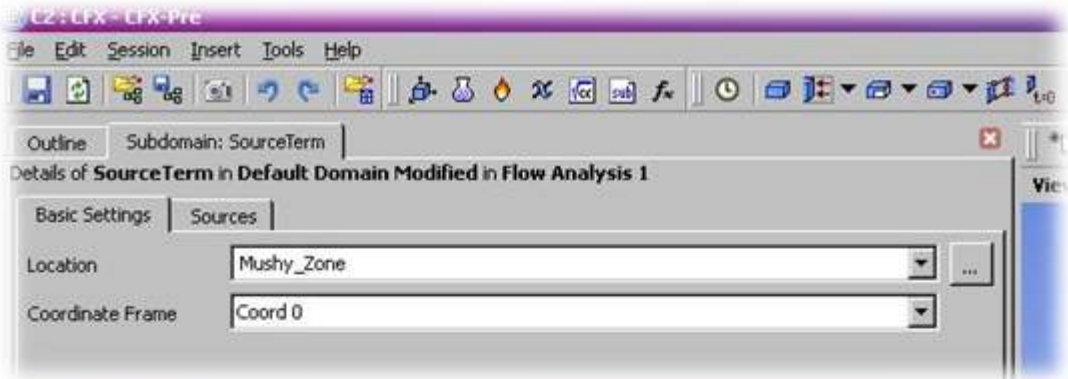


Figure 55 - Source Term setup for Fluid Flow Correction

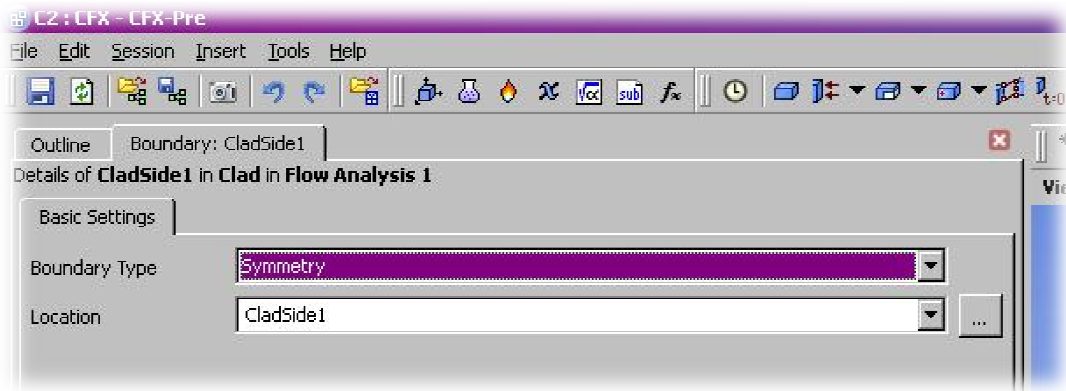


Figure 56 - Symmetry Plane Boundary Condition

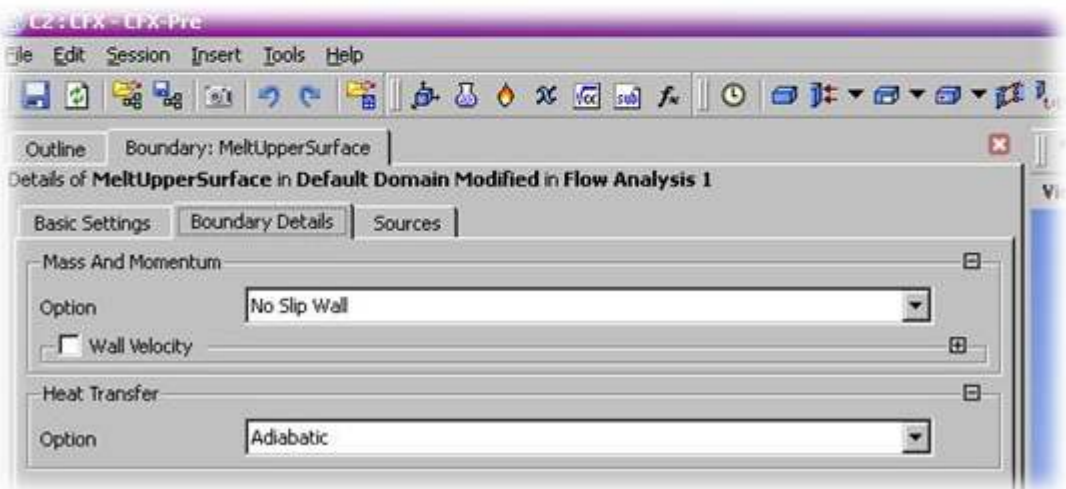
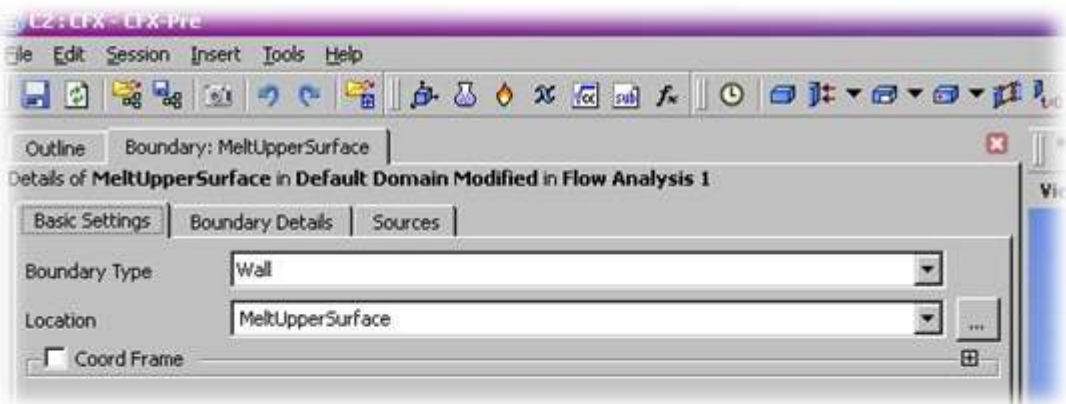


Figure 57 - Adiabatic Wall Setup

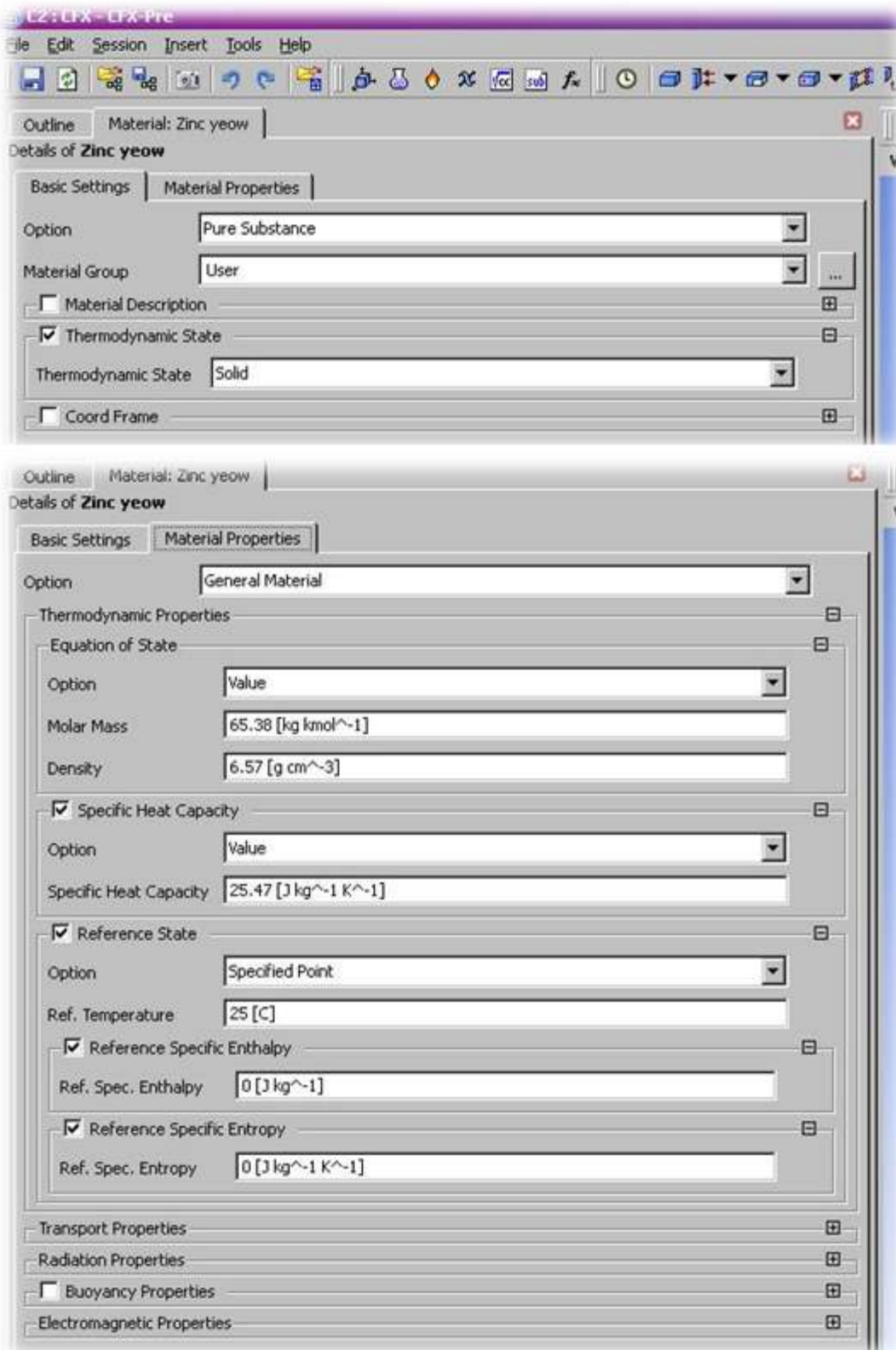


Figure 58 - Zinc Material Properties Setup

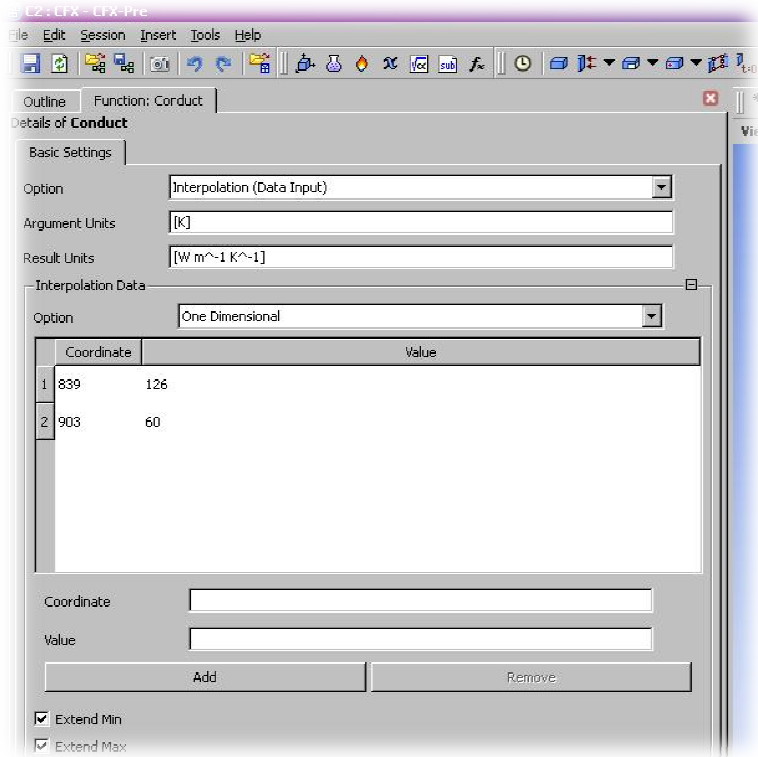


Figure 59 - Conductivity Equation Setup

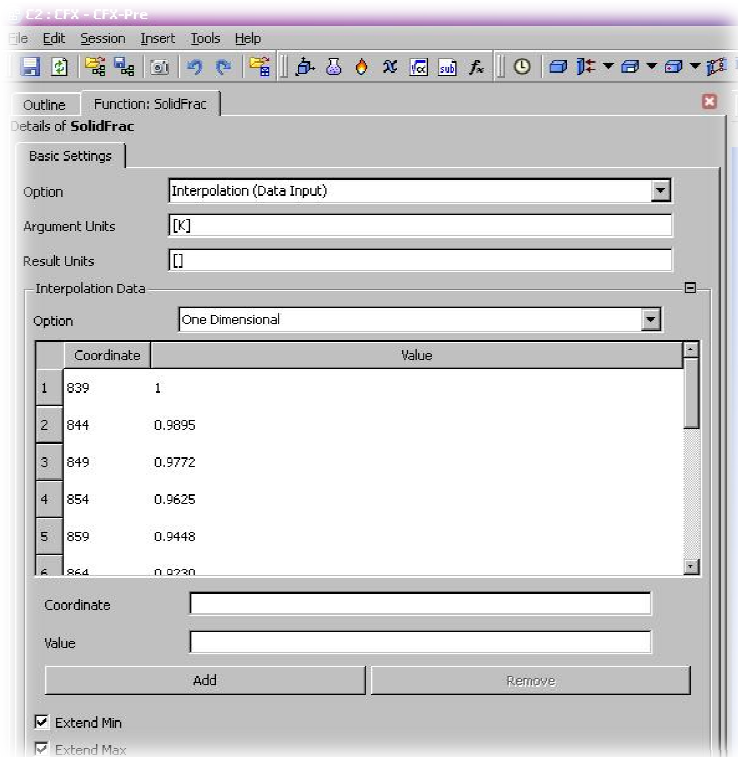


Figure 60 - Solid Fraction Equation Setup

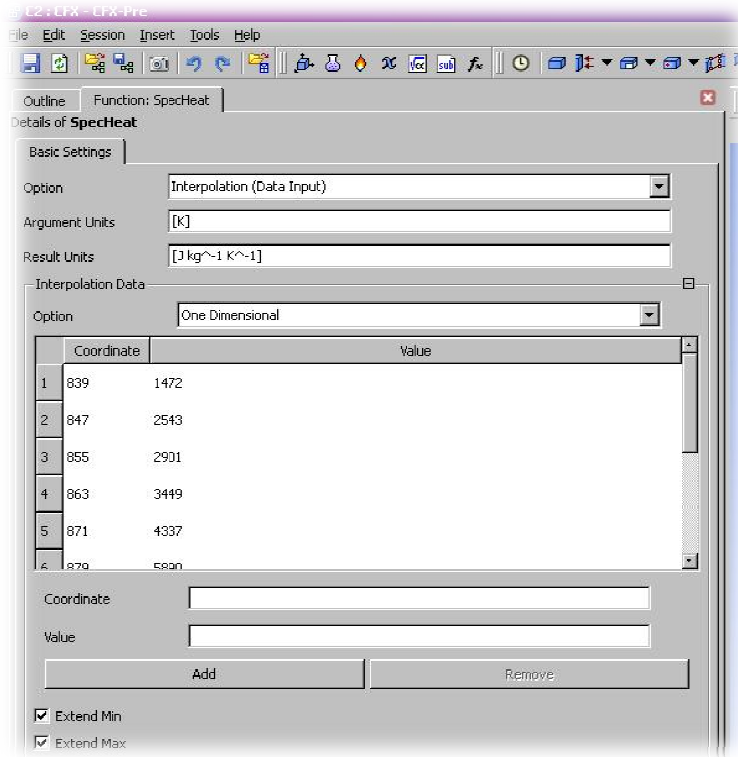


Figure 61 - Specific Heat Capacity Equation Setup

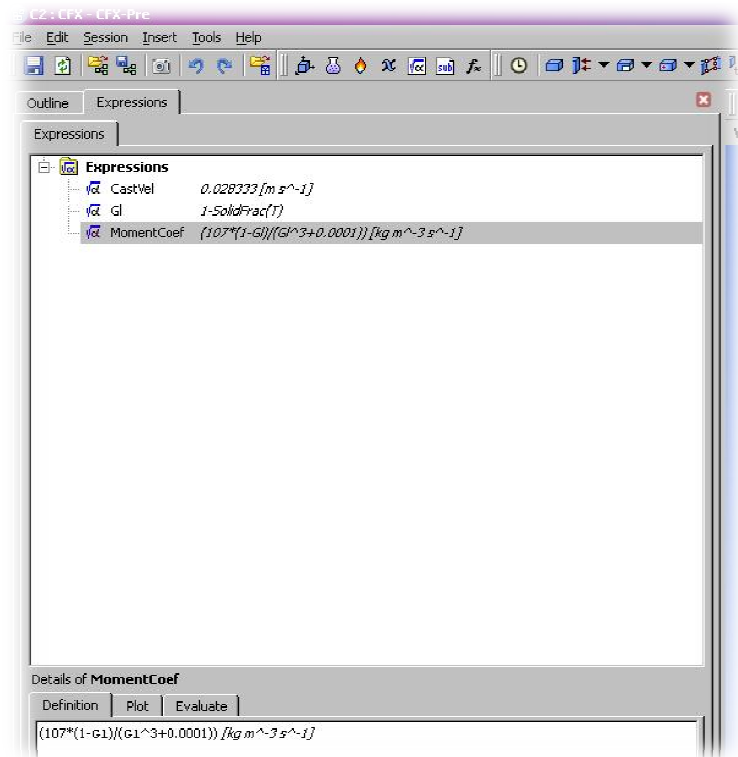


Figure 62 - Expression Setup

Appendix B - TRC Procedure

This appendix describes the procedure of the twin roll casting experiments that took place at POSTECH University.

Procedure Details:

A number of steps are required to operate the twin roll caster. This section outlines the step-by-step procedure from the beginning of the casting process to its completion for all the experiments conducted in this study. The first step is to ensure that all appropriate safety equipment is worn and that the caster is operated under nominal environmental conditions. Though the liquid metal solidifies at the rolls and exits as a solid, it is still extremely hot. Therefore, appropriate protection for the hands and body is required to ensure protection from burning. Goggles are also required due to the fact that sparks may occur if the metal catches on fire due to oxidation. The humidity within the lab is also very important to maintain. Since the material that is being cast is a magnesium alloy, oxidation is a constant problem so a dry environment is desired. To limit the oxidation that occurs, the humidity of the room is monitored.

With regards to set up of the equipment, the first step is to set the tundish temperature at the control panel to the desired casting temperature. Next, the roll gap needs to be adjusted to the desired exit thickness. A button is in place on the control panel to raise or lower the top roll and the adjusted roll gap is then measured with a vernier caliper. After these casting conditions are set, the power for the crucible should be turned on to ramp up the temperature. The crucible temperature should reach approximately 800°C for AZ31. While the crucible temperature is being ramped up, the metal AZ31 bars can be placed inside the crucible to be melted. Due to the limited space within the crucible, all the bars cannot be dropped in at the same time and need to be fed in two or three at a time. At this point it is very important to ensure that the CO₂ and SF₆ gas mixture is always on and directed to the molten metal in the crucible to prevent oxidation at the surface. Figure 64 shows the difference between a melt pool

with poor shielding from the gas mixture where oxidation occurs and one where proper shielding prevents oxide from forming.

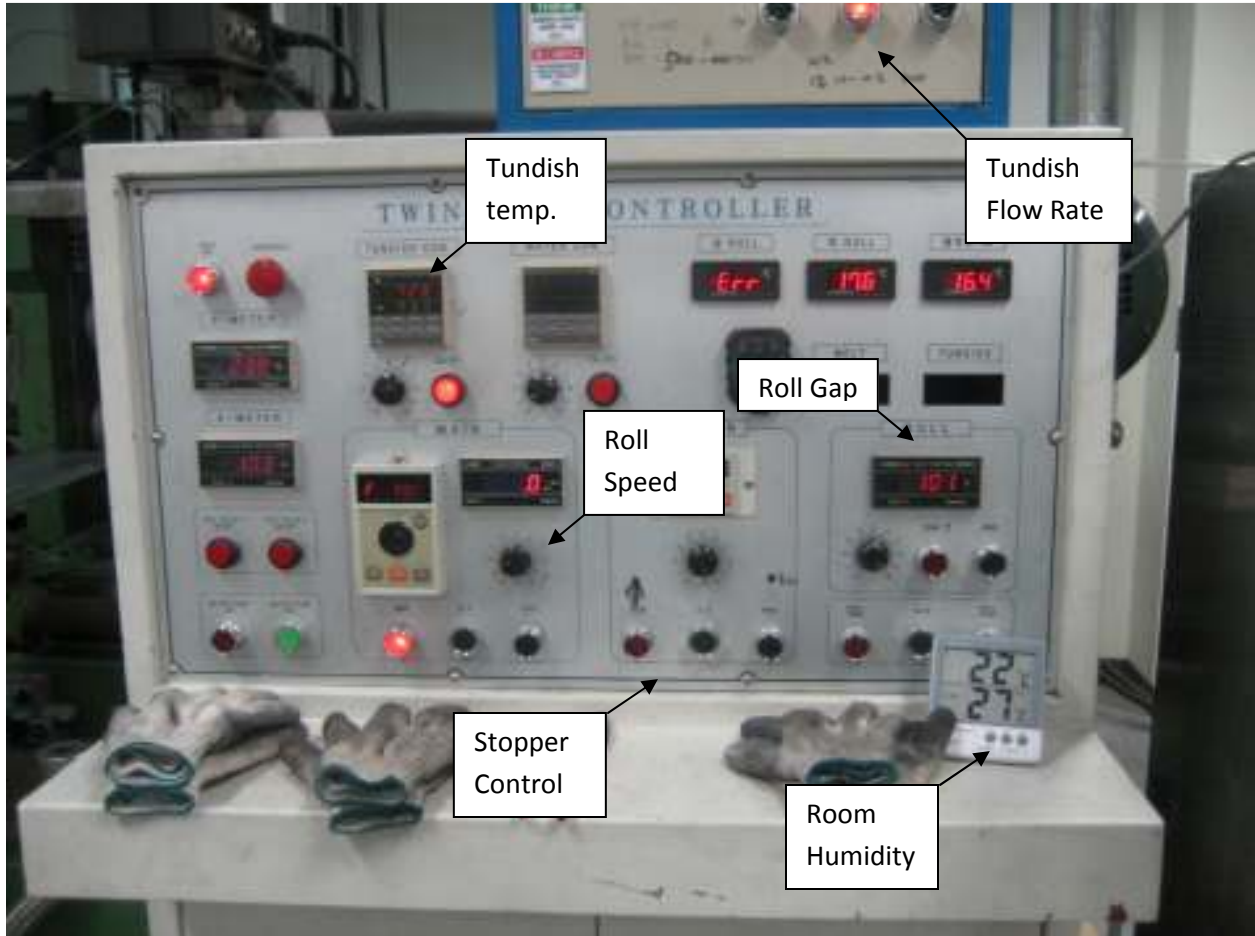


Figure 63 - TRC controls

When the desired tundish and crucible temperature are met and all the metal is melted, the roll speed can be ramped up to the desired speed. At this point, the crucible power can be turned off and the water pump for the rolls can be turned on. The water pump controls the water flow through the rolls to adequately cool them during the casting process. At this stage, the crucible needs to drop to approximately 20°C above the desired tundish temperature and then the molten metal can be released into the tundish. This is done by releasing the stopper in the crucible. When the stopper rises to the top, it allows for all the molten metal to flow into the tundish beneath.



Figure 64 - Difference of Melt Pool with (Right) and without (Left) protective gas shielding

The next step is to control the flow to allow the tundish to tilt and pour the liquid metal towards the rolls. As the metal flows through the nozzle and towards the rolls it is cooled and solidifies. The cast is pushed out of the rolls and needs to be guided towards the track in front of the rolls as it comes out. Any unwanted pieces of cast that stick to the roll should be knocked away in order to prevent interference between the pieces stuck on and the new cast. Towards the end of the cast the flow rate needs to be increased to help push out all of the material out of the tundish and towards the roll. This step is very important because if the flow rate remains the same then the ends of the cast come out very poorly since the material flow rate does not fill the entire nozzle and material tends to not flow through the rolls properly and, instead, stick to the rolls a lot more.



Figure 65 - Guiding the cast out of the rolls while removing any debris attached to the rolls

After the cast is completed, the equipment is powered down and the tundish is removed from the furnace and placed in a sand box. Sand is poured on any remaining material to prevent burning due to oxidation. This may occur at left over material on the rolls or at the edge of the nozzle as well. After this is completed, the excess material needs to be scraped off and the equipment needs to be cleaned off.



Figure 66 - Removing the tundish from the furnace and submerging it in sand

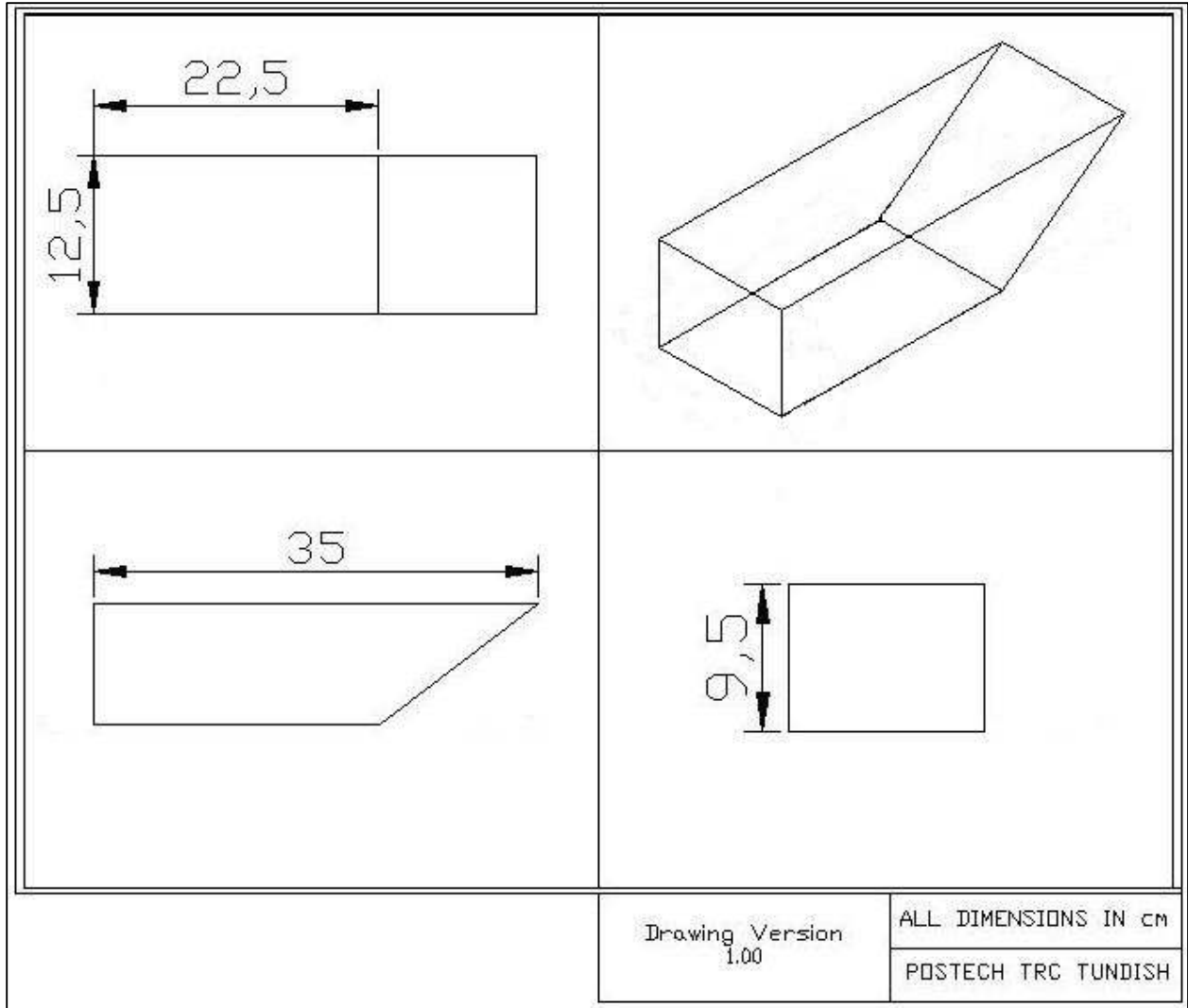


Figure 67 - Tundish dimensions

Appendix C - Metallography

This appendix refers to details regarding the preparation of the samples used for the experimental portion of the project.

Optical Microscope Details:

The mounted samples were attached to a slide using Plasticine. The samples were then hard pressed to ensure that they were completely flat when placed under the microscope. This was important because if the samples were viewed on an angle, focussing the image would be a big problem since the distance from one side of the image to the lens would be different than the other side. A software package called ImagePro 6.3 was used to acquire the optical microscope images. The image contrast and brightness was altered using this software in order to improve the clarity of the image as much as possible. This software was also used in measuring the secondary dendrite arm spacing within each sample. The 'measure' tool in ImagePro 6.3 was pre-calibrated for all magnifications of the optical microscope and simply needed to be set to the correct magnification in order to make measurements and apply scales on to images. All samples underwent an acquisition of overall thickness images and central region images. The borders between the surface microstructure and center microstructure were also observed.

The following figures are optical micrographs of the various samples across their thicknesses. The top and bottom parts of the images represent the top and bottom surfaces of the sample, respectively.

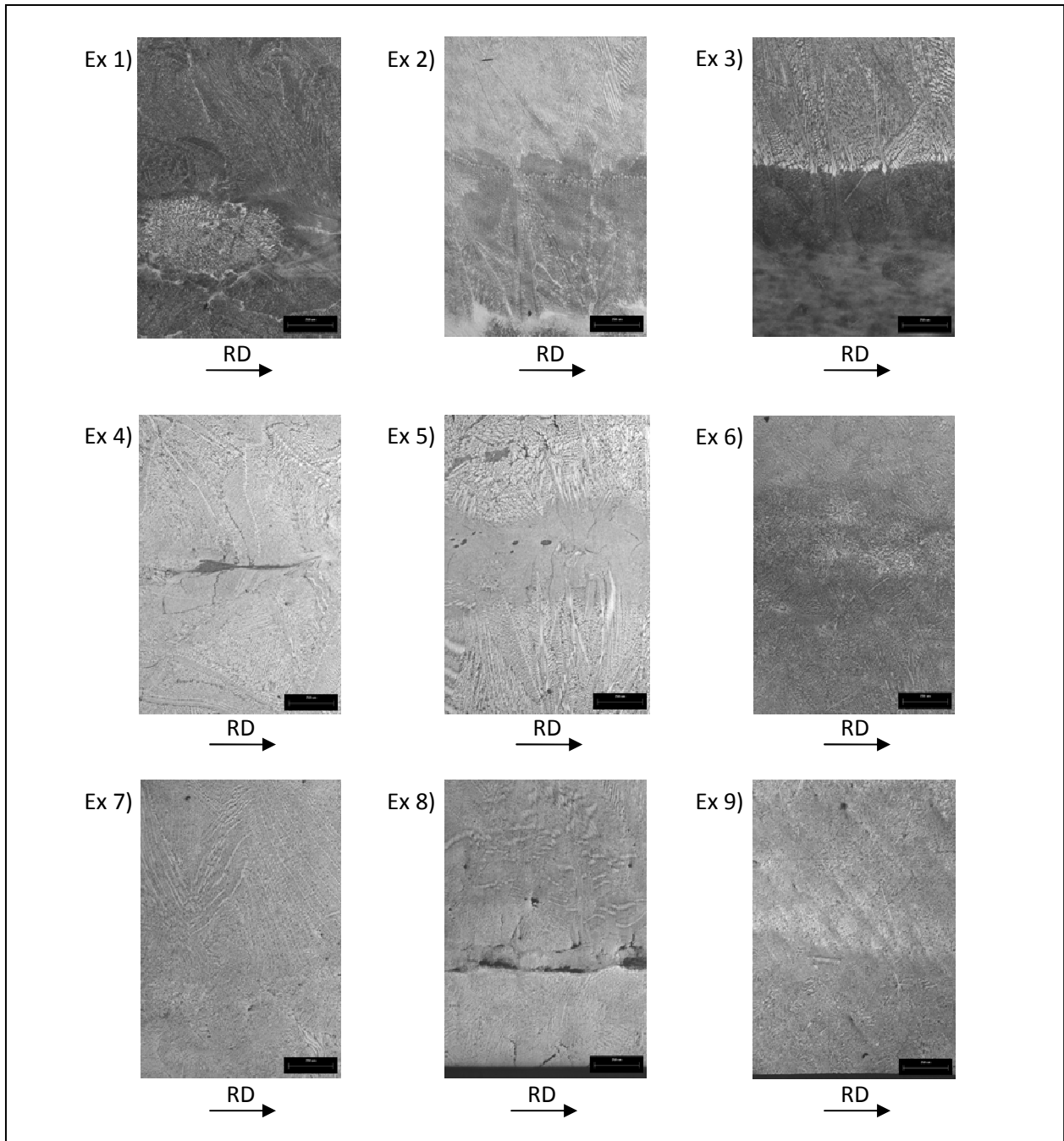


Figure 68 - Palette of all experiment sample thicknesses

EDS Details:

Using the EDS analysis technique, the composition of the material can be determined. This is achieved by the fact that each element has its own unique atomic structure. As a part of the SEM machine, a beam of electrons is sent towards the sample exciting the atoms in its focus. Without any excitation the

atoms contain electron shells with varying energy levels. Once excited, an electron within an inner shell, containing low energy, may be ejected from the atom, leaving an electron hole in its place. To fill this gap, an electron from an outer shell, containing high energy, moves towards the location where the electron within the inner shell was ejected. This difference in energy is released in the form of an X-ray. The amount of energy within the X-ray and the number of occurrences are measured by the spectrometer. This information is then interpreted as the elements present and the quantity of them.

Secondary Dendrite Arm Spacing Pictures:

The following figures were used to measure the secondary dendrite arm spacing of each sample.

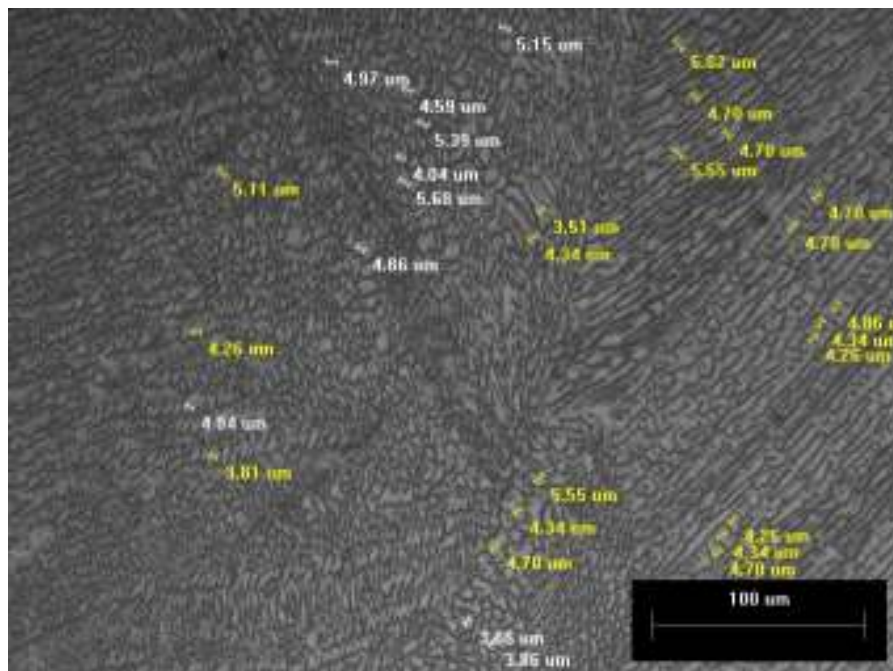


Figure 69 - Experiment 1 SDAS Measurements

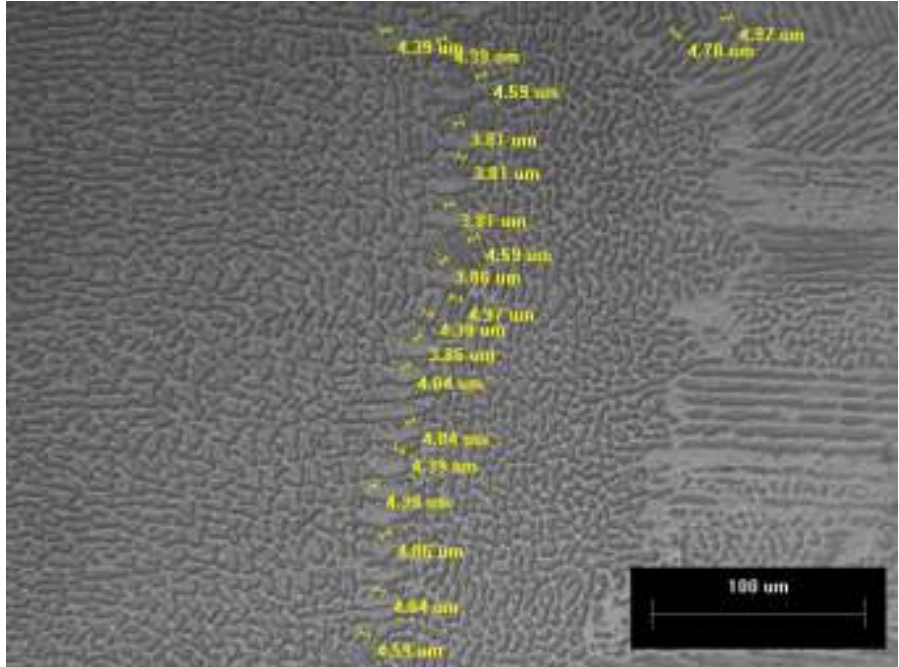


Figure 70 - Experiment 2 SDAS Measurements

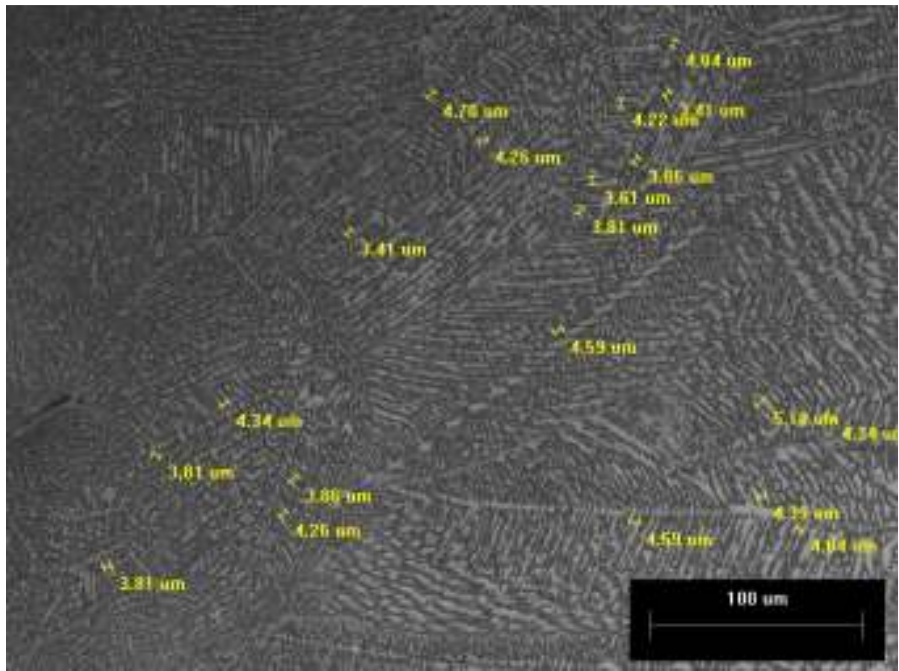


Figure 71 - Experiment 3 SDAS Measurements

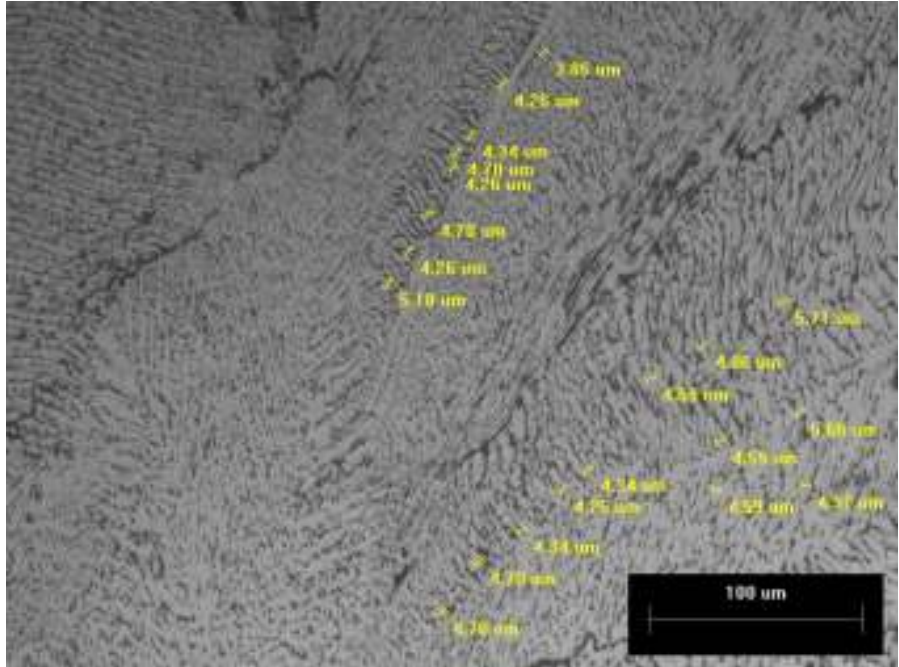


Figure 72- Experiment 4 SDAS Measurements

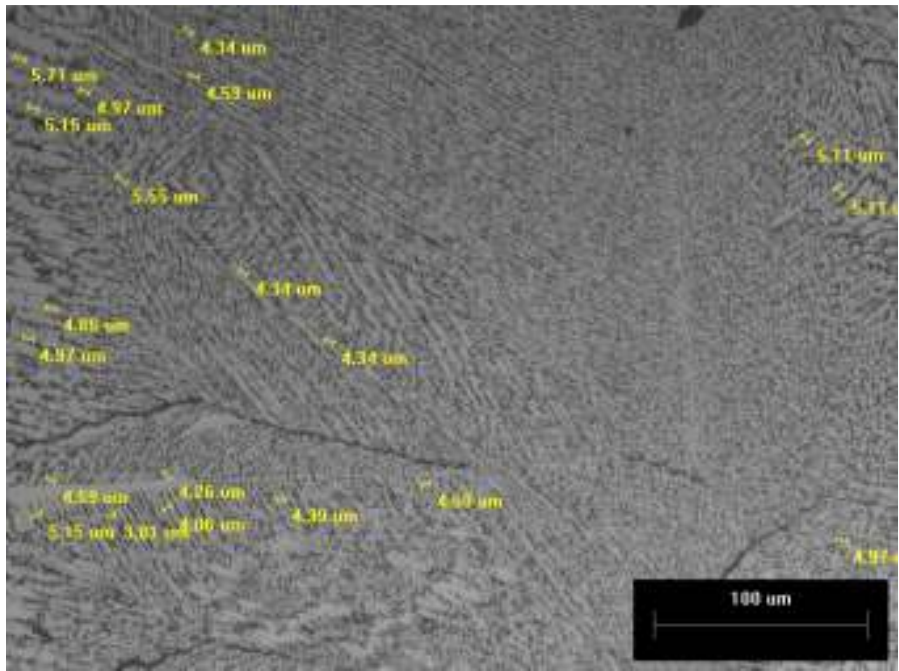


Figure 73 - Experiment 5 SDAS Measurements

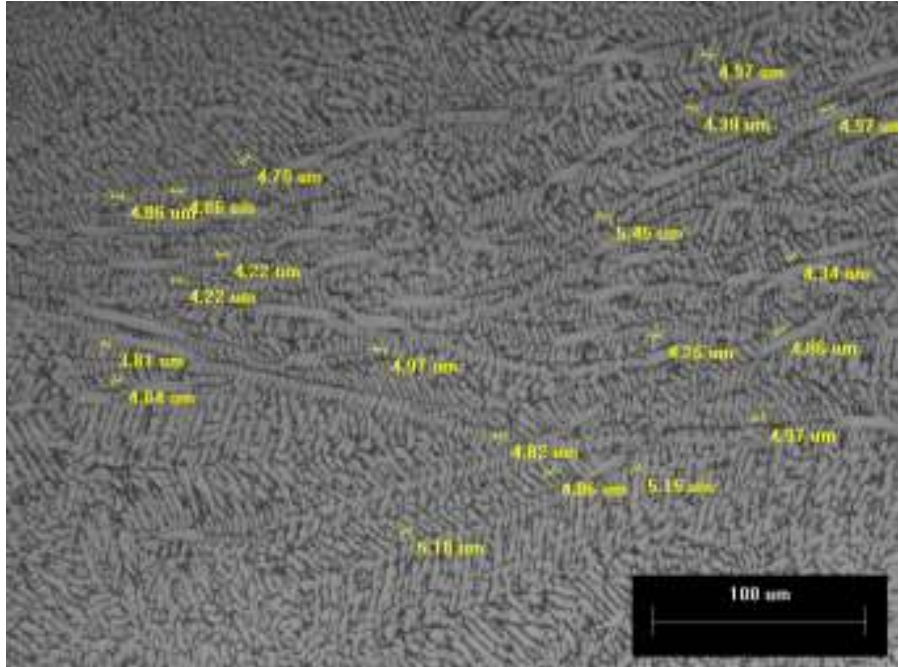


Figure 76 - Experiment 8 SDAS Measurements

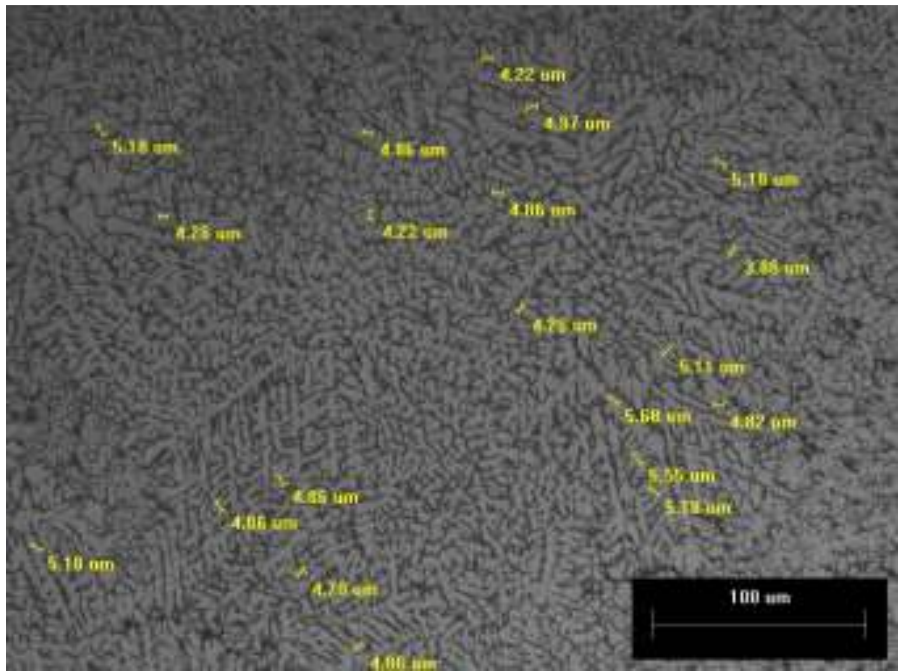


Figure 77 - Experiment 9 SDAS Measurements